

2006

## One and two dimensional surface emitting distributed feedback lasers based on MEH-PPV

Aziz Mahfoud Familia  
*University of Dayton*

Follow this and additional works at: [https://ecommons.udayton.edu/graduate\\_theses](https://ecommons.udayton.edu/graduate_theses)

---

### Recommended Citation

Mahfoud Familia, Aziz, "One and two dimensional surface emitting distributed feedback lasers based on MEH-PPV" (2006). *Graduate Theses and Dissertations*. 4136.  
[https://ecommons.udayton.edu/graduate\\_theses/4136](https://ecommons.udayton.edu/graduate_theses/4136)

This Dissertation is brought to you for free and open access by the Theses and Dissertations at eCommons. It has been accepted for inclusion in Graduate Theses and Dissertations by an authorized administrator of eCommons. For more information, please contact [mschlange1@udayton.edu](mailto:mschlange1@udayton.edu), [ecommons@udayton.edu](mailto:ecommons@udayton.edu).

**One and Two Dimensional Surface Emitting  
Distributed Feedback Lasers Based on MEH-PPV**

Dissertation

Submitted to

School of Engineering

UNIVERSITY OF DAYTON

In Partial Fulfillment of the Requirements for

The Degree of

Doctor of Philosophy in Electro-Optics

By

Aziz Mahfoud Familia

UNIVERSITY OF DAYTON

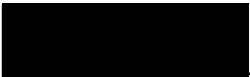
Dayton, Ohio

December, 2006

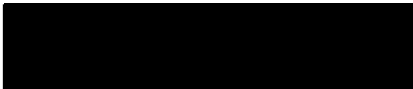
# One and Two Dimensional Surface Emission Distributed Feedback Lasers

Based on MEH-PPV


APPROVED BY:

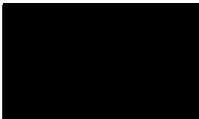
Andrew M. Sarangan, Ph.D.  
Associate Professor,  
Electro-Optics Program  
University of Dayton  
Committee Chairman


Joseph W. Haus, Ph.D.  
Director and Professor,  
Electro-Optics Program  
University of Dayton  
Committee Member


Thomas R. Nelson, Ph.D.  
Air Force Research Laboratory  
Sensors Directory, Wright  
Patterson Air Force Base  
Committee Member


Partha P. Banerjee, Ph.D.  
Professor,  
Electro-Optics Program  
University of Dayton  
Committee Member

Leno Pedrotti, Ph.D.  
Associate Professor,  
Department of Physics  
University of Dayton  
Committee Member

Donald L. Moon, Ph.D.  
Associate Dean and Professor,  
Graduate Engineering  
Program and Research  
School of Engineering

Joseph E. Saliba, Ph.D., P.E.  
Dean, School of Engineering

## ABSTRACT

The focus of this dissertation is one and two-dimensional surface emitting distributed feedback lasers based on the organic polymer 2-methoxy-5-(2-ethylhexyloxy)-1,4-phenylenevinylene (MEH-PPV). Theoretical models are developed, and experimental results are presented for both 1-D and 2-D structures. For the 2-D case the effects of pumping geometry on the laser performance and emission linewidth are studied.

Chapter II describes the basic theory of 1-D DFB laser using the couple mode theory and the Floquet's theorem. A complete solution of the couple equations including the second order or higher diffraction grating is presented. For generality, a semiconductor structure based on InGaAs was chosen for studying the influence of the grating shape in the coupling coefficient and to develop the theoretical formalism to be used in the study of the MEH-PPV based lasers in chapter 3.

Chapter III presents a more detailed description of the couple mode theory that includes evanescent and radiation modes into the coupled equations for the 1-D DFB. The theoretical analysis presented in this chapter is based on the same structure that was used for the experimental results in chapter IV. The decaying and radiating modes were calculated using finite differences and the threshold gain of the device was calculated for

different laser lengths. We show that the an increase in the device length beyond a certain value will, in addition to increasing the feedback strength, will also increase the losses due to the decaying and radiating modes, which may cause the lasing threshold gain to increase.

Chapter IV describes the material and device fabrication and characterizations for the 1-D devices. Interferometric lithography was used for the grating fabrication and the optical properties of MEH-PPV were characterized using visible and UV spectroscopy. Lasing action is reported by photopumping the samples beyond amplified spontaneous emission (ASE).

Chapter V describes the experimental results obtained from the two-dimensional grating structure. The lasing instabilities associated with pumping geometries were demonstrated in the case of 2-D photonic crystal laser. As a result, the laser spectrum and threshold gain were found to be strongly dependent on the excitation geometry.

## ACKNOWLEDGMENTS

I would like to express my gratitude to the many people who have contributed directly and indirectly to this work and whose support has made this effort possible.

First I would like to thank my advisor Andrew Sarangan, for his guidance and enthusiasm through this research. He has contributed substantially not only in this effort, but also tutoring me to develop more critical thinking of both scientific and practical problems. I would like to thank Dr. Joseph Haus for the innumerable discussions throughout my studies at the University of Dayton. I would like to acknowledge the other members of my committee Dr. Partha Banerjee and Leno Pedrotti for their contribution to my formation in the classroom. I also thank Dr. Tom Nelson from the WPABF for his collaboration in this effort.

I also would like to express my gratitude to my fellow students who have undergone the same endeavor. In particular I would like to thank Jang Pyo Kim, Cong Deng, George Nehmetallah and many others.

And finally, I would like to thank my parents for their constant support throughout my university experience.

## TABLE OF CONTENTS

Approval Page.....	ii
Abstract.....	iii
Acknowledgment.....	v
Table of Contents .....	vi
List of Figures.....	viii
Summary of Contributions.....	xii
Table of Contents	
I. Introduction.....	1
II. Coupled Mode Analysis of 1-D Distributed Feedback Lasers.....	3
2.1 Couple Mode theory for TEM Modes.....	3
2.2 Dispersion Relation and threshold Gain.....	15
III. Theoretical Simulation of 1-D Distributed Feedback Laser Based on [2-methoxy-5-(2'-ethylhexyloxy)-1,4-phenylenevinylene] .....	24
3.1 Introduction TEM Modes.....	24
3.2 Numerical solution for the Radiation and Decaying Modes .....	26
3.3 Threshold Gain Calculation .....	46
IV. Experimental Results From 1-D Distributed Feedback Lasers Based on theoretical Simulation of 1-D Distributed Feedback Laser Based on [2-methoxy-5-(2'-ethylhexyloxy)-1,4-phenylenevinylene].....	52

4.1 Conjugated Polymers.....	52
4.2 MEH-PPV Characterization.....	54
4.2.1 Introduction .....	54
4.2.2 Sample Preparation and Optical Characterization .....	55
4.2.3 Absorption Spectrum .....	56
4.2.4 Excitation Spectrum of MEH-PPV in Films .....	58
4.2.5 Photoluminescence and Spectral Line-Narrowing of MEH-PPV in Solution.....	59
4.2.6 Triplet State Absorption .....	63
4.2.7 Photoluminescence and Spectral Line-Narrowing of MEH-PPV in Film.....	64
4.2.8 Grating Fabrication .....	70
4.2.9 Lasing Action .....	73
V. 2-D Distributed Feedback Lasers: theory and Experiments .....	77
Introduction.....	77
Laser action from a two-dimensional distributed feedback laser.....	78
VI. Conclusions .....	82
Recommendations .....	84
Appendix A.....	85
Appendix B.....	95
Bibliography.....	99



## LIST OF FIGURES

Figure 2.1 - Five layer DFB laser structure with trapezoidal corrugation .....	4
Figure 2.2 - Phase as a function of position over an entirely period for first order Bragg diffraction.....	17
Figure 2.3 - Coupling coefficient dependence of the normalized bottom width corrugation for different values of normalized top width for $p=1$ .....	22
Figure 2.4 - Coupling coefficient dependence of the normalized bottom width corrugation for different values of normalized top width for $p=2$ .....	22
Figure 2.5 - Relationship between amplitude threshold gain ( $\alpha L$ ) and detuning coefficient ( $\delta L$ ) for the structure of figure 1. The values of the reflectivities were chosen arbitrary. The phase corrugation was $(3/4)\pi$ .....	23
Figure 2.6 - Relationship between amplitude threshold gain ( $\alpha L$ ) and detuning coefficient ( $\delta L$ ) for the structure of figure 1. The phase corrugation was $2\pi$ ... ..	23
Figure 3.1 - Atomic force microscope (AFM) image of the 1-D photonic crystal structure.....	25
Figure 3.2. - Triangular grating approximation to the one-dimensional photonic crystal structure of figure 3.1.....	26
Figure 3.3 - Index of refraction dependence on the coordinate position ( $x$ ) in the interval $0.93 \leq x < 1$ for the structure of figure 3.2. ....	28

Figure 3.4 - Index of refraction dependence on the coordinate position (x) for the entire structure of figure 3.2.....	29
Figure 3.5 – Fundamental mode calculation corresponding to the structure defined in figure 3.2.....	29
Figure 3.6 – First four orders corresponding to the complex module of $A_q$ .....	30
Figure 3.7 - Radiation mode calculation for $m=-1$ in equation 78. The field intensity is constant at both sides of the corrugation, therefore describing a radiation mode.....	35
Figure 3.8 - Real and imaginary fields corresponding to the radiation mode for $m=1$ in equation 78.....	36
Figure 3.9 – Second order diffraction process in a surface emission DFB.....	37
Figure 3.10 - Decaying mode corresponding to the structure defined in figure 3.2 and for the case of $m=2$ .....	38
Figure 3.11 - Decaying modes calculated from equation 70 for positive values of $m$ . The peak intensity for $m=10$ is about 5 order of magnitude smaller compare with the fundamental mode.....	40
Figure 3.12 - Decaying modes calculated from equation 70 for negative values of $m$ . The peak intensity for $m=-10$ is higher in magnitude compare with $m=10$ .....	41
Figure 3.13 - Decaying modes calculated from equation 71 for positive values of $m$ . The peak intensity for $m=-10$ is higher in magnitude compare with $m=10$ .....	43
Figure 3.14 - Decaying modes calculated from equation 71 for negative values of $m$ . ...	44

Figure 3.15 - Thresholds gain and detuning coefficients for the longitudinal modes in the DFB structure defined in figure 3.2. The values in this graph were calculated using the maple's code of appendix B.....	49
Figure 3.16 - Flowchart illustrate the solution procedure for the 1-DFB laser threshold gain determination. ....	51
Figure 4.1 - Four-level energy diagram for a conjugated polymer.....	54
Figure 4.2 - UV-vis absorption spectra of thin film of MEH-PPV in different solvents...	57
Figure 4.3 - Excitation spectra of MEH-PPV thin film. nm.....	59
Figure 4.4 - The experimental setup for the PL and ASE measurements.....	61
Figure 4.5 - Photoluminescence (a,b,c) and spectral line narrowing (c,d,e) spectra of MEH-PPV at different concentrations in solution and in different solvents. ....	62
Figure 4.6 - Electronic Transitions involving both singlet and triplet states. ....	63
Figure 4.7 -Photoluminescence spectra of MEH-PPV in solution and films.....	64
Figure 4.8 - Photoluminescence (a,b,c,) and spectral line-narrowing (d,e,f) spectra of MEH-PPV at different concentrations in films and in different solvents. ....	67
Figure 4.9 - Spectra line-narrowing of MEH-PPV film cast from the toluene solution...	68
Figure 4.10 – Interferometric lithography setup.....	71
Figure 4.11 - Rotating stage cylinder showing the UV mirror, the vacuum suction for the sample holder and the angle scale.....	71
Figure 4.12 - shows the atomic force microscope (AFM) image of the 1-D photonic crystal structure. The period of the corrugation was about 400 nm with an average depth of 70 nm. ....	72

Figure 4.13 - Schematic showing the grating period measurement. The period is obtained by determining the inside and diffracted angle.....	74
Figure 4.14 – Theoretical calculation of the fundamental mode of the polymer waveguide structure.....	74
Figure 4.15 - Amplified spontaneous emission (ASE) spectrum (dashed) obtained by photopumping an unpatterned film of MEH-PPV coated with PMGI. ....	76
Figure 5.1 – Atomic force microscope (AFM) image of the 2-D photonic crystal structure.....	79
Figure 5.2 - Laser action from a 2-D PCL as pumped with circular spot. This pumping configuration presents better spectral characteristics compare with the elliptical geometry.	
Figure 5.2(b). Laser spectrum from a 2-D PCL as pumped with an elliptical spot.....	81
Figure 5.3 – Second order diffraction mechanism in 2-D PCL. In this configuration the grating vector couples the forward and backward waves in two steps. Surface emission is achieved through crossing the origin of the k-space coordinates after the first diffraction step. The device behaves as a two independent resonators and thus performance is dependent on pumping geometry. Figure 5.3(b). Fourth order process in 2-D PCL.....	81

## SUMMARY OF CONTRIBUTIONS

Chapter	Overview	Contribution	
		Journal	Conference
1. Introduction			
2. Couple Mode Analysis of 1-D Distributed Feedback Lasers	Couple mode theory is analyzed in the context of 1-D distributed feedback laser. The threshold equation is derived and the effect of finite reflections at the laser facets is considered.	- Optics Communications (2006) <sup>2</sup>	- GLPS (2006) <sup>3</sup>
3. Theoretical Simulation of 1-D Distributed Feedback Laser Based on [2-methoxy-5-(2'-ethylhexyloxy)-1,4-phenylenevinylene]	This chapter illustrates the formalism developed in the previous chapter for the analysis of 1-D distributed feedback laser. The analysis is based on actual devices that were fabricated for the simulation of 1-D devices. The conductive polymer MEH-PPV ([2-methoxy-5-(2'-ethylhexyloxy)-1,4-phenylenevinylene] ) was used as the gain medium.	- Optics commun. (2006) <sup>2</sup>	-GLPS (2006) <sup>3</sup>
4. Experimental Results From 1-D Distributed Feedback Lasers Based on based on [2-methoxy-5-(2'-ethylhexyloxy)-1,4-phenylenevinylene]	This chapter presents the optical characterization and laser action from 1-D distributed feedback lasers based on the polymer MEH-PPV as the gain medium. The first part of this chapter develops the spectroscopic properties of MEH-PPV. Later the device fabrication and characterization is introduced. The laser characterization is presented at the end of this chapter.	Journal of Luminescence (2005) <sup>1</sup> Optical Materials (2006) <sup>2</sup>	-GLPS (2004) <sup>3</sup> OSA Annual Meeting (2005) <sup>3</sup>
5. 2-D Distributed Feedback Lasers Theory and Experiments.	In this chapter we present experimental results of two-dimensional distributed feedback laser based on MEH-PPV. We report laser instabilities associated with the pumping geometry for 2-D photonic crystal structures. These instabilities can result in the degradation of the spectral quality of the laser emission and in an increase in the threshold gain.	Optics Express (2005) <sup>1</sup>	-SPIE Annual Meeting (2005) <sup>1</sup>
6. Conclusions	This is a comprehensive study of one and two dimensional distributed feedback lasers (1D-DFB and 2D-DFB). Detailed numerical and experimental results were presented for the case of 1D-DFB. For the experimental studies the polymer 2-methoxy-5-(2'-ethylhexyloxy)-1,4-phenylenevinylene (MEH-PPV) was employed as gain media. This dissertation also presents experimental results for optically pumped 2D-DFB lasers with different pumping geometries.		

1. Accepted for publication, 2. Submitted for publication, 3. Accepted for presentation.

# Chapter I

## Introduction and Background

The possibility of generating circularly shaped, diffraction-limited beams, as well as transform limited (time-bandwidth), with relative low threshold gain, makes 1-D and 2-D distributed feedback (DFB) lasers very attractive for a variety of applications including fiber optic and free space communications, sensing and high power sources. The interest in DFB lasers has increased recently in the context of photonic crystals, due to the unique ability of these structures to confine light in multiple dimensions. The absence of optical modes in the photonic band gap can be used to suppress the spontaneous emission and create resonances that can be used in a variety of applications. By designing the photonic band gap to overlap the electronic band [1], the electron-hole recombination can be controlled leading to enhanced efficiency and reduced noise operation in certain optoelectronic devices.

1-D photonic band gap structures have been exhaustively studied for almost 50 years, and are the principles behind many devices such as dielectric mirrors, Fabry-Perot filters, and *distributed feedback lasers*. A complete mathematical description of a 1-D distributed feedback laser was developed in the mid-70's by Striefer *et al.*[2,3,4,5] after the pioneering work of Kolgenik *et al.* [6] and Handa *et*

*al.* [7]. Although the theoretical models were developed in the early 70's, it was not until 1975 when the first DFB laser diode operation was demonstrated [8].

Extending the one dimensional DFB to two dimensions has several interesting applications such as the potential for higher power, surface-normal emission and ease of fabrication. Two-dimensional distributed feedback structures in planar waveguides were first used in thin films with laser dyes by S. Wang *et al.* [9, 10]. Later the threshold gain characteristics of semiconductor lasers with 2-D gratings were studied by coupled mode theory [11, 12]. More recently, laser action from two-dimensional photonic crystals using organic gain media have been reported [13].

In this work we present both theoretical and experimental results of 1-D and 2-D distributed feedback lasers based on the organic polymer 2-methoxy-5-(2-ethylhexyloxy)-1,4-phenylenevinylene (MEH-PPV). Coupled mode theory was used to develop the theoretical formalism for these laser structures. We also report laser instabilities associated with the pumping geometry for the 2-D structures. These instabilities can result in degradation of the spectral quality of the laser emission and in an increase of the threshold gain of the devices.

## Chapter II

### Coupled Mode Analysis of 1-D Distributed Feedback Lasers

#### *2.1 Coupled Mode Theory for TEM Modes.*

Coupled mode analysis is a powerful technique for the analysis of periodic structures. When combined with Floquet's theorem, it becomes a robust formalism able to characterize wave propagation in photonic crystals. Since most practical distributed feedback lasers contain many layers with a periodic index corrugation etched into one of the layers, the wave equation can be written as:

$$\nabla^2 \mathbf{E} + k_0^2 n_t^2(x, z) \mathbf{E} = 0 \quad (1)$$

where  $n_t$  is the effective index that varies periodically due to the corrugation. Refer to figure 2.1. When the radiation frequency is sufficiently close to the resonance frequency of the material, the propagation constant can be expressed as [14]:

$$k_0^2 n_t^2(x) = k_0^2 n^2(x) \left( 1 - i \frac{2\alpha(x)}{k_0 n(x)} \right) \quad (2)$$

In this equation, the propagation constant is expanded into its real and imaginary parts, where  $n(x)$  is the real part, and  $\alpha(z)$  and  $k_0$  represent the gain coefficient and the free space propagation constant respectively.



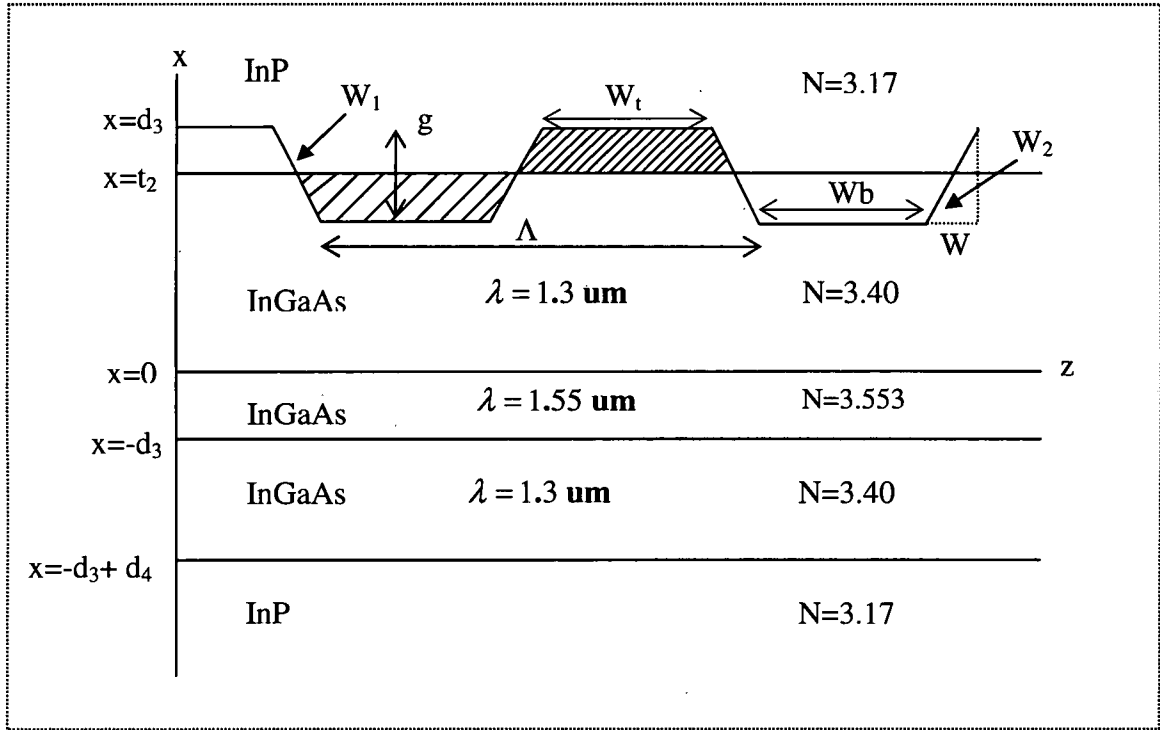


Figure 2.1 - Five layer DFB laser structure with trapezoidal corrugation

By considering the solution corresponding to the TE modes, the wave equation can be expanded as:

$$\frac{\partial^2 E_y}{\partial x^2} + \frac{\partial^2 E_y}{\partial z^2} + k_0^2 n_i^2(x, z) E_y = 0 \quad (3)$$

To begin our analysis, we try to find an analytical expression for the index of refraction in the perturbation region. Since only two values of index of refraction are presented in figure 2.1 for the corrugation, the unit step function is an obvious choice.

Then the index of refraction in the perturbation region can be written as [3]:

$$n^2(x, z) = \sum_{p=-\infty}^{\infty} n_1^2 \{u[z - w_1(x) - p\Lambda] - u[z - w_2(x) - p\Lambda]\} + n_2^2 \{u[z - w_2(x) - p\Lambda] - u[[z - w_1(x) - (p+1)\Lambda]]\} \quad (4)$$

where  $u$  is the unit step function,  $p$  is an integer that relates to the order of the perturbation,  $w_1(x)$  and  $w_2(x)$  represent the functions describing the grating tooth.

The periodicity in index of refraction suggests a Fourier expansion in two dimensions.

A convenient form to express the expansion is:

$$n^2(x, z) = n_0^2(x) + \sum_{\substack{q=-\infty \\ q \neq 0}}^{\infty} A_q(x) e^{(i2\pi qz/\Lambda)} \quad (5)$$

In this last expression  $n_0$  represents the zero-order expansion of the index of refraction and  $A_q$ 's represent higher order Fourier coefficients. . Outside the grating region,  $n_0$  will become the refractive index of the medium, and all the  $A_q$ 's will become zero. Then, we write  $n_0$  and  $A_q$  in the grating region as:

$$n_o^2 = \{n_2^2 + (n_1^2 - n_2^2)[w_2(x) - w_1(x)]\} / \Lambda \quad (6)$$

$$A_q(x) = \frac{1}{\Lambda} \int_{-\Lambda/2}^{\Lambda/2} n^2(x, z) e^{-(i2\pi qz/\Lambda)} dz \quad (7)$$

By integrating equation 7 over one grating period, a simplification to this expression is obtained:

$$A_q(x) = \left( \frac{n_2^2 - n_1^2}{i2\pi q} \right) \left( \exp\left(\frac{-i2\pi q w_2}{\Lambda}\right) - \exp\left(\frac{-i2\pi q w_1}{\Lambda}\right) \right) \quad (8)$$

Upon substituting equations 2 and 5 into equation 3, the following expression is obtained:

$$\frac{\partial^2 E_y}{\partial x^2} + \frac{\partial^2 E_y}{\partial z^2} + (k_0^2 n_0^2 - 2i\alpha(x)k_0 n_0(x)) E_y + k_0^2 E_y \sum_{\substack{q=-\infty \\ q \neq 0}}^{\infty} A_q(x) e^{(i2\pi q z / \Lambda)} = 0 \quad (9)$$

To solve equation 9, we will assume a solution in the form of an infinite summation of plane waves dictated by Floquet's theorem:

$$E_y(x, z) = \sum_m E_y^m(x, z) e^{i\beta_m z}, \quad (10)$$

where  $\beta_m = \beta_0 + \frac{2\pi m}{\Lambda}$  and  $\beta_0$  is the propagation constant in the waveguide and  $m$  is an integer. By substituting equation 10 into 9 and collecting the term with the same exponential dependence, the wave equation becomes:

$$\frac{\partial^2 E_y^m}{\partial x^2} + \frac{\partial^2 E_y^m}{\partial z^2} + 2i\beta_m \frac{\partial E_y^m}{\partial z} + (k_0^2 n_0^2 - 2i\alpha(x)k_0 n_0(x) - \beta_m^2) E_y^m + k_0^2 \sum_{\substack{q=-\infty \\ q \neq 0}}^{\infty} A_q(x) E_y^{m-q} = 0, \quad \forall m. \quad (11)$$

Notice that the Bragg condition requires  $\Lambda = \frac{N\lambda_0}{2n_{eff}}$ , where  $N$  a positive integer and

$n_{eff}$  is effective index of the waveguide. So, if the Bragg condition is satisfied for a particular  $p = -N$ , where  $p$  represent the diffraction order of the grating, in a case of surface emission DFB  $p=-2$ . Then it is easy to see that  $A_p(x)$  couples  $E_y^0(x, z)$  to  $E_y^p(x, z)$ . Assuming that  $E_y^0(x, z)$  and  $E_y^p(x, z)$  are separable in  $z$  and  $x$ :

$$E_y^0(x, z) = R(z)E_0(x) \quad (12)$$

$$E_y^p(x, z) = S(z)E_0(x) \quad (13)$$

where  $R(z)$  and  $S(z)$  represent the waves traveling in the  $+z$  and  $-z$  directions respectively. Upon substitution of these two last equations into equation (11) and applying the slowly varying envelope approximation for the  $R(z)$  and the  $S(z)$  waves, equation (11) becomes:

$$2i\beta_0 \frac{dR}{dz} E_0 + R \left[ \frac{dE_0}{dx^2} + [k_0^2 n_0(x) - 2i\alpha(x)k_0 n_0(x) - \beta_0^2] E_0 \right] + k_0^2 \sum_{\substack{q=-\infty \\ q \neq 0}}^{\infty} A_q(x) E_y^{-q}(x, z) = 0 \quad (14)$$

$$-2i\beta_0 \frac{dS}{dz} E_0 + S \left[ \frac{dE_0}{dx^2} + [k_0^2 n_0(x) - 2i\alpha(x)k_0 n_0(x) - \beta_0^2] E_0 \right] + k_0^2 \sum_{\substack{q=-\infty \\ q \neq 0}}^{\infty} A_q(x) E_y^{p-q}(x, z) = 0 \quad (15)$$

Adding and subtracting  $\beta E_0 R$  and  $\beta E_0 S$  to equations (14), (15) respectively, and imposing the condition:

$$\frac{d^2 E_0}{dx^2} + [k_0^2 n_0^2(x) - \beta^2] E_0 = 0 \quad (16)$$

Leads to:

$$2i\beta_0 \frac{dR}{dz} E_0 + [-2i\alpha(x)k_0 n_0(x) - \beta_0^2 + \beta^2] R E_0 + k_0^2 A_{-p}(x) S E_0 + k_0^2 \sum_{\substack{q=-\infty \\ q \neq 0, -p}}^{\infty} A_q(x) E_y^{-q}(x, z) = 0 \quad (17)$$

$$-2i\beta_0 \frac{dR}{dz} E_0 + [-2i\alpha(x)k_0 n_0(x) - \beta_0^2 + \beta^2] R E_0 + k_0^2 A_p(x) R E_0 + k_0^2 \sum_{\substack{q=-\infty \\ q \neq 0, p}}^{\infty} A_q(x) E_y^{p-q}(x, z) = 0 \quad (18)$$

It should be emphasized that equation (16) is a standard waveguide equation, and the index of refraction is the zero-order component of the refractive index of the grating. Since the index of refraction is a function of the position, this equation can be solved by numerical methods (finite differences). An alternative solution for this problem involves the replacement of the grating by two layers, so that the transverse waveguide can be treated as an unperturbed structure [15]. Also in obtaining the coupled equations (17) and (18),  $q = -p$  and  $q = p$  was substituted into the summation of equations (14), (15).

These expressions can be simplified if equations 14 and 15 are multiplied by  $E_0$  and integrated over  $(-\infty, \infty)$ :

$$\frac{dR}{dz} - [\alpha_0 + i\delta] R - i\kappa_p S - \frac{ik_0^2}{2\beta_0 P} \sum_{\substack{q=-\infty \\ q \neq 0, -p}}^{\infty} \int_{\text{grating}} A_q(x) E_0 E_y^{-q} dx = 0 \quad (19)$$

$$-\frac{dS}{dz} - [\alpha_0 + i\delta] S - i\kappa_{-p} R - \frac{ik_0^2}{2\beta_0 P} \sum_{\substack{q=-\infty \\ q \neq 0, -p}}^{\infty} \int_{\text{grating}} A_q(x) E_0 E_y^{p-q} dx = 0 \quad (20)$$

where,

$$\kappa_p = \frac{k_0^2}{2\beta_o P} \int_{\text{grating}} A_p(x) E_0^2(x) dx \quad (21)$$

$$P = \int_{-\infty}^{\infty} E_0^2(x) dx \quad (22)$$

$$\alpha_0 = \frac{k_0}{\beta_o P} \int_{-\infty}^{\infty} n_0(x) \alpha(x) E_0^2 dx \quad (23)$$

Notice that  $A_q = 0$  in the regions outside the grating. Then the integrals involving  $A_q$  have limits within the grating.  $\kappa_p$  is the coupling coefficient and represents the strength of the coupling between the forward and backward  $R(z)$  and  $S(z)$  waves. This coupling coefficient depends on the confinement of the waveguide mode in the grating region and the shape and index contrast of the corrugation. The coupling coefficient is also proportional to the index differences in the grating region. Observe also that the modal gain,  $\alpha_0$  becomes equal to  $\alpha$  in the absence of the grating.

It is not possible yet to evaluate equations (19) and (20), since the  $E_y^q(x, z)$  fields are not known. Since the field changes more rapidly in the  $x$  direction compared to the  $z$  directions, we will assume in equation (11) that the derivatives with respect to  $z$  are small compared to the derivatives in  $x$ . Also by assuming that only the fields  $E_y^0(x, z)$  and  $E_y^p(x, z)$  are relevant in generating  $E_y^m$ , equation (11) can be simplified as:

$$\frac{\partial^2 E_y^m(x, y)}{\partial x^2} + (k_0^2 n_0^2 - \beta_m^2) E_y^m(x, y) + k_0^2 E_0 [A_m R(z) + A_{m-p} S(z)] = 0 \quad (23)$$

The argument behind this simplification is the fact that the  $E_y^m$  field in the Floquet's summation tends to decay rapidly for larger order  $|m|$ . In this sense, the contribution of the mode  $m$  to higher modes can be ignored. Inspecting the last term of the equation (23), it is reasonable to assume a separable variable solution of the form:

$$E_y^m(x, z) = R(z)E_m^0(x) + S(z)E_m^p(x) \quad \forall m \quad m \neq 0, p \quad (24)$$

This last equation suggests that the field  $E_y^m$  is a consequence of the interaction of both  $E_y^0(x, z)$  and  $E_y^p(x, z)$  in which the terms  $R(z)$  and  $S(z)$  represent weighting factors respectively. By substitution of equation 24 into equation 23 and grouping the terms with the same  $z$  dependence, the following two equations are obtained,

$$\frac{d^2 E_m^0}{dx^2} + [k_0^2 n_0^2 - \beta_m^2] E_m^0 + k_0^2 A_m(x) E_0(x) = 0 \quad \forall m \quad m \neq 0 \quad (25)$$

$$\frac{d^2 E_m^p}{dx^2} + [k_0^2 n_0^2 - \beta_m^2] E_m^p + k_0^2 A_{m-p}(x) E_0(x) = 0 \quad \forall m \quad m \neq p \quad (26)$$

These last two equations can be solved by numerical techniques. Notice that these equations differ from the classical waveguide equations due to the extra driving term. The  $E_m^p$  and  $E_m^0$  fields along with the guided mode field  $E_0$ , constitute the complete solution to the electromagnetic problem stated in equation (3). While  $E_0$  is the guided mode confined to the waveguide structure,  $E_m^p$  and  $E_m^0$  represent radiation modes that are not confined to the waveguide structure. Once the radiation modes are determined the integrals of equation (19) and (20) can be evaluated.

$$\frac{dR}{dz} - (\alpha_0 + i\delta)R - i\kappa_{-p}S - \frac{ik_0^2}{2\beta_0 P} \sum_{\substack{q=-\infty \\ q \neq 0, -p}}^{\infty} \int_{\text{grating}} A_q(x) E_0 \left( R(z) E_{-q}^0(x) + S(z) E_{-q}^p(x) \right) dx \quad (27)$$

$$\frac{dS}{dz} - (\alpha_0 + i\delta)S - i\kappa_p R - \frac{ik_0^2}{2\beta_0 P} \sum_{\substack{q=-\infty \\ q \neq 0, p}}^{\infty} \int_{\text{grating}} A_q(x) E_0 \left( R(z) E_{p-q}^0(x) + S(z) E_{p-q}^p(x) \right) dx \quad (28)$$

The two integrals in equations 27 and 28 are in reality 4 integrals that can be grouped according with the modes  $E_m^p$  and  $E_m^0$ . The following integrals are defined:

$$\zeta_1 = \frac{k_0^2}{2\beta_0 P} \sum_{\substack{q=-\infty \\ q \neq 0, -p}}^{\infty} \int_{\text{grating}} A_q(x) E_{-q}^0(x) E_0(x) dx \quad (29)$$

$$\zeta_2 = \frac{k_0^2}{2\beta_0 P} \sum_{\substack{q=-\infty \\ q \neq 0, p}}^{\infty} \int_{\text{grating}} A_q(x) E_{-q}^p(x) E_0(x) dx \quad (30)$$

$$\zeta_3 = \frac{k_0^2}{2\beta_0 P} \sum_{\substack{q=-\infty \\ q \neq 0, p}}^{\infty} \int_{\text{grating}} A_q(x) E_{p-q}^p(x) E_0(x) dx \quad (31)$$

$$\zeta_4 = \frac{k_0^2}{2\beta_0 P} \sum_{\substack{q=-\infty \\ q \neq 0, p}}^{\infty} \int_{\text{grating}} A_q(x) E_{p-q}^0(x) E_0(x) dx \quad (32)$$

Note that the equations 29 and 30 are corrections to the quantities defined in reference [5] (equations 24a and 24b) In this reference the summation for these two parameters include  $m = p$  instead of  $m = -p$ . It is interesting to point out that the term in equation (19) that contains the coupling coefficient was obtained through the evaluation of the integral in this expression for  $m = -p$ . The expression in ref [5] incorrectly adds twice the coupling coefficient into the equation (19). The significance of the parameters defined in equations (29-32) resides in not only in the modification of the coupled mode equations (27) and (28), but more importantly in the threshold gain



condition of the device as will be shown later. Previous reports describing the threshold gain characteristic of the DFB laser have only considered the coupling coefficient as significant. These assumptions were valid in the context of edge emitting devices. Nevertheless, the parameters in equations (29-31) are essential for the analysis of second order and higher order DFB lasers.

By incorporating the parameters from equations (29-32), the following coupled mode equations that include the conventional forward-backward coupling as well as the radiation and decaying modes:

$$\frac{dR}{dz} - (\alpha_0 + i\delta + i\zeta_1)R - i(\kappa_p^* + \zeta_2)S = 0 \quad (33)$$

$$-\frac{dS}{dz} - (\alpha_0 + i\delta + i\zeta_3)R - i(\kappa_p + \zeta_4)S = 0 \quad (34)$$

Notice that from the definition  $A_q$  in equation 8,  $\kappa_{-p} = \kappa^*$ . A close examination of equation 25 and 26 illustrates the nature of the waves generated as a consequence of the interaction of the guided wave  $E_0$  with the grating structure. Both radiating and decaying waves can be produced, depending of the value of the propagation constant  $\beta_m$ . For instance, a more accurate expression can be written to describe the nature of the  $E_m^0$  modes, for instance:

$$\text{If } |\beta_m| < \beta_0 \quad \text{then radiation waves are generated;} \quad (35)$$

$$\text{If } |\beta_m| > \beta_0 \quad \text{then decaying waves are generated;} \quad (36)$$

In the above equations  $\beta_0 = \frac{\pi N}{\Lambda}$ , where  $N$  is the diffraction order of the grating. Since the modes  $\beta_m$  are characterized by a propagating constant given by:

$$\beta_m = \beta_0 + \frac{2\pi m}{\Lambda}, \quad (37)$$

therefore  $\beta_m = \beta_0 \left(1 + \frac{2m}{N}\right)$  where  $m = \dots -3, -2, -1, 0, 1, 2, 3 \dots$

(38)

It is interesting that  $\zeta_1$  represents an overlap integral summation between the guided mode and both the radiating modes ( $p < q < 0$ ), and the decaying modes ( $q < p, q > 0$ ) with  $A_q(x)$  as a dynamic weighting factor. In the same sense,  $\zeta_3$  represents the reaction of all partial waves  $E_{p-q}^p(x)$ , (except  $E_y^0$ ) that are generated by the interaction of the waveguide mode traveling in the  $-z$  direction. Since both decaying and radiating modes carry power away from the laser, the imaginary parts of both  $\zeta_1$  and  $\zeta_3$  must be negative. Also notice that the real parts of  $\zeta_1$  and  $\zeta_3$  are similar in nature to  $\delta$  as can be seen by examining equations 33 and 34. In this sense, the real part of  $\zeta_1$  and  $\zeta_3$  shift the lasing wavelength in the structure from the resonant Bragg condition.

Since the partial waves  $E_{p-q}^p(x)$  generated by the  $+z$  and  $-z$  are similar, a close examination of  $\zeta_1$  and  $\zeta_3$ , reveals that for both symmetrical and asymmetrical grating teeth  $\zeta_1 = \zeta_3$ . This intuitive argument helps us to write the couple equations as:

$$\frac{dR}{dz} - (\alpha_0 + i\delta + i\zeta_1)R - i(\kappa_p^* + \zeta_2 S) = 0 \quad (39)$$

$$-\frac{dS}{dz} - (\alpha_0 + i\delta + i\zeta_3)R - i(\kappa_p^* + \zeta_4 S) = 0 \quad (40)$$

These results are consistent with previous papers [3] on edge emitting devices ( $m=-1$ ). This paper [3] demonstrated that guided waves traveling in opposite direction radiate the same power independent of the teeth shape.

To obtain a physical interpretation for the  $\zeta_2$  and  $\zeta_4$  integrals, first notice that these parameters represents the reaction of all partial waves generated by  $E_y^p$  and  $E_y^0$  respectively. It is interesting to point out that the analyzing the coupled equations (39 and 40), shows that the effect of  $\zeta_2$  and  $\zeta_4$  is to couple the backward and forward waves in the waveguide. Another way to visualize these parameters is by considering them as corrections to the coupling coefficient. For both symmetrical and asymmetrical gratings  $\zeta_2$  and  $\zeta_4$  are in general complex. For symmetrically shaped grating it can be shown that [5]:

$$\zeta_2 = \left| \left( \frac{\kappa_p^*}{\kappa_p} \right) \right| \zeta_4 \quad (41)$$

For the special case of edge emitting devices ( $p=-1$ ) when no radiation modes are generated,  $\zeta_1$  is real and  $\zeta_2 = \zeta_4^*$ . However for  $p \leq 2$ , the two contradirectional guided waves combines each other to produce either gain or loss coupling (by means of the complex part of  $\zeta_2$  and  $\zeta_4$ ). Also as described in [6, 16] the longitudinal mode

structure of a DFB laser is no longer symmetrical about the Bragg condition. A close examination of the above derivations shows that the grating structure modifies not only the lasing wavelength by modifying  $\delta$ , but also the threshold gain through the imaginary part of  $\zeta_1$ .

## 2.2 Dispersion Relation and Threshold Gain Equation

Further simplification of the coupled mode equations can be obtained by defining:

$$\hat{\alpha} + i\hat{\delta} = \alpha + i\delta + i\zeta_i \quad (42)$$

where  $\hat{\alpha}$  and  $\hat{\delta}$  are real.

Then the coupled mode equations can be written as:

$$\frac{dR}{dz} - \left( \hat{\alpha} + i\hat{\delta} \right) R - i(\kappa_p^* + \zeta_2) S = 0 \quad (43)$$

$$-\frac{dS}{dz} - \left( \hat{\alpha} + i\hat{\delta} \right) S - i(\kappa_p^* + \zeta_4) R = 0 \quad (44)$$

Now, due to the nature of the above coupled equations, solutions of the form  $\exp(\gamma Z)$  are expected for both  $R(z)$  and  $S(z)$ . By substituting these exponential solutions into equations 43 and 44, we obtain:

$$\gamma \exp(\gamma z) - \left( \hat{\alpha} + i\hat{\delta} \right) \exp(\gamma z) = i(\kappa_p + \zeta_2) \exp(\gamma z) \quad (45)$$

$$-\gamma \exp(\gamma z) - \left( \hat{\alpha} + i\hat{\delta} \right) \exp(\gamma z) = i(\kappa_p^* + \zeta_4) \exp(\gamma z) \quad (46)$$

Then by multiplying the above equation together and dividing the result by  $\exp(\gamma z)$ , the following dispersion relation is obtained :

$$\gamma^2 = \left( \hat{\alpha} + i \hat{\delta} \right)^2 + \left( \kappa_p^* + \zeta_2 \right) \left( \kappa_p + \gamma_p \right) \quad (47)$$

The significance of the dispersion relation is that it provides the means to determine the two most important parameters in the performance of a DFB laser: the threshold gain  $\hat{\alpha}$  and the detuning coefficient  $\hat{\delta}$ . Notice that  $\hat{\alpha}$  is not only a function of the gain media properties but also the periodic structure as well. Also it is important to point out that the threshold gain increased as a direct consequence of the radiation modes, as it will be shown later.

The above equation is not yet general, since the boundary conditions at the end of the device have not been discussed. As a consequence of the finite dimensions of the laser, the propagating electromagnetic radiation experiences reflections at both terminating facets. The Fresnel reflections at the laser facets have a very important effect on the lasing characteristic of the device, especially on the threshold gain. Another interesting effect that is a direct result of the finite dimension of the device, is the phase associated with the facets. To produce single devices from a whole wafer, they are cleaved in individual pieces. The exact position of the cleave line through the grating induces a phase term. In most cases this phase is not directly controllable during manufacture. Figure 2.2 illustrates the concept of phase facet.

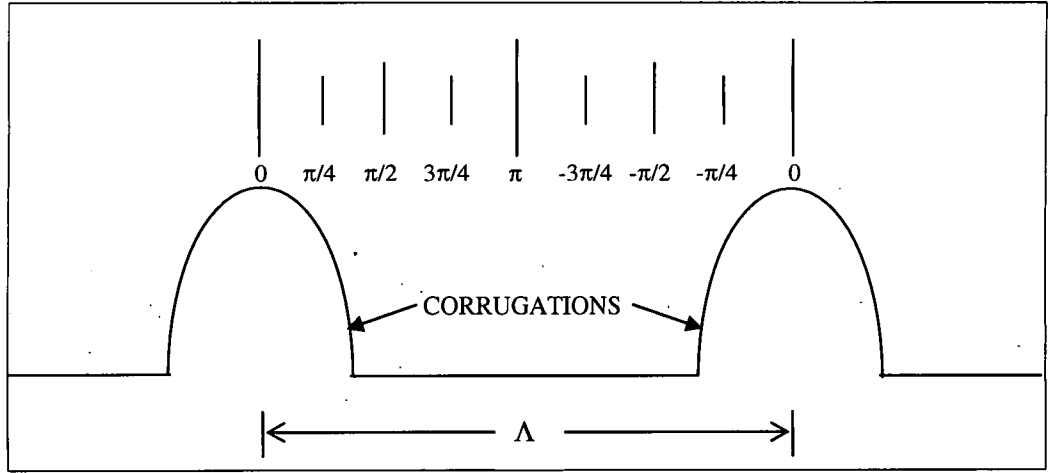


Figure 2.2 - Phase as a function of position over an entirely period for first order Bragg diffraction.

The presences of these phases at the end facets modify the coupled equation such as:

$$\frac{dR}{dz} - \left( \hat{\alpha} + i\hat{\delta} \right) R - i(\kappa_p^* + \zeta_2) \exp(-i\Omega) S = 0 \quad (48)$$

$$-\frac{dS}{dz} - \left( \hat{\alpha} + i\hat{\delta} \right) S - i(\kappa_p + \zeta_4) \exp(i\Omega) R = 0 \quad (49)$$

where  $\Omega$  represent the phase facets and both ends of the grating structure. Just as in equations 43 and 44, equations 48 and 49 are constant coefficient linear differential equations that admit exponential solution of the form:

$$R(z) = r_1 \exp(\gamma z) + r_2 \exp(-\gamma z) \quad (50)$$

$$S(z) = s_1 \exp(\gamma z) + s_2 \exp(-\gamma z) \quad (51)$$

Here  $r_1, r_2, s_1$ , and  $s_2$  are constants that are determined by equation 48 and 49 and by the boundaries condition at the end of the grating. Notice also that a physical solution

of the above equation requires the increment of the magnitude of  $R$  and an attenuation of the magnitude of  $S$  as they propagate. In other words the terms that multiplies  $r_1$  and  $s_2$  in the above equations grow with increasing spatial coordinate  $z$ . This can be expresses as:

$$\text{Re}(\gamma) > 0 \quad (52)$$

The magnitude  $|R(z) + S(z)|$  is constant throughout the grating, so the combined effects (gain/coupling) from the two counter-propagating waves is power transfer from  $s_1 \rightarrow r_1$  and  $r_2 \rightarrow s_2$ .

Due to the mathematical description of  $R(z)$  and  $S(z)$ , the solution for the partial waves  $E_y^m$  (equation 24) is formed by a superposition of growing waves with propagation constant of  $\beta_0 - \text{Im}(\gamma)$  and decaying waves  $\beta_0 + \text{Im}(\gamma)$ . Then by substitution of the solution 50, 51 into 48 and 49, and collecting the terms with similar dependency:

$$\hat{\Gamma} r_1 = i(\kappa_p^* + \zeta_2) \exp(-i\Omega) s_1 \quad (53)$$

$$\Gamma r_2 = i(\kappa_p^* + \zeta_2) \exp(-i\Omega) s_2 \quad (54)$$

$$\Gamma s_1 = i(\kappa_p + \zeta_4) \exp(i\Omega) r_1 \quad (55)$$

$$\hat{\Gamma} s_2 = i(\kappa_p + \zeta_4) \exp(i\Omega) r_2 \quad (56)$$

where

$$\hat{\Gamma} = \left( \gamma - \hat{\alpha} - i\hat{\delta} \right) \quad (57)$$

$$\Gamma = \left( -\gamma - \hat{\alpha} - i\hat{\delta} \right) \quad (58)$$

Now if we impose boundary condition at  $z = \pm \frac{L}{2}$  then from equations 48 and 49,

we obtain:

$$\left( r_1 \exp\left(-\gamma \frac{L}{2}\right) + r_2 \exp\left(\gamma \frac{L}{2}\right) \right) \exp\left(i\beta_0 \frac{L}{2}\right) = \hat{\rho}_l \left( s_1 \exp\left(-\gamma \frac{L}{2}\right) + s_2 \exp\left(\gamma \frac{L}{2}\right) \right) \exp\left(-i\beta_0 \frac{L}{2}\right) \quad (59)$$

$$\left( s_1 \exp\left(\gamma \frac{L}{2}\right) + s_2 \exp\left(-\gamma \frac{L}{2}\right) \right) \exp\left(-i\beta_0 \frac{L}{2}\right) = \hat{\rho}_r \left( r_1 \exp\left(\gamma \frac{L}{2}\right) + r_2 \exp\left(-\gamma \frac{L}{2}\right) \right) \exp\left(i\beta_0 \frac{L}{2}\right) \quad (60)$$

where  $\rho_l$  and  $\rho_r$  are the reflexion coefficients at the grating facets. Then  $r_1$  and  $s_2$  can be eliminated from the above equations by using equations 53 and 56:

$$\left( \frac{i(\kappa_p^* + \zeta_2) e^{-i\Omega} s_1}{\hat{\Gamma}} e^{-\gamma \frac{L}{2}} + r_2 e^{\gamma \frac{L}{2}} \right) e^{i\beta_0 \frac{L}{2}} = \hat{\rho}_l \left( s_1 e^{-\gamma \frac{L}{2}} + \frac{i(\kappa_p + \zeta_4) e^{i\Omega} r_2}{\hat{\Gamma}} e^{\gamma \frac{L}{2}} \right) e^{-i\beta_0 \frac{L}{2}} \quad (61)$$

$$\left( s_1 e^{\gamma \frac{L}{2}} + \frac{i(\kappa_p + \zeta_4) e^{i\Omega} r_2}{\hat{\Gamma}} e^{-\gamma \frac{L}{2}} \right) e^{-i\beta_0 \frac{L}{2}} = \hat{\rho}_r \left( \frac{i(\kappa_p^* + \zeta_2) e^{-i\Omega} s_1}{\hat{\Gamma}} e^{\gamma \frac{L}{2}} + r_2 e^{-\gamma \frac{L}{2}} \right) e^{i\beta_0 \frac{L}{2}} \quad (62)$$

Since these two last equations are homogeneous in  $r_1$  and  $s_2$  the following relation can be obtained for the nontrivial solution :



$$\frac{\left(1 + i \frac{\rho_l \hat{\Gamma}}{(\kappa_p^* + \zeta_2)}\right) e^{-\gamma L}}{\rho_l + i \frac{\hat{\Gamma}}{(\kappa_p^* + \zeta_2)}} = \frac{\left(\rho_r + i \frac{\hat{\Gamma}}{(\kappa_p + \zeta_4)}\right) e^{\gamma L}}{1 + i \frac{\rho_l \hat{\Gamma}}{(\kappa_p + \zeta_4)}} \quad (63)$$

where

$$r_1 = \hat{\rho}_l e^{-i\beta_0 L} e^{i\Omega} \quad (64)$$

$$r_2 = \hat{\rho}_r e^{-i\beta_0 L} e^{i\Omega} \quad (65)$$

Now the new coefficients defined in equations 64 and 65, not only includes the reflectivities but the phases associated with the grating facets, and with the propagation of the wave through the grating ( $\beta_0 L$ ).

By combining equations 54, 55, 57 and 58 the following relation can be obtained:

$$\gamma = \frac{i\kappa_p}{2} \left( \frac{i\hat{\Gamma}}{\kappa_p} + \frac{i\kappa_p}{\hat{\Gamma}} \right) \quad (66)$$

By combining equation 63 and 66 and after considerable algebraic manipulation [17]:

$$\begin{aligned} & (\gamma L)^2 + (\kappa_p + \zeta_4)(\kappa_p^* + \zeta_2) \sinh^2(\gamma L) + \\ & 2i\gamma L(\kappa_p + \zeta_4)(\kappa_p^* + \zeta_2)(r_1 + r_2)(1 - r_1 r_2) \sinh(\gamma L) \cosh(\gamma L) = 0 \end{aligned} \quad (67)$$

The last equation is a complete description of the variables that relate to the threshold gain of distributed feedback lasers. Also when  $r_1$  and  $r_2$  are equal to zero in equation 67, it easy to see that the resulting expression is similar to that derived in equation 47.

It is important to emphasize that the performance of the lasers is very closely related to the  $\zeta_n$  parameters as well as the order of the grating, phases, and reflection coefficients, as can be seen in figure 2.3, and 2.4. Figures 2.3 and 2.4 show the coupling coefficient dependence of the normalized bottom width (WTN, see figure 2.1) for  $p=1,2$  respectively, for the semiconductor structure defined by figure 2.1. The lasing wavelength was around 1.5  $\mu\text{m}$ . To facilitate comparison, the bottom widths were normalized to the grating period. These figures are a comprehensive study of how the shape of the corrugation in trapezoidal gratings impacts for instance the coupling coefficient of the device. The curves produce an interesting result: the maximum coupling coefficient is obtained when the  $WTN = \frac{1}{2}$  in other words, when a grating resembles a rectangular corrugation (for  $p=1$ ). Also notice that for  $p=2$ , the coupling coefficient reaches a maximum for  $WTN = \frac{1}{4}$ .

Figure 2.5 and figure 2.6 show a relationship between threshold gain ( $\alpha L$ ) and detuning coefficient ( $\delta L$ ) as calculated from equation 66 and for the case of  $p=1$ . The  $\zeta_n$  parameters were ignored for this particular case, and the values of the reflectivities were chosen arbitrarily (0.565 and 0). As expected the greater the coupling coefficient the lower the threshold gain. The DFB with a phase corrugation  $(3/4)\pi$  presents a lower threshold gain compare with the zero-phase one. On the other hand, the zero-phase DFB shows a greater gain margin (separation between the threshold gains of two adjacent modes) than the  $(3/4)\pi$  phase DFB. The next chapter will describe in details those calculations for a polymer-based device and with the inclusion of the  $\zeta_n$  parameters.

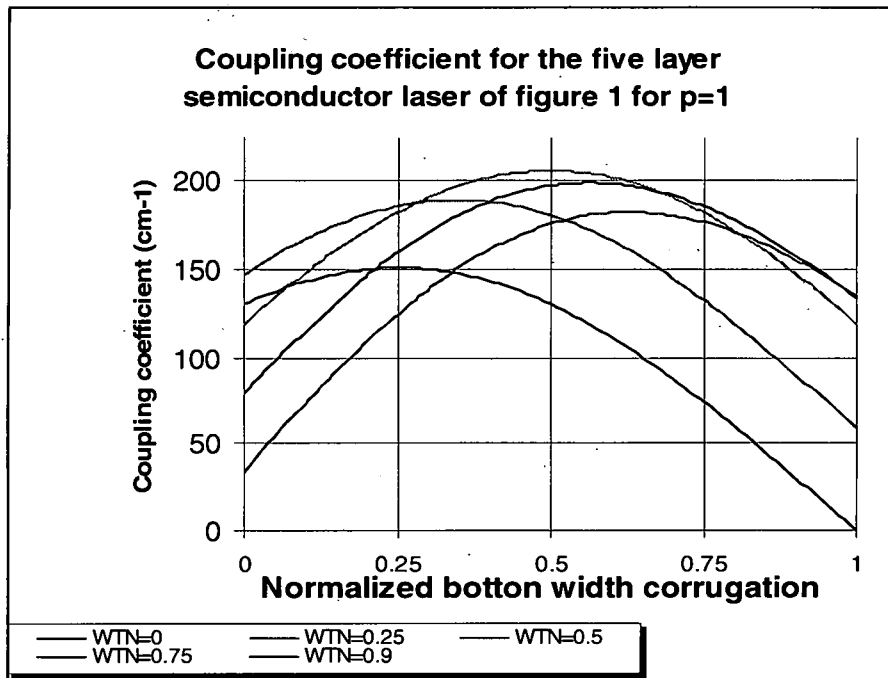


Figure 2.3 - Coupling coefficient dependence of the normalized bottom width corrugation for different values of normalized top width for  $p=1$ .

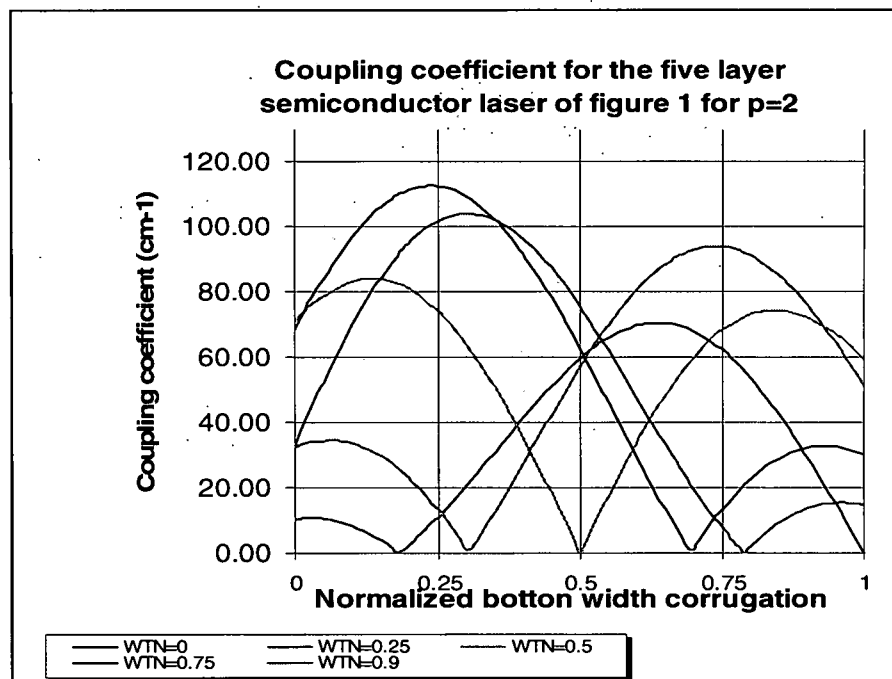


Figure 2.4 - Coupling coefficient dependence of the normalized bottom width corrugation for different values of normalized top width for  $p=2$ .

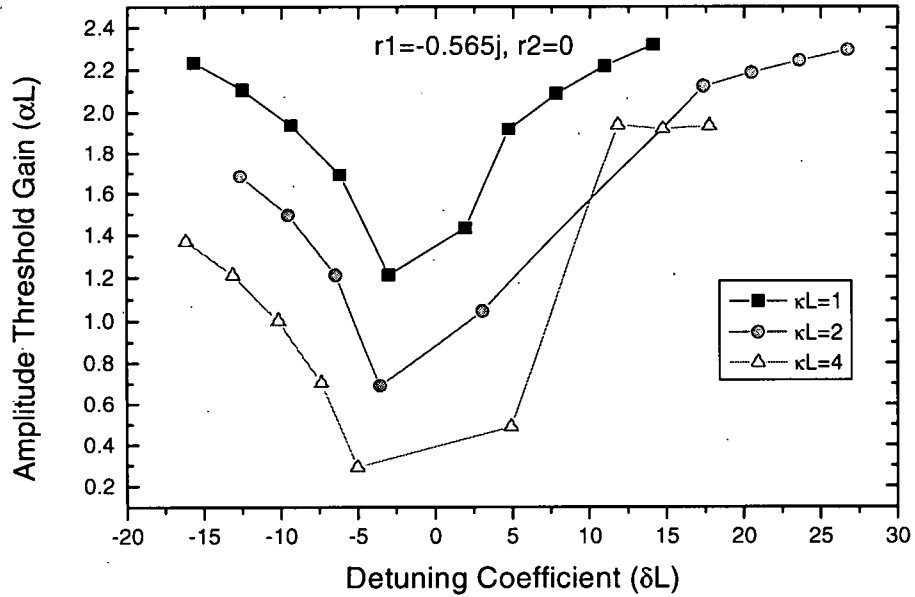


Figure 2.5 - Relationship between amplitude threshold gain ( $\alpha L$ ) and detuning coefficient ( $\delta L$ ) for the structure of figure 2.1. The values of the reflectivities were chosen arbitrary. The phase corrugation was  $(3/4)\pi$

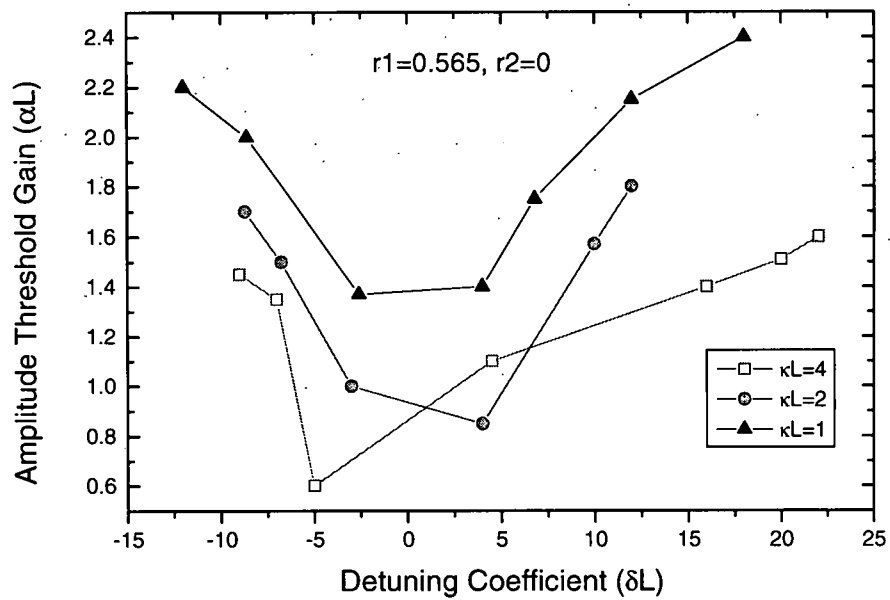


Figure 2.6 - Relationship between amplitude threshold gain ( $\alpha L$ ) and detuning coefficient ( $\delta L$ ) for the structure of figure 2.1. The phase corrugation was  $2\pi$ .

## Chapter III

### **Theoretical Simulation of 1-D Distributed Feedback Laser Based on [2-methoxy-5-(2'-ethylhexyloxy)-1,4-phenylenevinylene]**

#### *3.1 Introduction*

In this chapter the formalism from the previous chapter is used for the analysis of 1-D distributed feedback lasers. The analysis is based on actual devices that were fabricated. For ease of fabrication, the conductive polymer MEH-PPV ([2-methoxy-5-(2'-ethylhexyloxy)-1,4-phenylenevinylene] ) was chosen as the gain medium. The following chapters will describe the details of the photophysics of this polymer by analyzing its spectroscopy properties as well its suitability as a media for lasing applications.

For a meaningful analysis of the device performance, a reasonable corrugation shape must be assumed. The corrugation parameters that were used in this work are a consequence of the photolithography and device processing. Figure 3.1 shows the atomic force microscope (AFM) image of the 1-D photonic crystal structure on a photoresist layer.

The period of the corrugation was about 400 nm with an average depth of 70 nm. For calculation purposes this structure was approximated as a triangular shape. Figure 3.2 shows the complete structure for the polymer based 1-D distributed feedback laser. In the next chapter, a more detailed description of figure 3.2 will be presented.

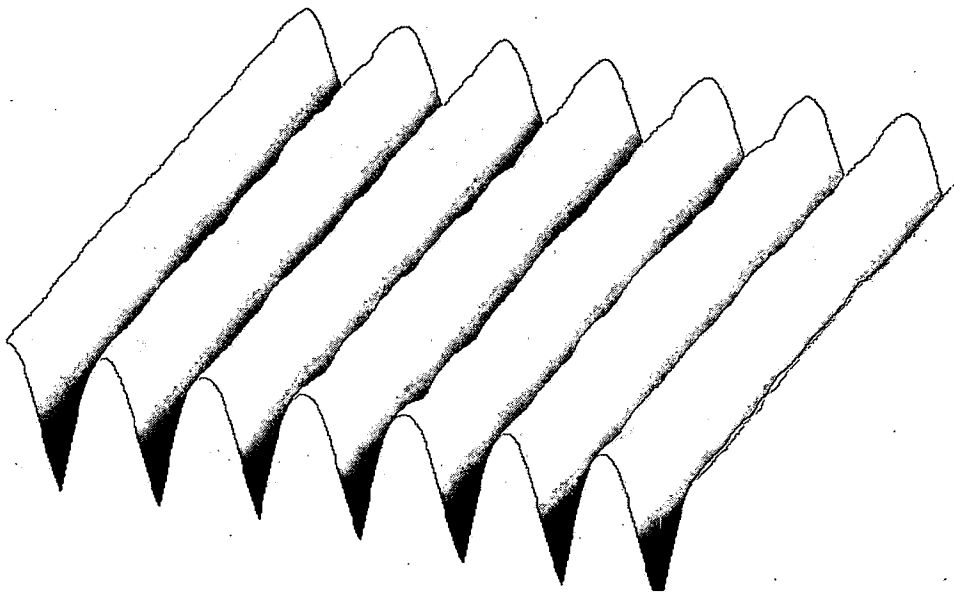


Figure 3.1 - Atomic force microscope (AFM) image of the 1-D photonic crystal structure. The period of the corrugation was about 400 nm with an average depth of 70 nm.

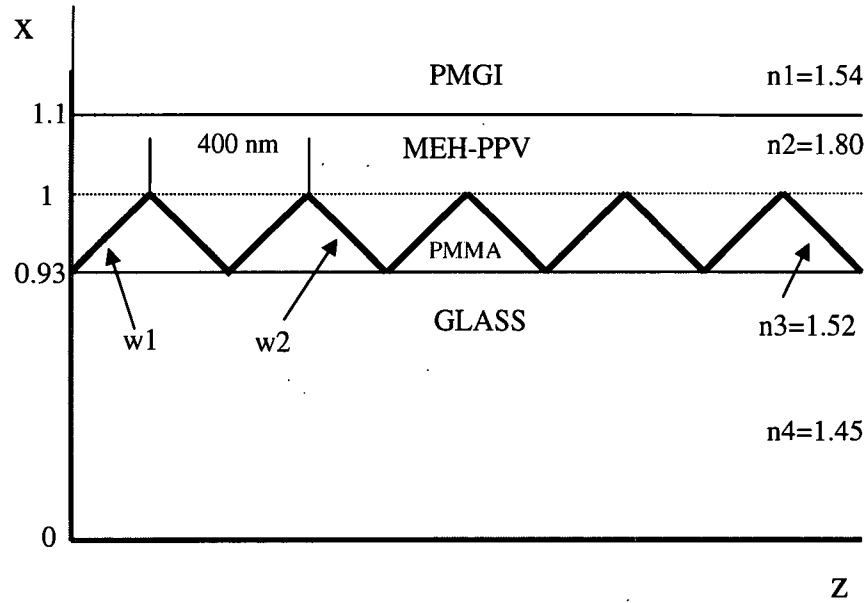


Figure 3.2. - Triangular grating approximation to the one-dimensional photonic crystal structure of figure 3.1.

### 3.2 Numerical solution for the Radiation and Decaying Modes

The first step is to determine the guided mode of the waveguide structure. The periodic corrugation in the refractive index creates some difficulties for estimating the refractive index profile used in Maxwell's equation (1). To overcome this problem, equation 4 and 6 provide expressions that describe the index of refraction of the corrugation. More specifically, equation 6 gives the value of the index of refraction at each point of the grating. In order to fully evaluate this equation, the functions  $w_1$  and  $w_2$  need to be determined. From figure 3.2 both  $w_1$  and  $w_2$  correspond to the equation of a straight line, which can be expressed as:

$$\begin{cases} w_1 = -2.857142857 \cdot x + 2.457142857 \\ w_2 = 2.857142857 \cdot x - 2.457142857 \end{cases} \quad 0.93 \leq x \leq 1 \quad (66)$$

Upon direct substitution into equation 6, the following relationship for the index of refraction can be obtained:

$$n_0(x) = \begin{cases} 1.54 & x \geq 1.1 \\ 1.8 & 1 \leq x, 1.1 \\ (-12.59428572 + 15.83428572 * x)^{0.5} & 0.93 \leq x < 1 \\ 1.46 & 0 \leq x < 0.93 \end{cases} \quad (67)$$

The implementation of equation 67 will allow us to determine the guided modes in the waveguide structure. The functional relationship in equation 67 for the interval  $0.93 \leq x < 1$  can be interpreted as the average index of refraction at a given position  $x$  that can be estimated by integrating the index of refraction function (discrete) over one grating period.

The index of refraction 67 returns 1.46 and 1.8 for  $x = 0.93$  and  $x = 1$  respectively, which ensures the continuity of the expression. Even though the index of refraction has square root functionality for  $0.93 \leq x < 1$ , it can be approximated as a straight-line for this interval as can be seen in figure 3.3. Figure 3.4 shows the complete index of refraction for the entire structure. We can now use standard numerical techniques to solve the wave equation to obtain the guided modes:

$$\frac{d^2 E_0}{dx^2} + [k_o^2 n_o^2(x) - \beta^2] E_0 = 0 \quad (68)$$



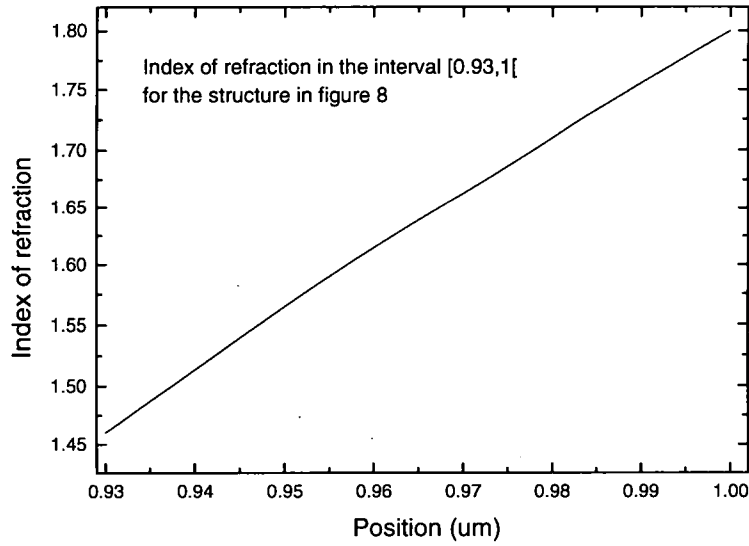


Figure 3.3 - Index of refraction dependence on the coordinate position ( $x$ ) in the interval  $0.93 \leq x < 1$  for the structure of figure 3.2. It illustrates that the relationship can be approximated as a straight line. This graph was included here because the program used to calculate the mode assumed a linear variation of the index of refraction in this interval.

Figure 3.5 shows the fundamental guide mode. To facilitate subsequent calculations the field has been normalized such  $\int_0^{2.4} E_0^2(x) dx = 1$ . The maximum intensity of the field happens to coincide with the corrugation position, which is desirable for a high coupling coefficient. The confinement factor around the corrugation layer is approximately 0.17. In order to evaluate equation 23 and thus to determine both the radiation and decaying modes that span the Floquet's theorem, the parameters  $A_q$  need to be determined. For the structure under study it is easy to show that:

$$A_q = \begin{cases} (0.148/q) * i * (\exp((-44.87 * X) + 38.6) * i * q) - \exp((-44.87 + 44.87 * X) * i * q) & 0.93 \leq x < 1 \\ 0 & x < 0.93, x \geq 1 \end{cases} \quad (69)$$

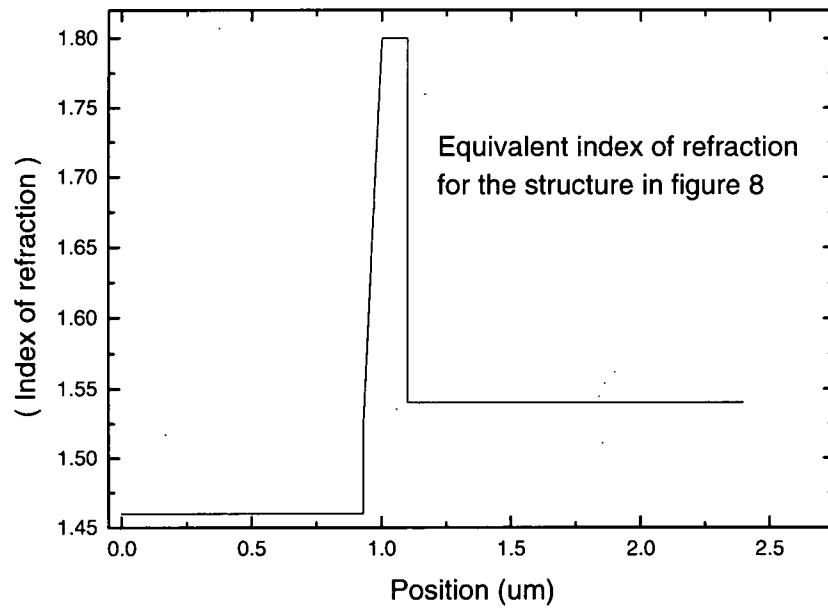


Figure 3.4 - Index of refraction dependence on the coordinate position (x) for the entire structure of figure 3.2.

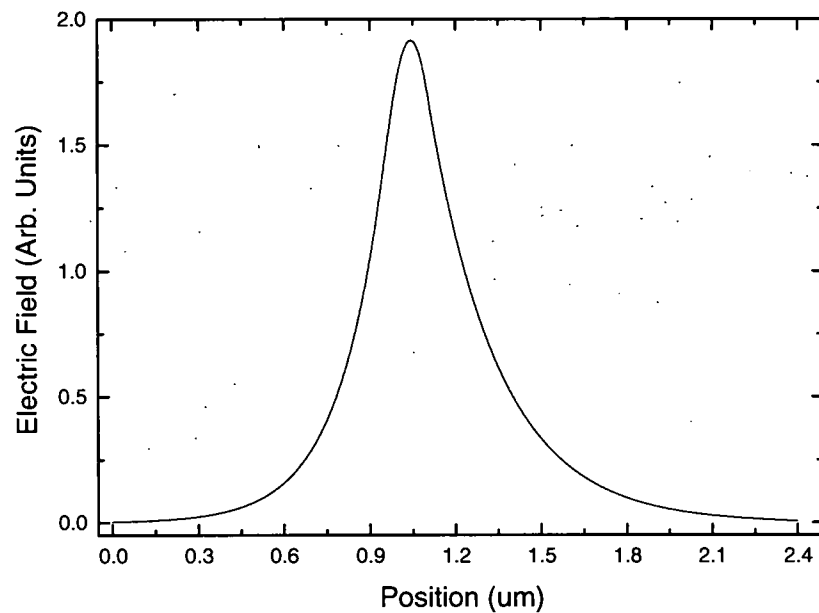


Figure 3.5 - Fundamental mode calculation corresponding to the structure defined in figure 3.2.

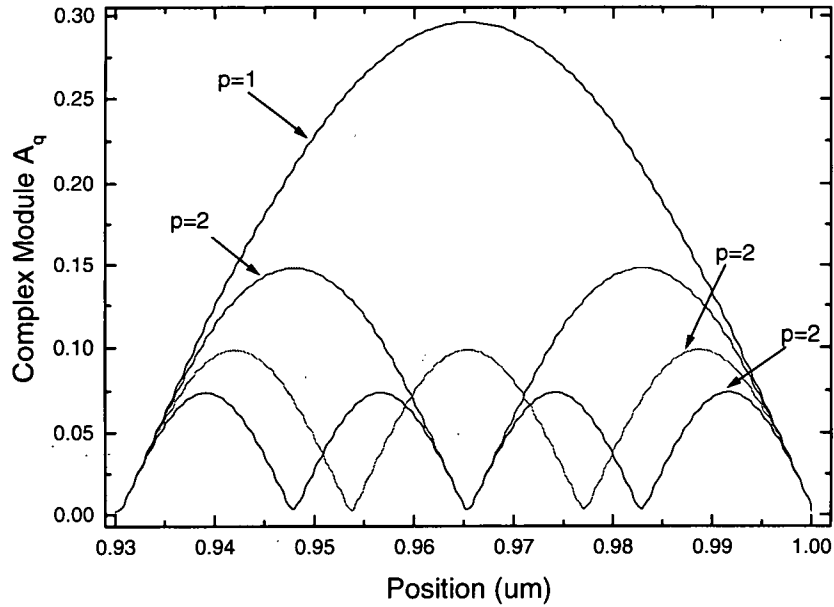


Figure 3.6 - First four orders corresponding to the complex module of  $A_q$  around the corrugation of the structure.

Notice that equation 69 has a complex form. and Since it is the term that drives the differential equation that describes both the decaying and radiating modes, complex solutions are expected for these fields. Figure 3.6 show the functional relationship of  $A_q$  for four different orders ( $q$ ).

In order to proceed with the calculations, the decaying and radiating modes need to be determined. An important point that needs to be taken into account regarding the formalism introduced in the latter chapter, it is related with the approximation inherits to the derivation. Merely the zero and  $p$  order modes contribute in generating the  $E_y^p$  modes. The latter approximation together with the slow envelope approximation constitute part of the theoretical framework used to derive this formalism.

The  $p$  and zero orders corresponding to equation 25 and 26 will be calculated later and these results will be used to compare against the fundamental mode of figure 3.5. Both  $p$  and zero orders have the same field distribution illustrated in figure 3.5. However they differ in the signs of their respective propagation constants. Higher order modes can be computed from the expressions of equations 25 and 26, in which  $E_0$  and  $E_p$  represents the driving fields calculated from equation 68.

$$\frac{d^2 E_m^0}{dx^2} + [k_0^2 n_0^2 - \beta_m^2] E_m^0 + k_0^2 A_m(x) E_0(x) = 0 \quad \forall m \neq 0 \quad (70)$$

$$\frac{d^2 E_m^p}{dx^2} + [k_0^2 n_0^2 - \beta_m^2] E_m^p + k_0^2 A_{m-p}(x) E_0(x) = 0 \quad \forall m \neq p \quad (71)$$

The above equations are equivalent to those presented in equations 25 and 26. However, we have eliminated the condition on  $m \neq p, 0$  imposed in these equations earlier. The reason is, as will be shown, when  $m=p$  and  $m=0$  in equations 70 and 71 respectively, the solution returns a scaled version of  $E_0(x)$ .

Here we will solve equation 70 and 71 through finite differences approximations:

$$\frac{d^2 E_m^i}{\Delta x^2} = \frac{E_{m_{j+1}}^i - 2E_{m_j}^i + E_{m_{j-1}}^i}{\Delta x^2} \quad (72)$$

Where  $E_{m_{j+1}}^i$  and  $E_{m_{j-1}}^i$  represent the electric field evaluated at the preceding and subsequent points respect to  $E_m^i$ . Standard Crank-Nicholson [18] differentiation can

also be used to approximate the second derivative in equation 72. By substituting equation 72 in 70 and 71 and organizing the terms, the following simplified equations are obtained:

$$\frac{E_{m_{j-1}}^0}{h^2} + \left[ k_0^2 n_0^2 - \beta_m^2 - \frac{2}{dx} \right] E_{m_j}^0 + \frac{E_{m_{j+1}}^0}{h^2} + k_0^2 A_m(x) E_0(x) = 0 \quad \forall m \ m \neq 0 \quad (73)$$

$$\frac{E_{m_{j-1}}^p}{h^2} + \left[ k_0^2 n_0^2 - \beta_m^2 - \frac{2}{dx} \right] E_{m_j}^p + \frac{E_{m_{j+1}}^p}{h^2} + k_0^2 A_{m-p}(x) E_0(x) = 0 \quad \forall m \ m \neq p \quad (74)$$

This representation allows changing the problem from a differential equation to an algebraic one. Notice also that the driving term in the above equations is independent of the variables, which also allows us treating the problem as a system of linear equations.

The terms  $A_m$  and  $A_{m-p}$  modulate the driving term  $E_0(x)$  and thus it is partially responsible for the profile of the  $E_m^i \ i=0,p$  fields.

We already have determined the guided mode  $E_0(x)$ , then for  $N$  points that defined  $E_0(x)$ ,  $N-2$  equations can be obtained from equations 73 and 74 respectively. For the system of equation to have a distinct solution two more equations are needed. In the present work, the transparent boundary condition (TBC) was employed to generate the two needed equations to completely define the problem.

The transparent boundary condition assumes that the electric field at the boundary can be written as:

$$E = E_0 \exp(ik_x x) \quad (75)$$

where  $E_0$  and  $k_x$  are complex. An important feature of the above assumption is that  $k_x$  is allowed to change as the problem progresses, thus eliminating the need for a problem-dependent adjustable parameter [19]. In the context of our simulation and using equation 75, the following equations can be obtained for the points at the boundaries of the computational grid:

$$\begin{cases} E_1 = E_0 \exp(jk\Delta x) \\ E_n = E_{N+1} \exp(-jk\Delta x) \end{cases} \quad (76)$$

where  $E_0$  and  $E_{n+1}$  are the electrical fields at points outside the boundary and thus the computational grid, and  $k_x$  can be defined as:

$$k_x = \sqrt{k_0^2 n_0^2 - \beta_m^2} \quad (77)$$

with

$$\beta_m = \frac{2\pi}{\lambda_g} + \frac{2\pi m}{\Lambda}$$

Using these points, the finite differences approximation can be applied to the boundary points. The final effect is that the problem has been expanded to an  $N+2$  equation with  $N+2$  variables for each field. Equation 78 illustrates the stated problem. The latter systems of linearly independent equations in conjunction with equation 76 needs to be solved in order to determine the decaying and radiating modes indicated with the superscript  $m$ .

$$\left[ \begin{array}{c} \frac{E_0^m}{h^2} \left[ k_0^2 n_0^2 - \beta_m^2 - \frac{2}{dx} \right] E_1^m \frac{E_2^m}{h^2} \quad 0 \quad 0 \quad 0 \quad 0 \quad 0 \quad 0 \quad 0 \quad 0 \quad \dots \quad 0 = k_0^2 A_m(x) E_0(x) |_{x \rightarrow E_1} \\ \frac{E_1^m}{h^2} \left[ k_0^2 n_0^2 - \beta_m^2 - \frac{2}{dx} \right] E_2^m \frac{E_3^m}{h^2} \quad 0 \quad 0 \quad 0 \quad 0 \quad 0 \quad 0 \quad 0 \quad \dots \quad 0 = k_0^2 A_m(x) E_0(x) |_{x \rightarrow E_2} \\ \frac{E_2^m}{h^2} \left[ k_0^2 n_0^2 - \beta_m^2 - \frac{2}{dx} \right] E_3^m \frac{E_4^m}{h^2} \quad 0 \quad 0 \quad 0 \quad 0 \quad 0 \quad \dots \quad 0 = k_0^2 A_m(x) E_0(x) |_{x \rightarrow E_3} \\ \downarrow \\ \frac{E_{n-1}^m}{h^2} \left[ k_0^2 n_0^2 - \beta_m^2 - \frac{2}{dx} \right] E_n^m \frac{E_{n+1}^m}{h^2} = k_0^2 A_m(x) E_0(x) |_{x \rightarrow E_n} \end{array} \right] \quad (78)$$

The structure described in figure 3.2 is designed with a second order diffraction grating, and in this sense the radiation mode (only one for a second order grating) will constitute the laser output and will irradiate power normal to the surface. This condition happens for  $m=-1$  in both equations 70 and 71. Figure 3.7 shows the field intensity of the calculated radiating mode. The minimum intensity for this field happens to be around both ends of the photonic crystal. Also notice that the field intensity at the top side of the photonic crystal is higher compared to the bottom side. In other words the laser output is asymmetrical and the beam propagating upward has higher intensity compare with the beam propagating downward. The reason for this asymmetry can be related to the index of refraction distribution. The effective index of refraction to the right of the grating is higher compared to the structure to the left of the grating. In this sense, a more symmetrical output can be obtained by increasing (by adding a buffer layer) the index of refraction to the left of the grating structure.

Another interesting observation about the systems of equation that define each radiating and decaying mode is that since the driving term is complex, the solution of the system of equation will be also complex. This is the reason for why the amplitude of the field has been plotted in figure 3.7. Figure 3.8 shows the real and imaginary parts corresponding to the field in figure 3.7.

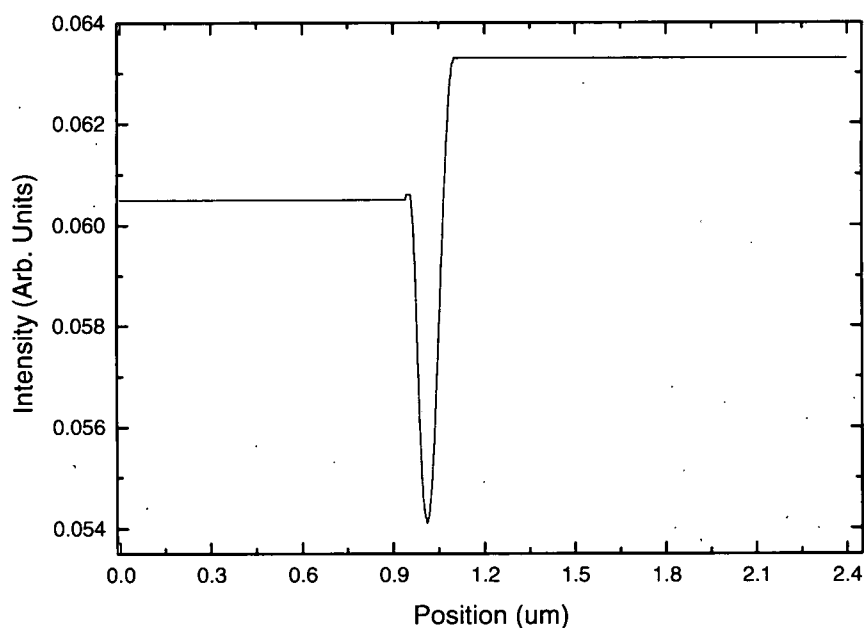


Figure 3.7 - Radiation mode calculation for  $m=-1$  in equation 78. The field intensity is constant at both sides of the corrugation, therefore describing a radiation mode.



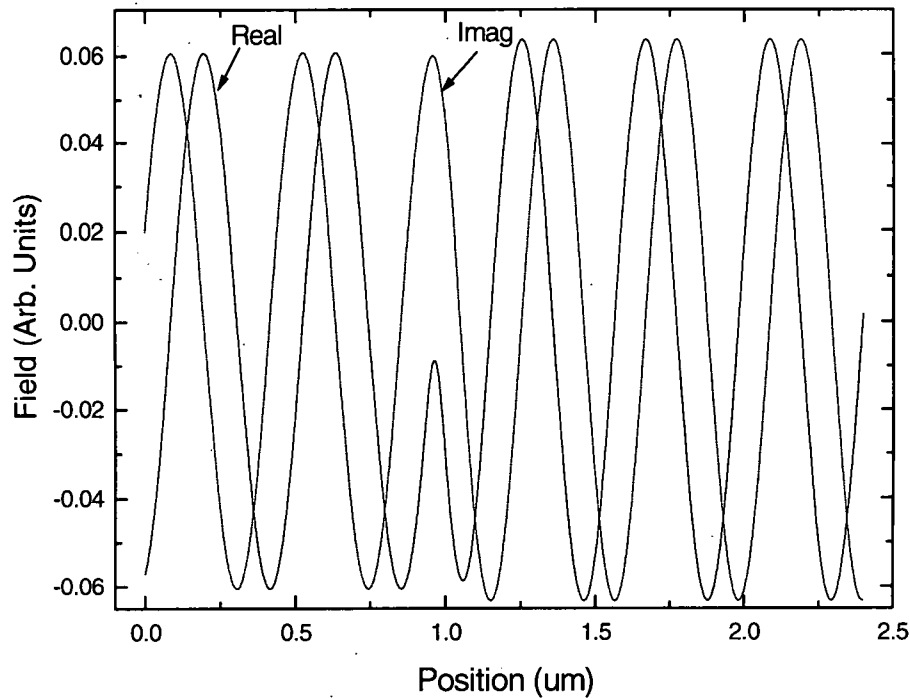


Figure 3.8 - Real and imaginary fields corresponding to the radiation mode for  $m=1$  in equation 78.

We have stated above that when  $p=m$ , the solution of equation 73 is similar to the zero order mode (defined by equation 68) but scaled in amplitude. To illustrate this process, figure 3.9 shows how the diffraction process coupled the forward and backward waves by means of a second order diffraction process. The first diffraction order couples part of the forward waves outside and normal to grating vector, and a second diffraction process couples the rest of the diffracted forward wave to the backward waves. In this sense the backward and forward waves have the same propagation constant (but different signs) and thus the same mode structure. Figure 3.10 shows the decaying mode intensity compared to  $m=-2$ . Notice that the mode is essentially similar to that calculated in figure 3.5. Moreover the field calculated in figure 3.5 is approximately 4.63 times the field calculated in figure 3.10.

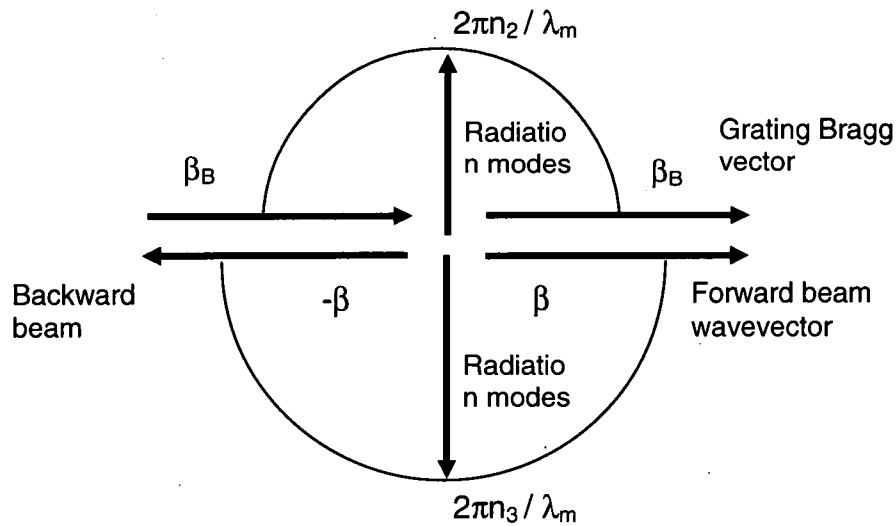


Figure 3.9 – Second order diffraction process in a surface emission DFB.

This is a very important step in our calculations. If the simulation is unable to match the fundamental mode with the mode corresponding to  $m=-2$ , it means that an error has been introduced in the computation, which can be used to validate the numerical procedure.

Also intuitively, the ratio between the intensities of the two modes is a measurement of the strength of the corrugation. The smaller the ratio the higher the grating strength, also the smaller the ratio the lower the threshold gain of the device and smaller the laser output (radiation mode).

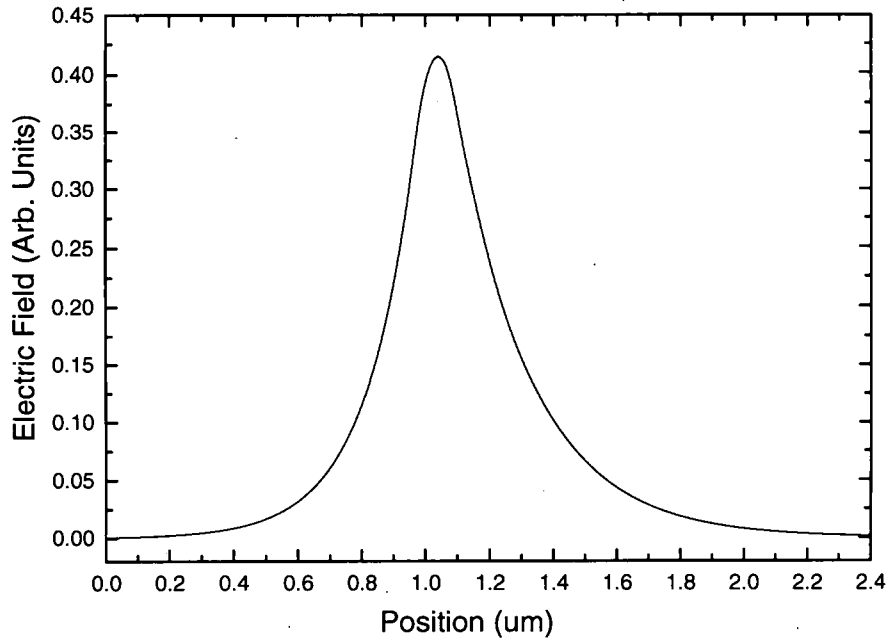


Figure 3.10 - Decaying mode corresponding to the structure defined in figure 3.2 and for the case of  $m=-2$ .

Others decaying modes corresponding to the fields defined by equation 70 and consequent from  $m=1$  to  $m=10$  are shown in figure 3.11. The calculation of these modes is essential for the determination of the  $\zeta_n$  parameter. Also it is important for practical considerations to determine when to truncate the calculation of these modes.

For instance, the peak intensity for the wave with  $m=10$  is about 5 order of magnitude smaller compared with the zero order mode as can be seen in figure 3.11. Also a correlation was found between the order  $m$  and the number of peaks in the field, and as discussed before, this has do the contribution of the  $A_q$ 's parameters in the eigenvalue equation. Even though some symmetry can be seen between the modes

with positive and negative values of  $m$ , important differences arise when comparing their amplitudes.

Figure 3.12 show the decaying modes defined for negative values of  $m$ . First notice that for  $m=-3$  only two peaks are noted in the field, the reason for that is related with both the radiation mode ( $m=-1$ ) and the decaying mode that couples the forward wave to the backward wave ( $m=-2$ ). In general the number of peaks is equal to the order of the mode for  $m < p$  and  $m > 0$ . Also the levels of intensity of the modes for negative values of  $m$  are higher compare with the positive ones. Also it is interesting to point out that the higher the intensity level of the mode corresponding to  $m=-2$  the faster the convergence of the infinite summation in equation 10.

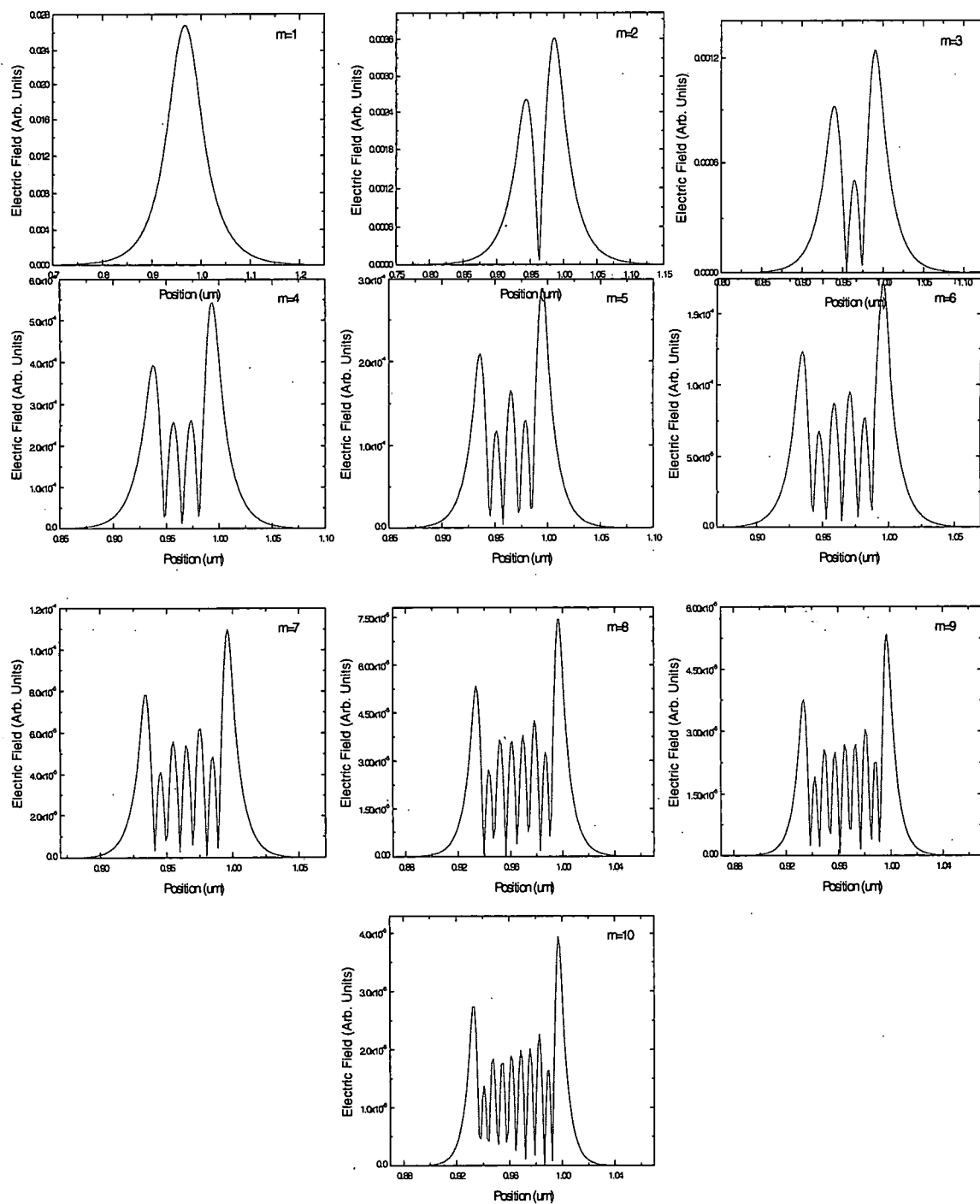


Figure 3.11 - Decaying modes calculated from equation 70 for positive values of  $m$ . The peak intensity for  $m=10$  is about 5 order of magnitude smaller compare with the fundamental mode.

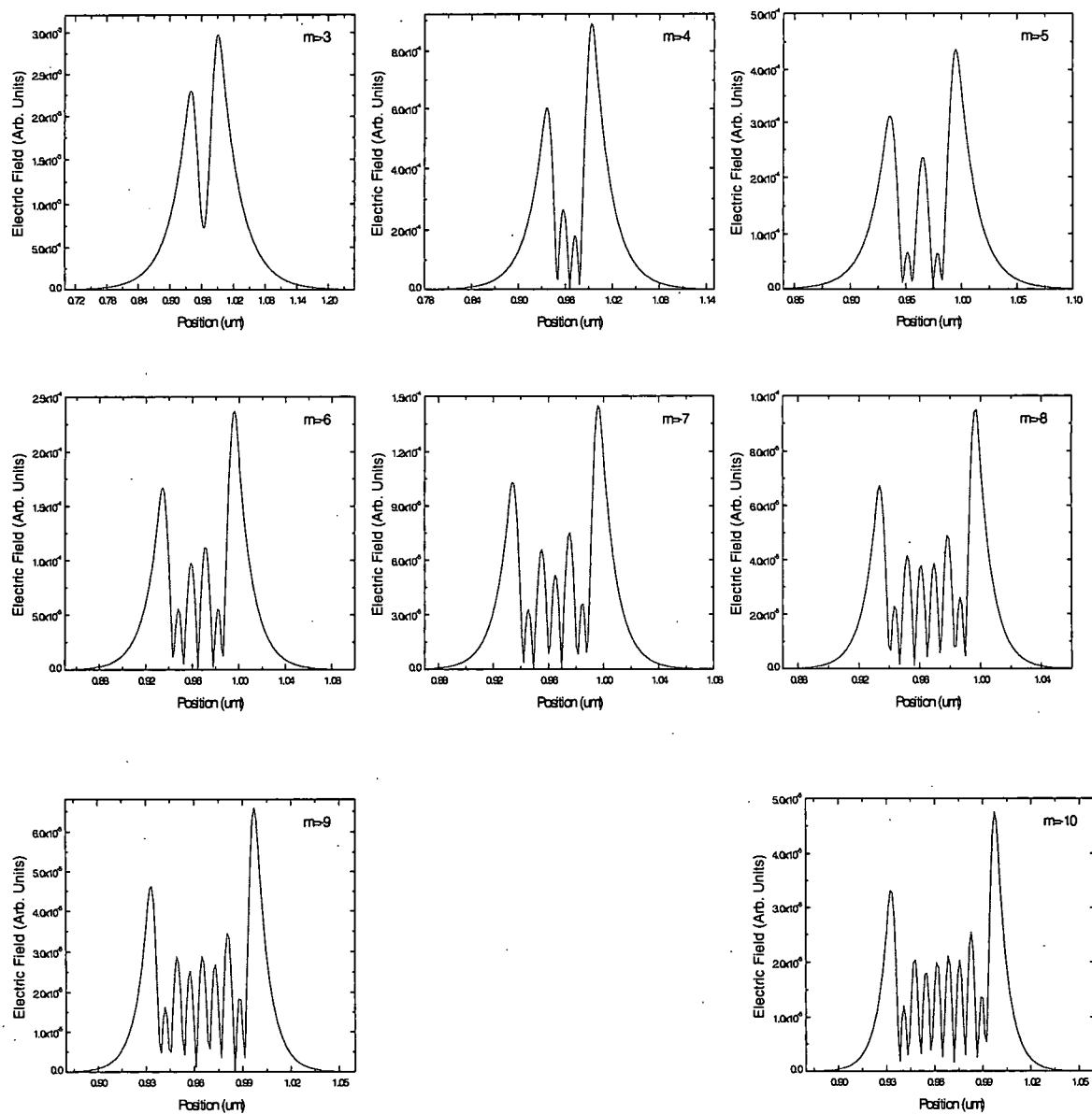


Figure 3.12 - Decaying modes calculated from equation 70 for negative values of  $m$ . The peak intensity for  $m=-10$  is higher in magnitude compare with  $m=10$ .

In order to complete the calculation of all modes, equation 71 needs to be evaluated. This equation differs from equation 70 basically in the  $Aq$ 's coefficients, in this particular case the  $Aq$ 's are computed by changing  $q$  for  $q+2$  in equation 69 (the  $q$ 's represents the mode order just as  $m$ ). Then it is straightforward to infer that the number of peaks in the field intensity of each mode is equal to  $m+2$ . In the same line of argument, the counter propagating modes are obtained for  $m=0$  compared to  $m=-2$  obtained from equation 71.

However the radiation mode happens at  $m=-1$  just as in equation 70. An interesting observation is that even though the modulus of the  $Aq$  coefficient for the counter propagating mode has been reduced compared to the same mode calculated from equation 70, the intensity level of both modes are similar. The same observation is true for the radiation mode in both equations. Figure 3.13 and 3.14 show the decaying modes for positive and negative values of  $m$  respectively.

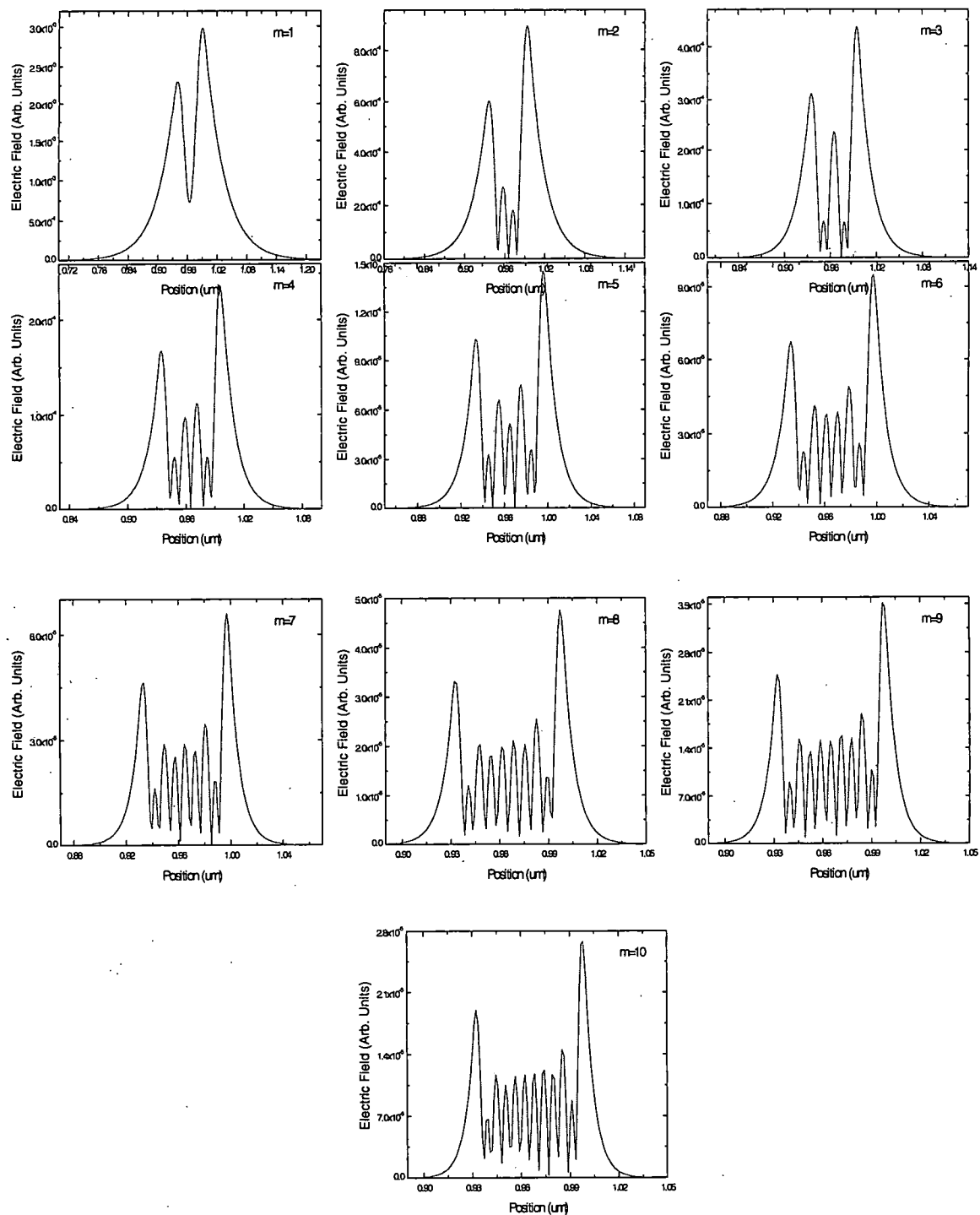


Figure 3.13 - Decaying modes calculated from equation 71 for positive values of  $m$ . The peak intensity for  $m=10$  is higher in magnitude compare with  $m=9$ .



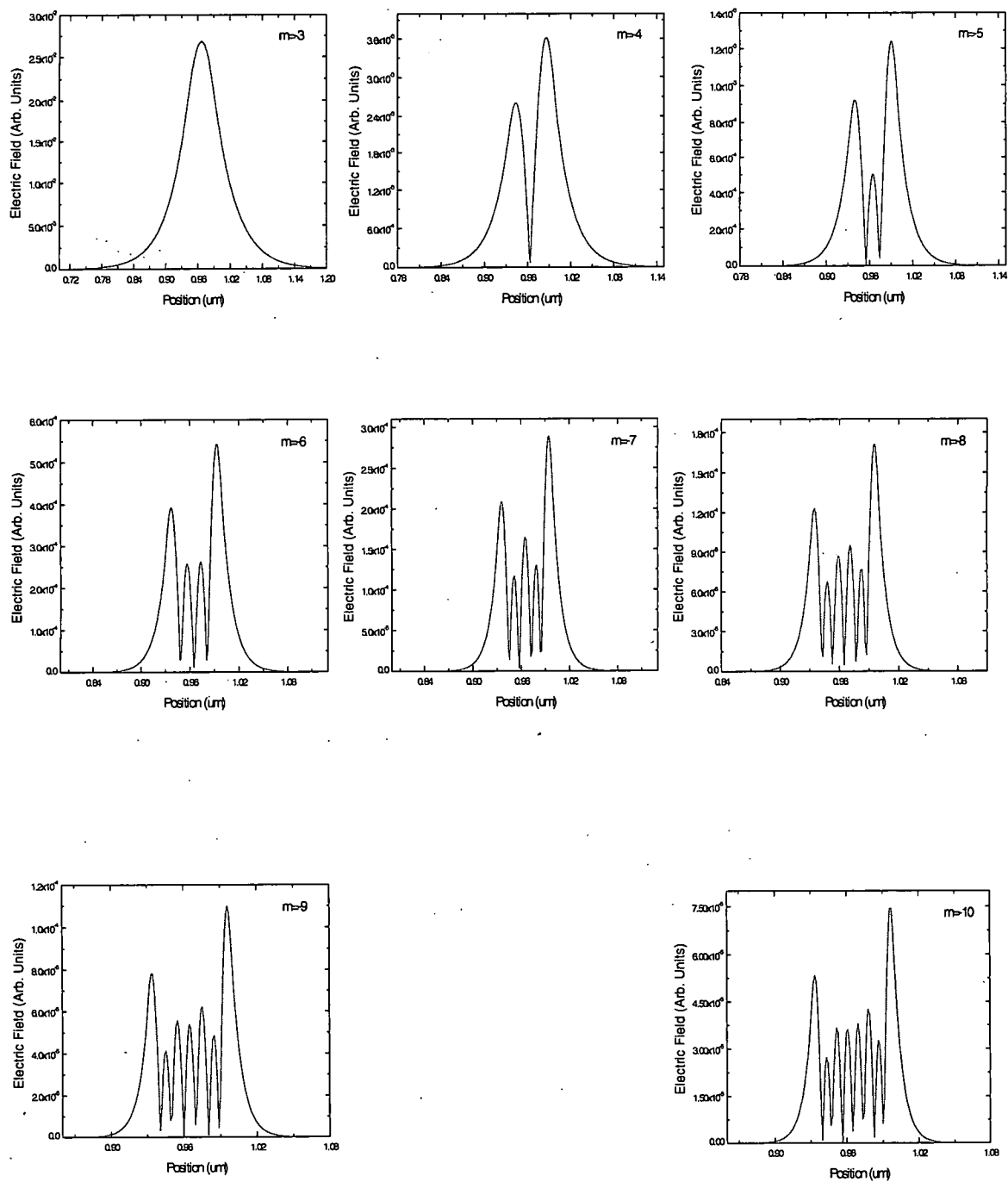


Figure 3.14 - Decaying modes calculated from equation 71 for negative values of  $m$ .

The final goal of the first part of our calculation is to construct the threshold gain equation for the waveguide structure defined in figure 3.2. To construct such an equation the coupling coefficient and the  $\zeta_n$  coefficients need to be determined. In the process of determining these parameters the zero order is employed to calculate the coupling coefficient. The decaying modes and the radiation mode are used for the determination of the  $\zeta_n$  coefficients. The counter propagating modes ( $m=-2, 0$  for equation 70 and 71 respectively) do not play any role in the calculation of these coefficients. The evaluation of equations 29-32 produce the following results:

$$\begin{aligned}
\zeta_1 &= -1.2776e-004 + 7.0851e-004i \\
\zeta_2 &= -1.3091e-004 + 7.0685e-004i \\
\zeta_3 &= -1.2927e-004 + 6.9800e-004i \\
\zeta_4 &= -1.1399e-004 + 6.9957e-004i \\
\kappa_p &= 1.193e-002 - 3e-004i
\end{aligned} \tag{79}$$

The first sanity check of this theoretical analysis is the reproduction of the guided mode obtained from equation 73 and 74 for  $m=-p, 0$  respectively. The  $\zeta_n$  parameters also provide useful information that can guide us in determining if the results obtained are accurate. For instance we have stated that the parameters  $\zeta_1$  and  $\zeta_3$  must be equal. In our calculations these parameters are the same within 1.4 %. Also,

since the grating structure is symmetrical  $\zeta_2 = \left( \frac{\kappa_p^*}{\kappa_p} \right) \zeta_4$  within 3.31 %. These results

validate the outcome of our numerical simulations. Appendix A shows the Matlab code used to generate these results.

### 3.3 Threshold gain Calculation

The threshold gain is one of the most important figures of merit of a distributed feedback laser. This analysis not only provides information about minimum gain that is needed to overcome losses in the waveguide structure, but it also provides details about the deviation of the lasing mode from the Bragg condition as well as mode discrimination (gain margin). The mode discrimination analysis is vital for the design of single longitudinal mode lasers, which is essential in optical communication. This characteristic is what makes DFB lasers unique compared to Fabry-Perot lasers. Large amplitude gain difference is a desirable characteristic to ensure large mode discrimination and single mode operation.

In our structure the laser output is normal to the grating surface. In this sense, it will be convenient to high-reflection coat the facets of the device in order to reduce the loss in the waveguide. This will translate in a reduction of the threshold gain of the laser. We choose  $r_1 = r_2 = 0$  in equation 67. Equation 67 then becomes:

$$(\gamma)^2 + (\kappa_p + \zeta_4)(\kappa_p^* + \zeta_2) \sinh^2(\gamma L) = 0 \quad (80)$$

Notice that the terms  $\zeta_2$  and  $\zeta_4$  appear implicit in the above equation, the term  $\zeta_1$  (and thus  $\zeta_3$ ) are included explicitly in the  $\gamma$  parameter. The problem in hand is therefore to find numerical solution to equation 80.

The solution of equation 80 can not be expressed as a closed expression and therefore needs to be solved numerically. Besides, its solution is not unique, and consequently a collection of solutions can be generated. The solution (each solution is characterized by a gain and the corresponding detuning coefficient) with the lowest gain value defined as the threshold gain of the device. Obviously the length of the device affects the threshold gain and the detuning coefficient of the device as can be inferred from equation 80.

The solution of equation 80 implies indirectly the solution for both the threshold gain  $\alpha$  and the detuning coefficient  $\delta$ . A natural way of solving equation 80 is by discomposing it in both its real and imaginary parts. Thus if equation 80 is written as:

$$W = (\gamma)^2 + (\kappa_p + \zeta_4)(\kappa_p^* + \zeta_2) \sinh^2(\gamma L) \quad (81)$$

then the problem is reduced to a system of two transcendental equations with two variables:

$$U = \text{Re}(W) = 0 \quad (82)$$

$$V = \text{Im}(W) = 0 \quad (83)$$

Notice that in equation 81  $\gamma$  is a complex variable. In order to be able to solve equations 82 and 83 the following substitution must be made:

$$\gamma = x + iy \quad (84)$$

In this sense the system of equation described in equations 82, 83 can now be solved in terms of  $x$  and  $y$ . Streifer et al [17] has suggested an Newton-Rapson subroutine to solve the system of equation.

This method is accurate and not very difficult to implement. However, special care must be taken in selecting the initial guessing point. In other words, the subroutine may generate the same pair of solution for different starting points. To circumnavigate this problem we used a semi-graphical approach.

Using this method we first plot equation 82 and 83 and the intersection of both graphs will determine roughly the solution of the system of equations. Now we can use standard algorithms to solve equation 82 and 83 numerically by choosing the appropriate interval for the root solving subroutine.

The solution of equations 82 and 83 do not directly provide the threshold gain and the detuning coefficient, since  $\gamma$  is also a function of the  $\zeta_n$  parameters as well as the coupling coefficient. In order to obtain these quantities, it is necessary to solve the system of equations below:

$$\begin{aligned}\alpha &= \text{Re} \left[ (x + iy)^2 - (\kappa_p + \zeta_4)(\kappa_p^* + \zeta_2) \right]^{\frac{1}{2}} - i\zeta_1 \\ \delta &= \text{Im} \left[ (x + iy)^2 - (\kappa_p + \zeta_4)(\kappa_p^* + \zeta_2) \right]^{\frac{1}{2}} - i\zeta_1\end{aligned}\tag{84}$$

As can be inferred from equation 80,  $\gamma$  is function of 4 predetermined constants and the device length ( $L$ ). In order to produce a dimensionless analysis, the results will be presented as function of  $\alpha L$  and  $\delta L$  respectively. Appendix B shows the Maple's

code used to solve the threshold gain and the detuning coefficient. Figure 3.15 shows the threshold gain analysis for the structure of figure 3.2, for 4 different device lengths. These solutions represent the allowing modes in the DFB laser.

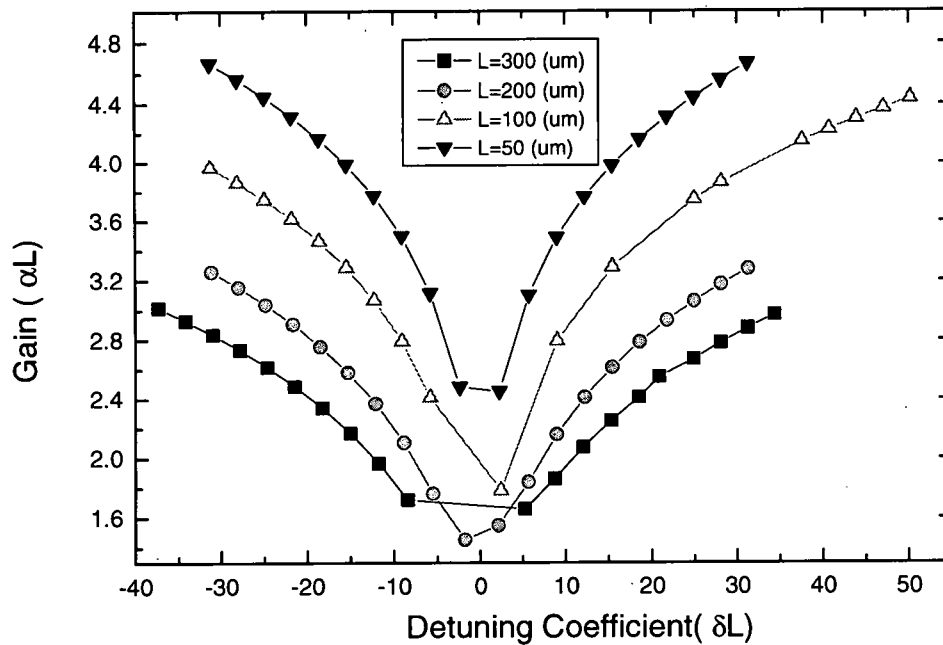


Figure 3.15 - Thresholds gain and detuning coefficients for the longitudinal modes in the DFB structure defined in figure 3.2. The values in this graph were calculated using the maple's code of appendix B.

Figure 3.15 shows that as the device length increases a reduction of the threshold gain is seen. However when the device length increases from 200  $\mu m$  to 300  $\mu m$ , the threshold gain increases. These results illustrate the important effect of the radiation modes in the threshold gain calculations. In previous analysis<sup>8,9</sup> the threshold gain was always found to decrease with the increase of device length. An increase of the device length beyond certain values will, in addition to increasing the feedback

mechanism, will also increase the losses due to the  $\zeta_{n=1,3}$  parameters. Consequently an increase in the threshold gain at 300  $\mu\text{m}$  is observed.

In optical communication and due to dispersion consideration, it is imperative that the laser operates within one longitudinal mode. An important characteristic that measure the ability of the laser to remain single mode is the concept of gain margin. Gain margin measures the difference between the lasing mode (threshold gain) and the most probable side mode. A large gain margin is desirable because it implies that more gain can be introduced in the laser structure without the excitation of new longitudinal modes. The mode discrimination is then an essential parameter in the performance of a DFB laser. As can be interpreted from figure 3.15, the device with length of 100  $\mu\text{m}$  presents the best gain margin characteristic. A further increase of device length does not produce substantial decrease of the device threshold, besides the larger the device the smaller the throughput per wafer. Therefore 100  $\mu\text{m}$  represent the optimum length for the device described in figure 3.2. Figure 3.16 shows a flowchart that illustrate the steps necessary to analyze the 1-D DFB laser.

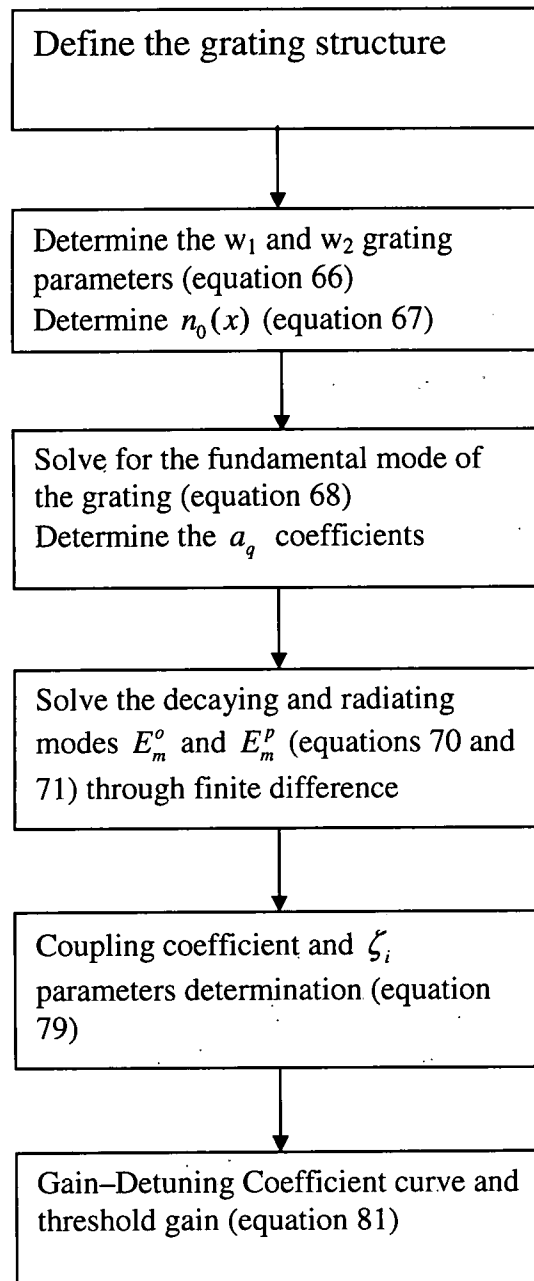


Figure 3.16 – Flowchart that illustrates the solution procedure for the 1-DFB laser threshold gain determination.



## Chapter IV

### **Experimental Results From 1-D Distributed Feedback Lasers Based on [2-methoxy-5-(2'-ethylhexyloxy)-1,4-phenylenevinylene]**

This chapter presents the optical characterization and laser action from 1-D distributed feedback lasers based on the polymer 2-methoxy-5-(2'-ethylhexyloxy)-1,4-phenylenevinylene] (MEH-PPV) as the gain media for the lasing studies in this work. The first part of this chapter develops the spectroscopy properties of MEH-PPV. Later the device fabrication and characterization is introduced. At last the laser action is presented.

#### *4.1 Conjugated Polymers*

Conjugated polymers, also known as conductive polymers, are organic macromolecules, which consist of alternating single and double bonds between carbon atoms on the polymer backbone. Conjugated polymers are semiconductors, therefore they have a band gap and their conductivity can be varied through doping (usually p-doped). Conjugated polymers derive their semiconducting properties from having delocalized  $\pi$  - electron bonding along the polymer chain [20].

Notable progress has been made in the field of conjugated polymer since the discovery by Hideki Shirikawa of polyacetylene, the first polymer capable of conducting electricity [21]. The subsequent discovery by Alan J. Heeger and Alan G.

MacDiarmid [22] that oxidative doping can increase the conductivity of the polymer about 12 orders of magnitude opened very exciting opportunities for optoelectronic applications. For the discovery and development of conductive polymer Alan J. Heeger, Alan G. MacDiarmid, Hideki Shirakawa received the Nobel Prize in Chemistry 2000. Electroluminescence from conjugated polymers was first reported using poly(phenylene vinylene) (PPV) [23] in 1990.

Besides the conductivity and the photoluminescence, there are other properties that a conjugated polymer must have in order to be suitable for lasing applications. It is convenient that the structure of the energy level support a four-level system to avoid a overlapping between the ground state absorption and the stimulated emission. Nearly all polymers can be described as a four-level system, since their vibronic structures are quite similar to the energy level structures of dye lasers [24]. Also due to the variation of the conjugation length throughout the polymer, a variation in band gap is verified allowing energy transfer along the polymer film [25]. Another attractive advantage of conjugated polymer for lasing application is the high luminescence and high density of chromophore even at high concentration [26], which is advantageously compares to other laser materials such as rare earths and dyes, whose luminescence quench with an increase in the concentration. Also, the absorption cross section of many conjugated polymers is considerably large (about  $10^{-15} \text{ cm}^2$ ) [27]. In order for a material to be suitable for laser applications it is necessary that the stimulated emission does not have other competitive processes. Non-radiative (NR) transitions, excited state absorption and triplet absorption are

processes that can inhibit the stimulated emission in a conjugated polymer. Figure 4.1 illustrates the excited state absorption processes.

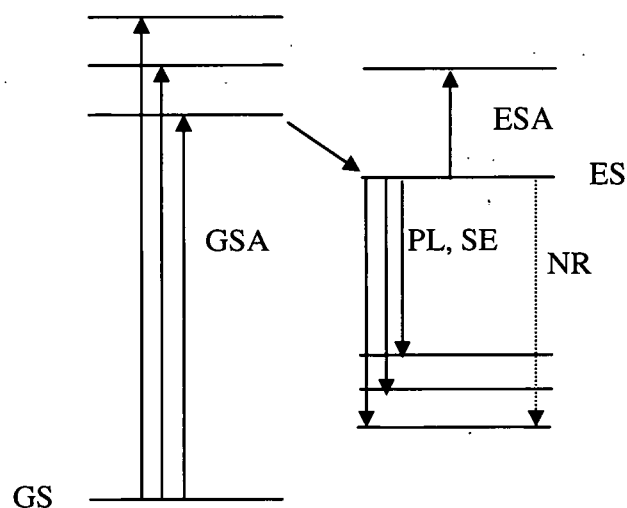


Figure 4.1 - Four-level energy diagram for a conjugated polymer. The ground state (GS) can be pumped to the ground state absorption (GSA), a relaxation process cascade the electron to the excited state (ES).

## 4.2 MEH-PPV Characterization

### 4.21.1 Introduction

Conjugated conducting polymers have been the subject of intense theoretical and experimental study due to their promising applications in optical and electronic devices. Among the conjugated polymers, poly[2-methoxy-5-(2'-ethylhexyloxy)-1,4-phenylenevinylene] (MEH-PPV) has become very attractive because it can be excited both electrically and optically, providing versatility and convenience. Applications such as light emitting diodes (LEDs) [28], photovoltaic cells [29], photodetectors [30], and field effect transistors [31] have been realized based on MEH-PPV. The commercial potential of these devices resides in their ease of

fabrication, since conjugated polymers can be deposited and patterned by inexpensive techniques such as spin coating or ink jet printing on a variety of substrates, including flexible ones [32].

One of the first demonstrations of lasing action in MEH-PPV was reported by Lawandy et al [33] from optically pumped MEH-PPV solutions containing colloidally suspended titanium dioxide ( $\text{TiO}_2$ ). In this device the titanium dioxide particles scatter the emitted photons in the MEH-PPV molecules in such a way that the feedback obtained from the scattering processes exceeds the losses above threshold. More recently Turnbull et al [34] presented the first demonstration of lasing action from films of MEH-PPV. In this configuration the device was held under vacuum to prevent photooxidation and the subsequent degradation of the device.

The next sections present the spectroscopic properties of MEH-PPV as well as the laser characteristics from 1-D distributed feedback laser.

#### *4.2.2 Sample Preparation and Optical Characterization*

Gilch-type MEH-PPV was purchased from Aldrich with average molar number  $M_n=70,000-100,000$  g/mol. MEH-PPV solutions were prepared from chlorobenzene, toluene, and tetrahydrofuran (THF) toluene at three different concentrations (0.38, 2, and 5 g/dm<sup>3</sup>). To enhance the dissolution process, the solutions were placed in an ultrasonic bath for 6 hours and kept in a dark environment at room temperature until ready for characterization. The thin films were prepared by

spin-coating the solution onto microscope slide substrates from the various concentrations at a spin speed of 1200 rpm for 30 seconds. The average thickness of the samples spun from the  $5 \text{ g/dm}^3$  concentration were about 100 nm as measured by a Tencor model P10 surface profilometer. The absorption profiles were measured with a model 8453 Hewlett-Packard spectrophotometer. For the photoluminescence (PL) and amplified spontaneous emission measurements, the excitation source was a Q-switched frequency-doubled, Quanta Ray (Spectra Physics) Nd:YAG laser operating at 532 nm, 2.5 ns pulse length with a repetition rate of 10 Hz. An HR2000 Ocean Optics fiber-coupled CCD spectrometer with a resolution of 0.1 nm was used to record the spectra.

#### *4.2.3 Absorption spectrum*

Figure 4.2 shows the absorbance spectrum of MEH-PPV films at room temperature prepared from the  $5 \text{ g/dm}^3$  solutions. As the concentration was increased a slightly blue shifted spectrum was observed (not shown in the figure). This indicates that the polymer chains in the film spun from the more dilute solution are more extended and the  $\pi$  electrons in the polymer backbone have a longer conjugation length. Notice also that the spectrum is somewhat red shifted in the THF film compared to the chlorobenzene and toluene films.

Two absorption bands are obvious, and the one in the visible region with a peak around 510 nm has the largest transition probability. The other peak is located in the UV region around 335 nm and corresponds to the phenyl group of the polymer.

The strength of this transition was stronger in THF compared to the other solvents. A possible explanation for the greater strength of this transition in THF compared to the chlorobenzene and toluene may be related with the amount of aggregation formed by the dissolution process. Aggregation happens more readily in chlorobenzene and toluene. Aggregates are lower band gap species compare to the isolated polymer chains. As a result, there will be more absorption species in the UV region for THF compared to the other solvents due to its lower aggregation formation. The amplitude of the absorption spectra was found to decrease with increasing temperature in an oxygen rich environment, indicating the formation of oxidized products.

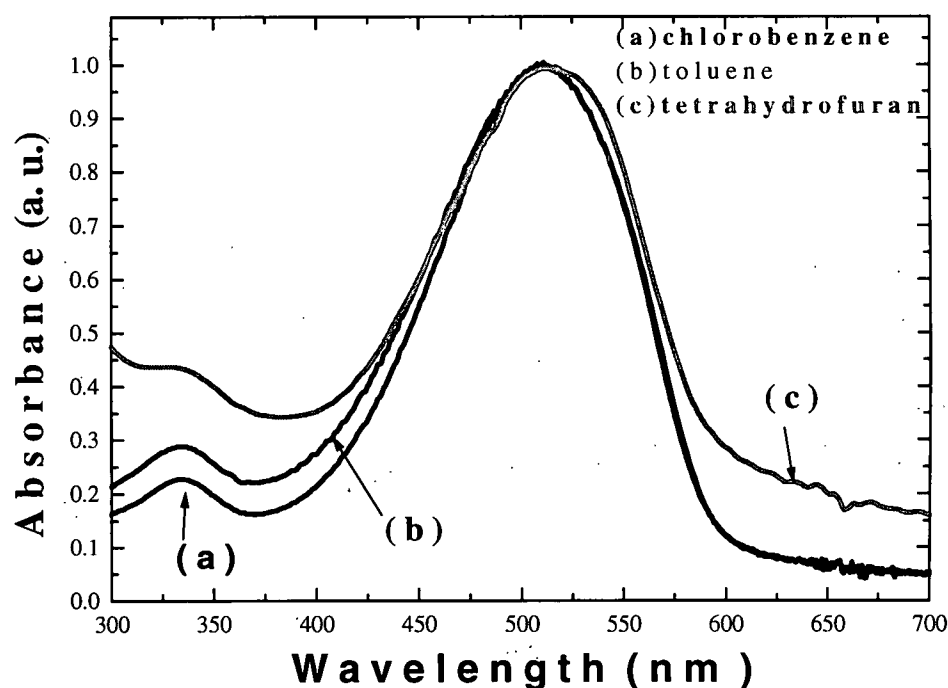


Figure 4.2 - UV-vis absorption spectra of thin film of MEH-PPV in different solvents. The films were cast from the 5 g/dm<sup>3</sup> solution. The inset shows the chemical structure of MEH-PPV.

#### *4.2.4 Excitation Spectrum of MEH-PPV in Films*

Since the spectral line narrowing is occurring mainly around 640 nm, it is important to determine the most appropriate wavelength to excite the polymer, to ensure maximum absorption at this wavelength. This information it is not provided by the absorption spectra, since absorption only provide an integrated value (absorption at all wavelength) and also they do not generate any information regarding phonon distribution and therefore no information about radiative and nonradiative transitions.

The excitation experiments are performed by exciting the samples at different wavelength and recording the photoluminescence at a specific wavelength. In this way the best wavelength, which will account for both absorption and radiative transition can be determined. Figure 4.3 shows the excitation spectra for a film spun from the chlorobenzene solution. The emission wavelength was 640 nm. It is evident that the best wavelength for this transition is around 500 nm. However due to equipment limitations, the photoluminescence and lasing studies were be conducted with a 532 nm YAG laser.

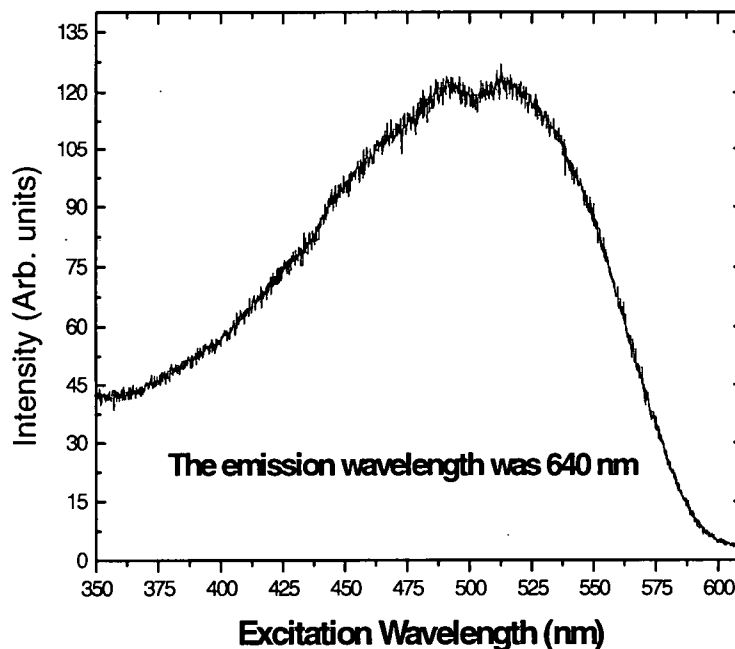


Figure 4.3 - Excitation spectra of MEH-PPV thin film. The emission wavelength is 640 nm. The best pumping wavelength for this transition is around 511 nm.

#### *4.2.5 Photoluminescence and Spectral Line-Narrowing of MEH-PPV in solution*

Figure 4.4 shows the experimental setup used to obtain the photoluminescence (PL) and the spectral line-narrowing (SLN) spectra. The Figure 4.5 shows the PL and SLN emission spectra of MEH-PPV in solution at different concentrations in chlorobenzene (2a), toluene (2b), and tetrahydrofuran (2c) respectively. The PL and SLN spectra have been normalized to facilitate comparison. The PL profiles show two emission peaks. The first one is located at 557, 561 and 566 nm in THF, chlorobenzene and toluene respectively.



The second peak was found to be dependent on solution concentration and appeared at 596, 604 and 599 nm respectively and is due mainly to the second vibronic transition of the polymer and to a less extent to the formation of aggregated species. The emission wavelengths of the aggregates species is roughly the same as the vibronic transition of the isolated polymer chains.

Aggregation is the result of interchain interactions that form electronic species with ground and excited state properties different from an isolated polymer chain. The level of aggregation increases with concentration. If the excited state wave function is delocalized over two or more polymer chains and charge separation occurs (so the electron resides only on one chain) the interchain species is referred to as a polaron pair [35]. If there is no significant charge separation the species is referred to as an excimer [36]. Delocalization of the wave function over multiple chains in the ground state has also been reported [37].

In dilute solution (where very little or no aggregation is formed) it is well accepted that photoexcitation creates only one electronic specie in which the PL spectrum shows a peak roughly at the same position as the aggregates [38]. Notice also that aggregation is also a function of the chemical nature of the solvent. The amount of aggregation is obviously higher in toluene and chlorobenzene compared to THF. Aggregation happens more readily in aromatic solvents such as chlorobenzene which interacts preferentially with the aromatic backbone of the polymer chain. On the other hand, nonaromatic solvents such as THF are more likely to interact with

the side groups of the polymer, thus causing the polymer chains to form tight coils and minimize the exposure of the backbone thus reducing the formation of aggregates [39].

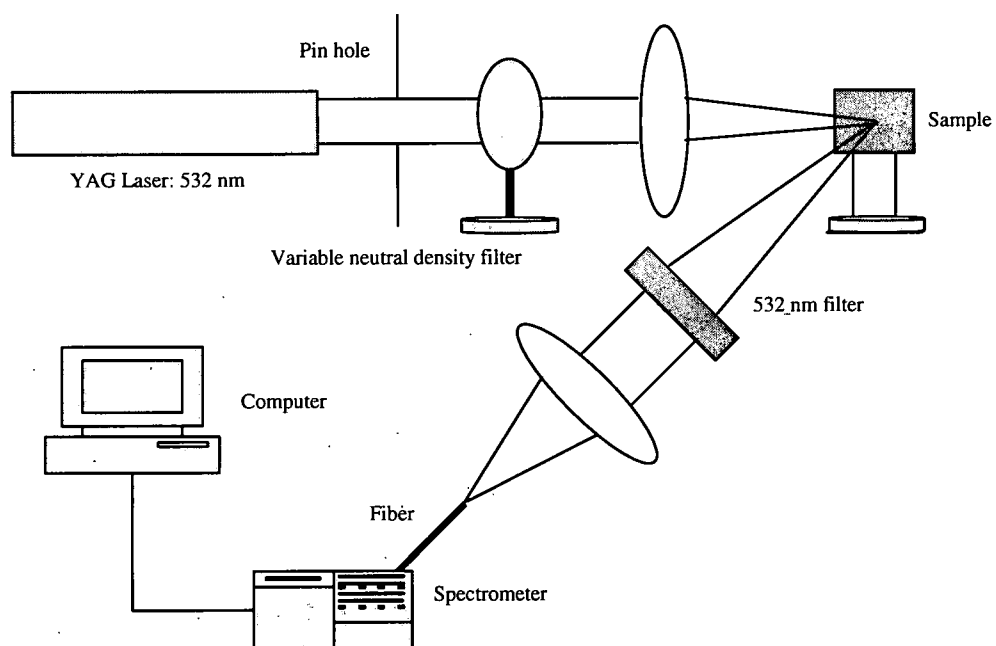


Figure 4.4 - The experimental setup for the PL and ASE measurements

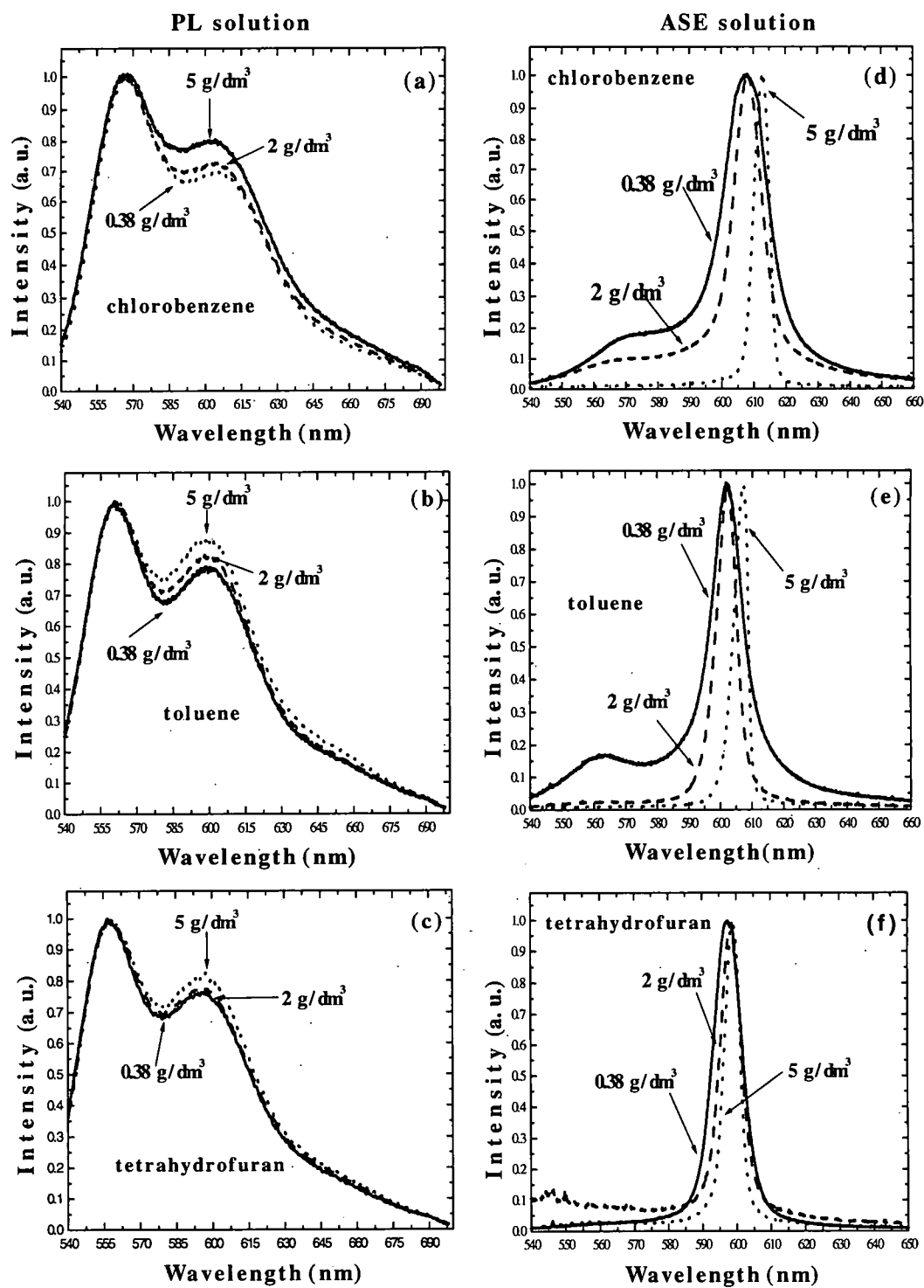


Figure 4.5 - Photoluminescence (a,b,c) and spectral line narrowing (c,d,e) spectra of MEH-PPV at different concentrations in solution and in different solvents. The excitation source was a Nd:YAG pulsed laser operating at 532 nm.

#### 4.2.6 Triplet State Absorption

It is important to point out that a pulsed excitation source must be employed to observe line-narrowing effects in MEH-PPV. The situation is better illustrated in figure 4.6. The figure illustrates electronic transitions involving both singlet (all electrons are spin-paired) and triplet (one set of electrons is unpaired) states. Upon excitation electrons from the ground state are absorbed into the singlet states where vibrational relaxation reduced the energy of the electrons to the bottom of the singlet band. Two mechanisms may occur: fluorescence in which the electron relax to the ground states and intersystem crossing which transfer the electrons to the allowed triplet states in where vibrational and finally radiative transition occurs. This radiation is usually of the form of phosphorescence. The lifetime of this transition is very long (up to 10 seconds), upon CW excitation charge accumulation in the triplet state can occur, therefore preventive population inversion in the singlet state and therefore making very difficult lasing action.

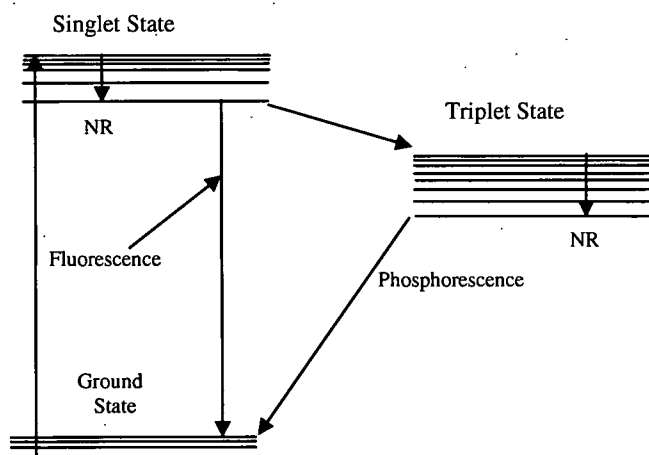


Figure 4.6 - Electronic Transitions involving both singlet and triplet states.

#### 4.2.7 Photoluminescence and Spectral Line-Narrowing of MEH-PPV in Films

The spectroscopic properties of MEH-PPV proved to be strongly dependent on not only of the preparation condition but also on the polymer chain's surroundings. Temperature, solvent and pressure are particularly important in the PL and ASE spectra. For instance, both the absorption and the photoluminescence redshift with the increment of pressure. These effects suggest that changes in pressure induce changes in the electronic polarizability of the polymer chains. Figure 4.7 shows the PL spectra of MEH-PPV in solution and in thin film obtained from the 5 g/dm<sup>3</sup> concentration. Notice that the PL emission in film is shifted by about 35 nm compared to the solution, which is consistent with the "gas-to-crystal" effect. This effect is a consequence of the stronger interaction of the MEH-PPV dipoles with its surroundings in the highly polarizable environment of a conjugated polymer film compared to the solution form [40].

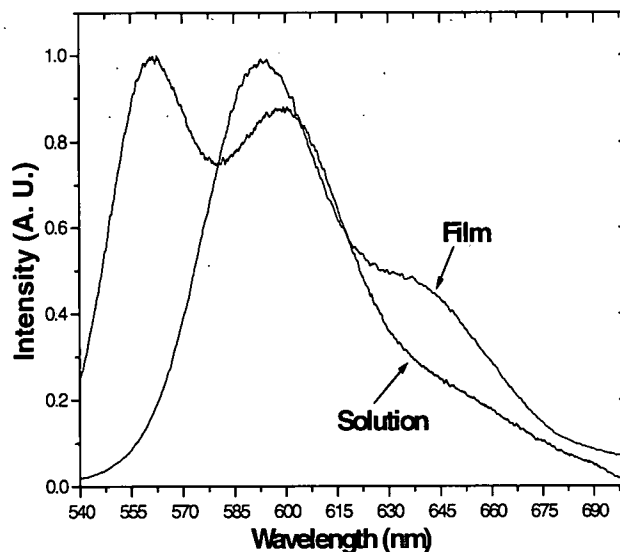


Figure 4.7 - Photoluminescence spectra of MEH-PPV in solution and film. The films were cast from the 5 g/dm<sup>3</sup> solution. The excitation source was a Nd:YAG pulsed laser operating at 532 nm.

The mechanism of spectral narrowing in MEH-PPV has been the subject of much debate [41]. Results which show line-narrowing can only happen when the index of refraction of the polymer is higher than the substrate and when the film is thick enough to support waveguiding suggest that spectral narrowing results from amplified spontaneous emission [42]. Sheridan et al [43] demonstrated the tunability of amplified spontaneous emission over a 40 nm range by controlling the waveguide thickness. This might suggest that the waveguide geometry is the primary factor that determines the SLN characteristics. Other mechanisms such as superfluorescence [44] biexcitons [45] and condensed excitons [46] have been proposed to explain the SLN.

In thin films, we argue that the polymer chains that are closer to the glass substrate behave differently than those that are further away. This is a consequence of the strong interaction of the polymer's dipoles on its surrounding. The spin coating process may have a different impact on the polymer chains closer to the glass interface compared to the chains further away from the interface. This may cause a variation of the electronic polarizability and the polymer morphology at different positions in the film. The influence of the polymer morphology on the emission spectra has been extensively studied in MEH-PPV [39]. The red shifted PL and SLN emission at lower temperatures [47] suggest that the polymer morphology is strongly dependent on the physical conditions of the polymer chains in films.

In order to study the SLN photophysics of the polymer of both the inner and outer layers of the polymer, the samples were characterized immediately after they were spun, so that the properties under study were mostly of the outer polymer chains. The outer polymers were then carefully removed by increasing the laser power, which caused the evaporation of the outer layers (about 45-60 nm). Similar spectra were obtained by removing the outer layers of material with a cotton swab dipped in toluene, but the laser ablation technique was preferred since the contact of the polymer with the toluene can contribute to the formation of aggregate species. Since both procedures provided the same results, the possibility that the laser ablation itself can induce changes in the polymer photophysics that could shift the emission wavelengths was ruled out. Figure 4.8 shows the PL of the film and the SLN spectra corresponding to both the inner and outer layers of the polymer film at different concentrations and solvents. In an earlier publication [48] we explained that the two emission bands corresponding to the inner and outer polymer chains in the films were due to the 0-0 and 0-1 band transitions respectively. This explanation relied on the correspondence of the spectral position between the two emission bands of the PL profile (the emission wavelengths are roughly 10 nm red shifted compared to the 0-0 and 0-1 PL transitions). However, notice that both spectra in figure 4.8 show an emission peak around 570 nm and 600 nm respectively ( in toluene at a concentration of 5 mg/ml), which are at shorter wavelengths compared to the SLN emission. These emission bands are most likely the result of the 0-0 band transition. As a consequence, the SLN in both cases is observed in the 0-1 band transition (just as in solution).

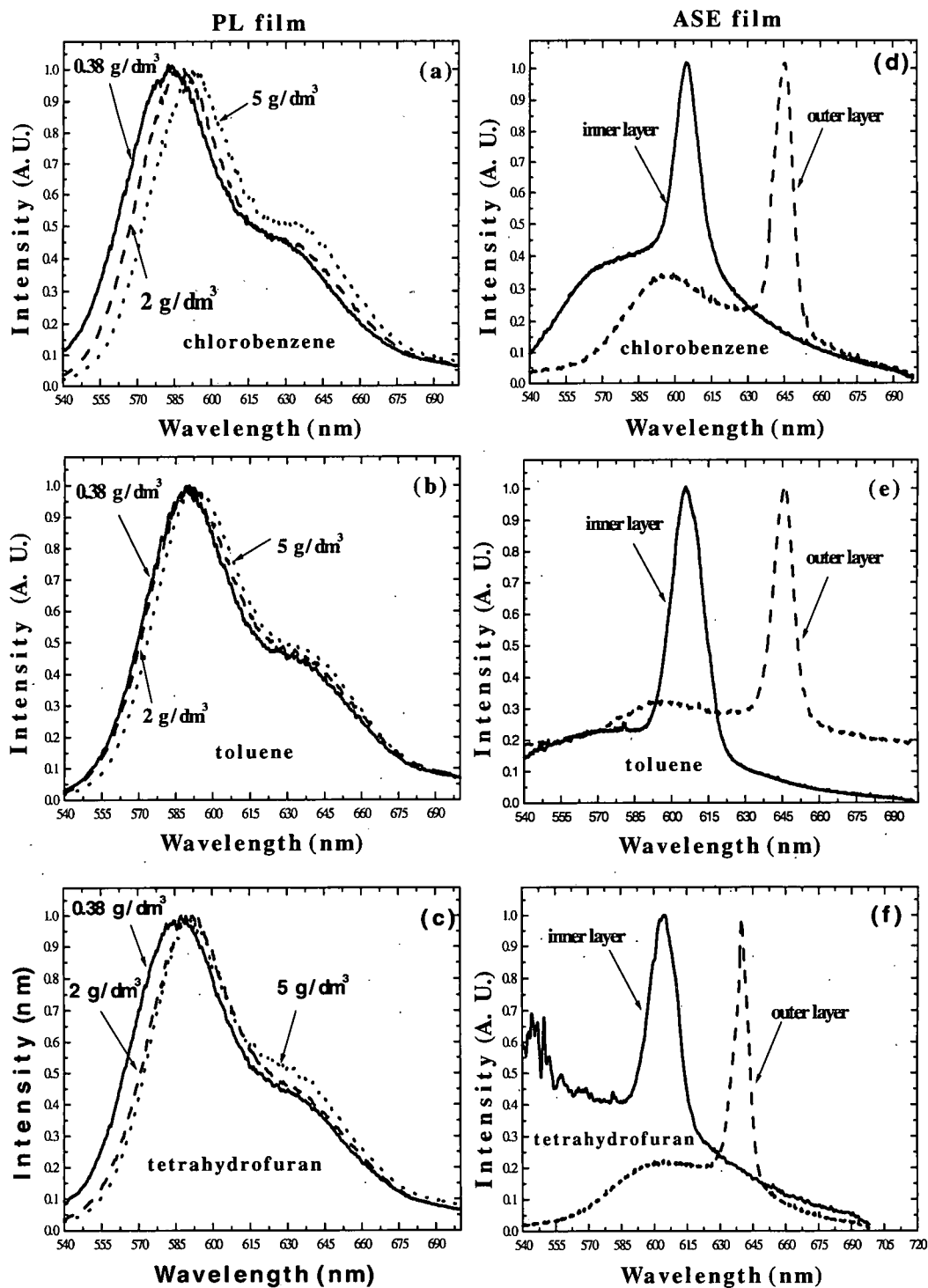


Figure 4.8 - Photoluminescence (a,b,c,) and spectral line-narrowing (d,e,f) spectra of MEH-PPV at different concentrations in films and in different solvents. The excitation source was a Nd:YAG pulsed laser operating at 532 nm.



The red shifted emission coming from the outer polymer (which was shifted around 40 nm compared to the emission of the inner chains) is attributable to the “gas-to-crystal” effect. In other words, the polarization environment of the outer layer of the polymer is quite different than the inner layer that is closer to the glass substrate. It is interesting to point out that when the samples are excited for the first time, one would expect that emissions from both the inner and outer polymer chains should be observed. Instead only the emission of the outer polymer was recorded. Since the emission from the inner polymer chains appears at shorter wavelengths compared to the outer polymer chains, the emission from the inner polymer chains is most likely absorbed by the outer polymer chains. Figure 4.9 illustrates that it is also possible to observe line-narrowing from both transitions at the same time by removing just enough material from the sample surface (30-35 nm).

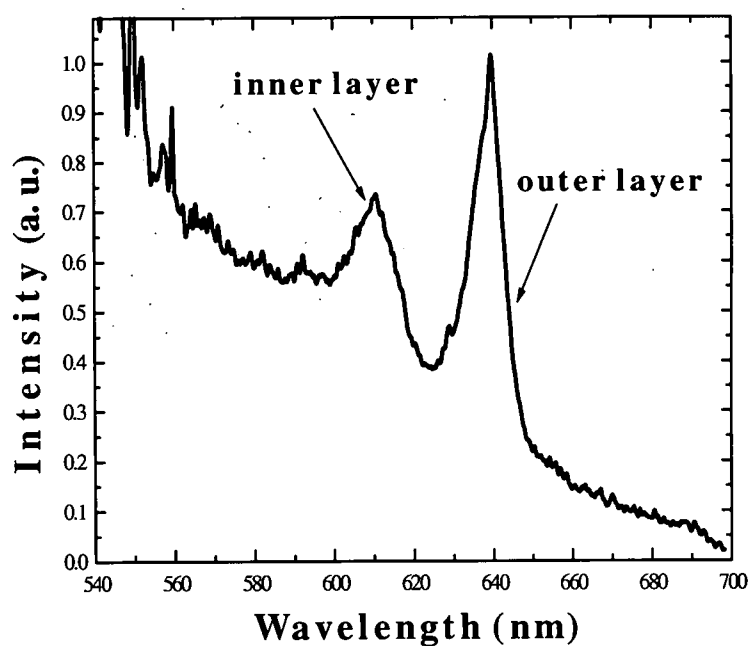


Fig. 4.9 - Spectra line-narrowing of MEH-PPV film cast from the toluene solution. Laser ablation removed just enough material from the surface of the samples so SLN from both inner and outer polymer chains takes place.

The mechanisms described in [43] are important for explaining the shape of the ASE spectra. However if waveguide confinement were the only mechanism for the SLN, that will imply a total emission bandwidth of around 60 nm (590 - 650 nm). To the best of our knowledge, such large ASE bandwidths in MEH-PPV have not been reported. The emission from solution shows, where there is no waveguide confinement, a bandwidth of only 20 nm (at a concentration of 5 g/dm<sup>3</sup>). Also notice that the peaks of the SLN bands are around 603 and 645 nm. Hence the waveguiding model might suggest that the line-narrowing emission is occurring at both the 0-0 and 0-1 vibronic transitions (see figure 2). The waveguiding model cannot explain the two ASE bands of figure 4.9. In other words the crystal to gas effect may be important in explaining the line-narrowing properties of MEH-PPV in films.

These results suggest that in thin films, two line-narrowing emission bands are observed as a consequence of the interaction of the polymer chains in different polarizable environments, probably as a consequence of the spin coating process. These results could have important implications for devices based on MEH-PPV, especially for lasing applications. Since the SLN radiation of the inner most polymer chains can be absorbed by the outer polymer chains, this can significantly reduce the effective gain in a laser structure.

#### 4.2.8 Grating Fabrication

To fabricate the 1-D grating structures, interferometric lithography was used to pattern the photonic crystal on a photoresist layer on the glass substrate. The photoresist (refractive index 1.52 at 632.8 nm) was diluted with Shipley Microposit EC-11 solvent at a ratio of 1:5, and spun on a silica substrate at 3000 rpm. The resulting film thickness was 70 nm as measured by a Tencor P10 surface profilometer. Figures 4.10 and 4.11 show the interferometric lithography system and the rotating stage respectively. The setup is similar to a Lloyd-mirror configuration. A CW argon laser operating at 244 nm (after second harmonic conversion) is used as the illumination source. The beam is expanded and then combined at the sample. The direct beam and the secondary beam are reflected off the mirror to produce an interference pattern with period given by:

$$\Lambda = \frac{\lambda}{2 \sin \theta} \quad (85)$$

After the photoresist was developed, the samples were soft baked at 100 C for 1 hour and then exposed to UV radiation (mercury lamp, 365 nm) for about 1 hour to increase the hardness of the photoresist. Figure 4.12 shows the atomic force microscope (AFM) image of the 1-D photonic crystal structure. The period of the corrugation was about 400 nm with an average depth of 70 nm.

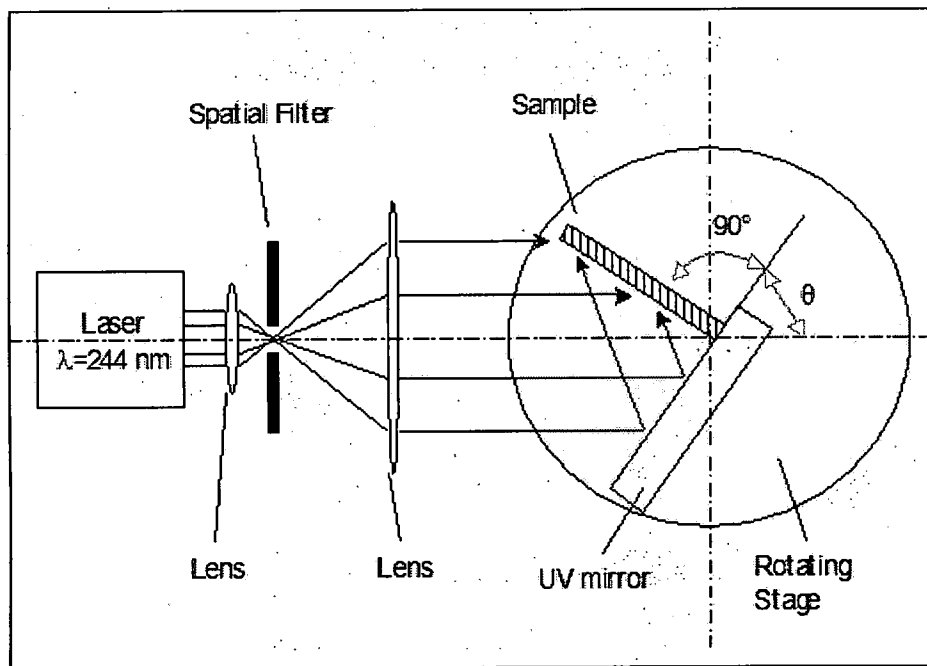


Figure 4.10 - Interferometric lithography setup. Grating periods from 150 nm to 2  $\mu$ m can be fabricated by selecting the appropriate angle  $\theta$ . An angle of 17.758 degrees was selected to obtain a grating period of 400 nm. The laser source is an argon laser operating at 244 nm with an intracavity second harmonic crystal.

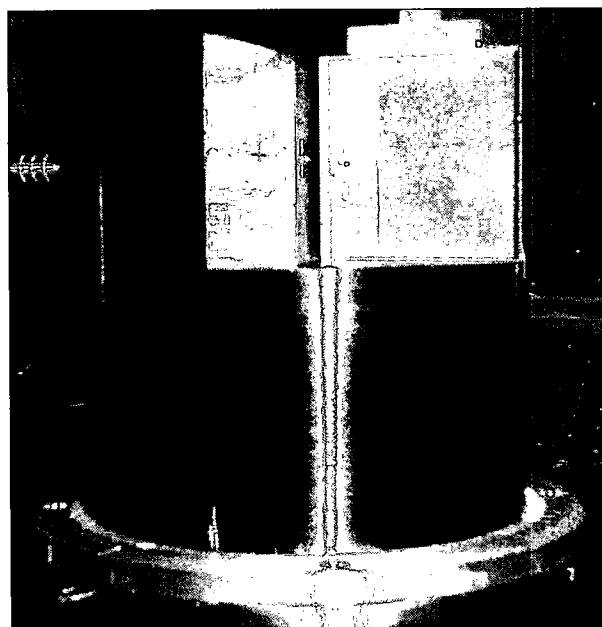


Figure 4.11 - Rotating stage cylinder showing the UV mirror, the vacuum suction for the sample holder and the angle scale.

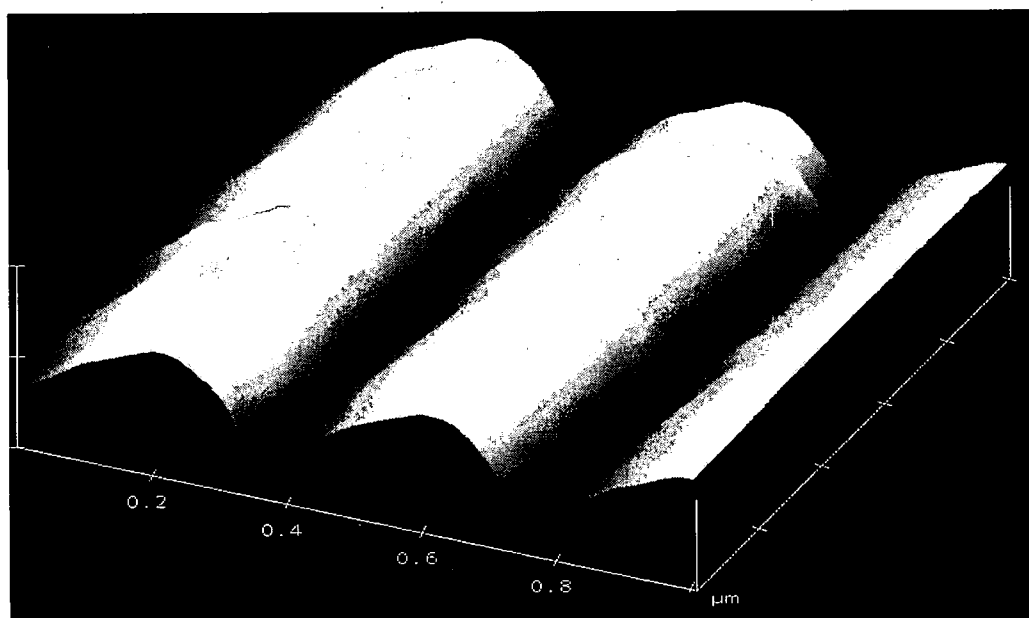
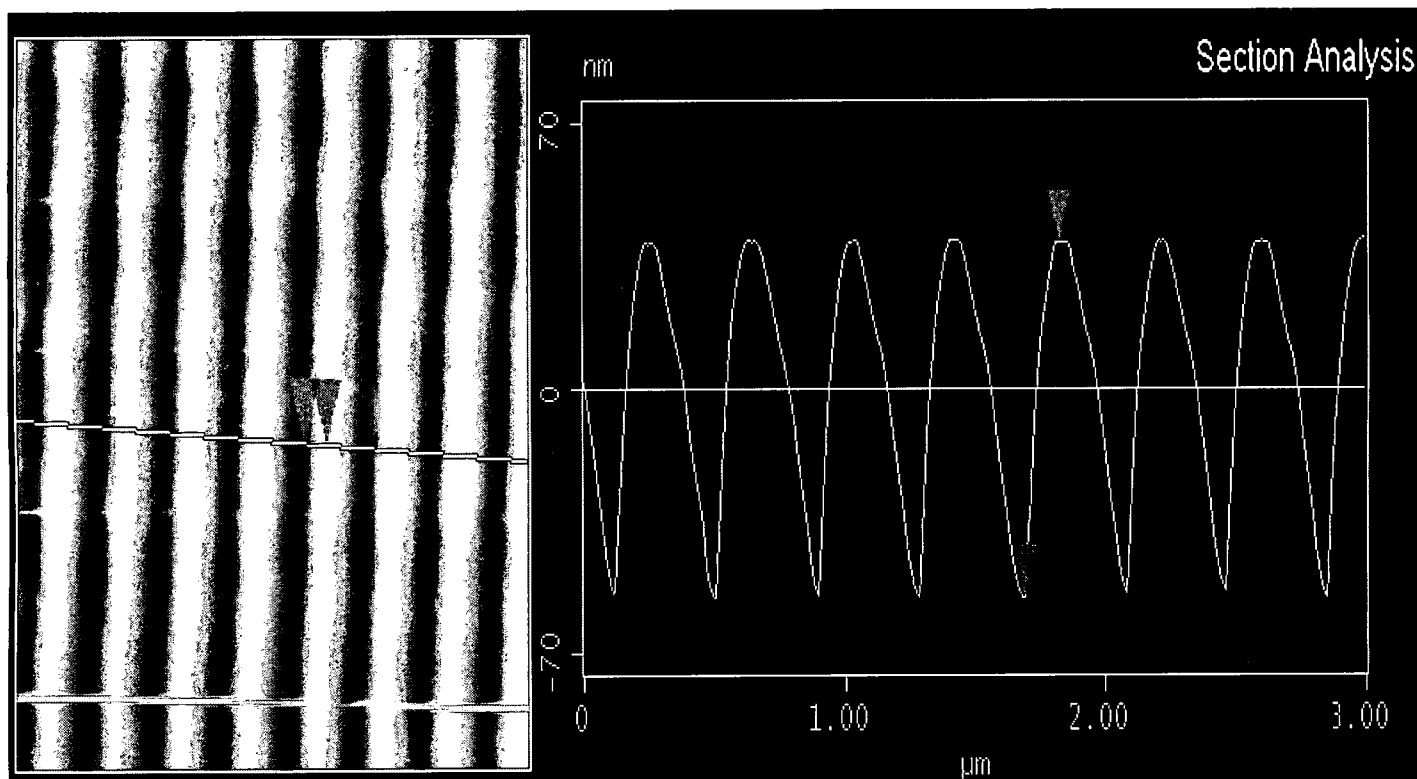


Figure 4.12 - shows the atomic force microscope (AFM) image of the 1-D photonic crystal structure. The period of the corrugation was about 400 nm with an average depth of 70 nm.

It is important to emphasize that if the gain media presents a narrow gain band, a precise control of the grating period must be achieved in order to operate within the gain region of the material. Even small angle variations of half degree in the rotating stage (figure 4.11) can shift considerably the resonant wavelength. To fabricate accurate grating periods, the experimental setup shown in figure 4.13 was used to measure the period of the photonic crystal obtained after the interferometric exposure. Interactions were performed until the desired period was obtained.

#### *4.2.9 Lasing Action*

The silica samples were not etched; instead photoresist-polymer interfaces were used as the final patterns. This was done for the purpose of increasing the effective index around the corrugation area. The overall effect is an increase in the confinement factor of the fundamental optical mode in the laser waveguide structure around the corrugation, which decreases the threshold gain of the device. To incorporate the gain media into the laser structures, the MEH-PPV (refractive index 1.8 at 640 nm) was deposited from solution onto the samples to form a film thickness of 100 nm. To prevent photooxidation and to enable operation of the device in an oxygen rich environment, a 1.5  $\mu\text{m}$  thick layer of polymethylglutarimide (PMGI) was spin coated on top of the MEH-PPV film. PMGI has a refractive index of 1.54 at 640 nm and is transparent to visible light [49].

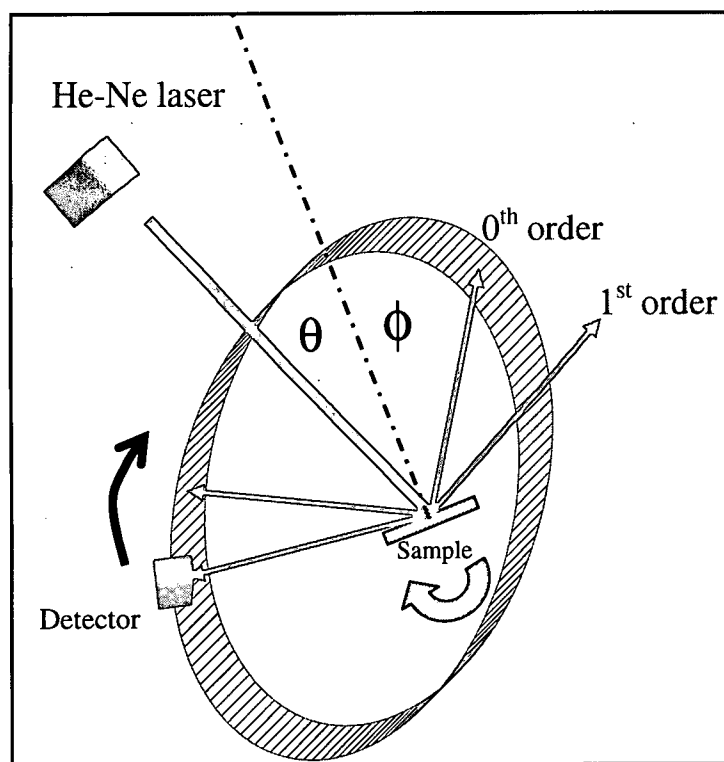


Figure 4.13 - Schematic showing the grating period measurement. The period is obtained by determining the inside and diffracted angle.

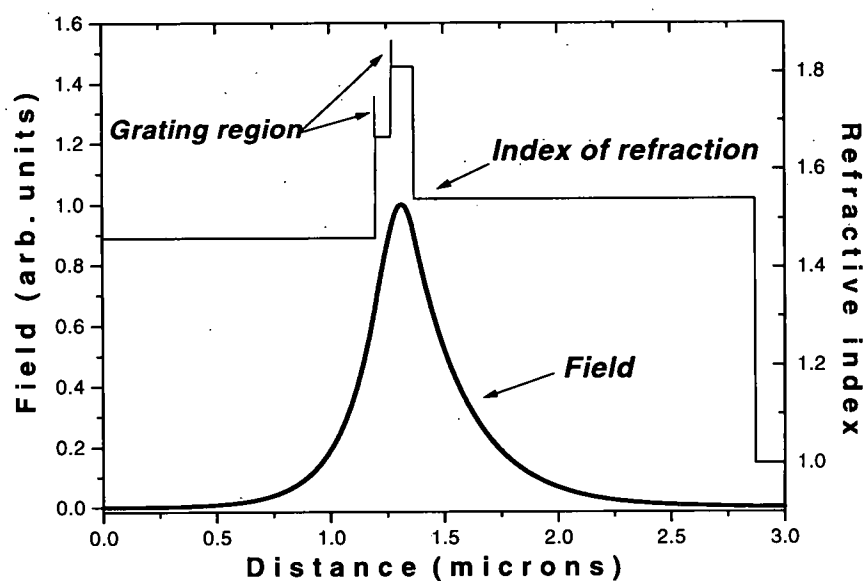


Figure 4.14 - Theoretical calculation of the fundamental mode of the polymer waveguide structure. The refractive index profile of the device shows excellent overlapping between the field distribution and the grating region, thus ensuring low threshold gain for the laser.

Figure 4.14 shows the theoretical calculation of the fundamental mode in the polymer film waveguide. In this calculation the refractive index of the corrugation region was approximated as the average of the refractive indices of PMMA and MEH-PPV. Notice that this approximation is reasonable, since this mode is quite similar to the one determined using coupled mode theory in the previous chapter (see figure 3.10). The effective index of the structure was found to be around 1.60. The Bragg condition that determines the lasing wavelength of the photonic crystal structure is given by:

$$\Lambda = n \frac{\lambda_B}{2n_{eff}},$$

(86)

where  $n$  is an integer,  $n_{eff}$  is the effective index of the structure,  $\lambda_B$  is the Bragg wavelength and  $\Lambda$  is the period of the photonic crystal. For surface emission normal to the corrugation, a second order diffraction grating with  $n = 2$  was chosen. The period  $\Lambda$  must be selected such that the Bragg wavelength overlaps with the amplified spontaneous emission (ASE) of MEH-PPV. In this particular case, a period  $\Lambda$  of 400 nm was selected. Figure 4 shows the ASE spectra obtained by pumping an unpatterned film of MEH-PPV coated with PMGI. It is important to note that a film patterned with a photonic crystal structure will produce a PL spectrum that has an angular dependence due to the diffraction process in the photonic crystal. Therefore care must be taken to avoid misinterpreting the PL spectrum.



Lasing action in the photonic crystal MEH-PPV was obtained by optically pumping the devices beyond the threshold gain of the laser. The resulting laser emission was normal to the surface at both faces of the polymer film. To test the directionality of the emission, the laser spectrum was recorded at 12 inches away from the sample. The recorded spectrum from the device is shown in figure 4.15. It shows considerable line-narrowing to  $\leq 0.65$  nm FWHM, the resolution limit of the spectrometer. Compared to most lasing materials, MEH-PPV has a very broad ASE spectrum. This allows the laser emission to be tuned over a large range by varying the periodicity of the photonic crystal structure or by tailoring the thickness of the MEH-PPV layer to change the effective index of the waveguide structure.

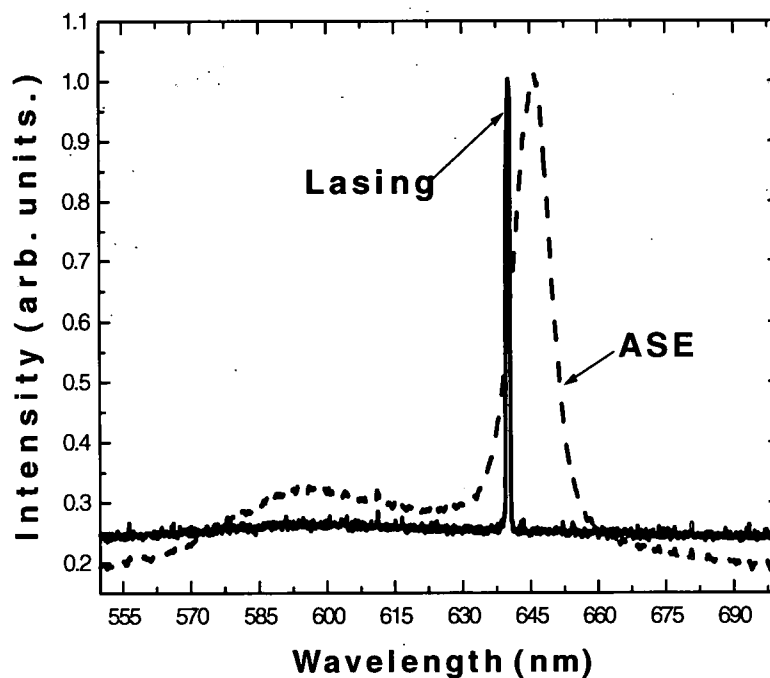


Figure 4.15 - Amplified spontaneous emission (ASE) spectrum (dashed) obtained by photopumping an unpatterned film of MEH-PPV coated with PMGI. The solid line represents lasing action from the photonic crystal laser. The spectrum was recorded at 12 inches from the device with a FWHM around 0.65 nm, which is limited by the resolution of the spectrometer.

## Chapter V

### 2-D Distributed Feedback Laser Theory and Experiments

#### *5.1 Introduction*

One of the major drawbacks of 1-D photonic crystal lasers is the existence of lateral modes that lead to multimode operation, which limits the operation of single mode high power lasers. One approach to obtain higher power is to use several narrow stripes of active regions arranged to work together in a phase locked array [50]. However to overcome the problems associated with the phase difference of the individual lasers, techniques such as binary filter [51] and other elaborated structures [52, 53] need to be incorporated into the design. A very elegant way to reduce the lateral modes and concentrate the laser emission in a narrow spectral line is to create optical confinement of the propagating waves in all directions (in-plane) through a 2-D photonic crystal structure [12].

Multimode lasing from a two-dimensional cross grating structure using an active dye as the gain medium was reported in the early 70's [54]. L. Lyk'yanova et al [55] observed a very low divergence (0.33 degrees X 0.33 degrees in the far field) beam from a single mode crossed grating device. V. Sychugov et al. [56], also reported extremely low divergence angle in the far field, and the angular divergence of the

radiation was determined as a function of the pumping rate above the threshold value. Toda et al. demonstrated that Bragg reflection only takes place for TM modes and not for TE modes in a crossed grating structure having the same period in both directions [12].

More recently, a nearly diffraction-limited surface emitting two-dimensional grating lasers have been investigated by S. Riechel et al. using conjugated ladder type poly (p-phenylene) (LPPPP) as the gain media [57]. This work demonstrated that a 2-D DFB structure can drastically reduce the divergence of the laser emission compared to a 1-D corrugation. In addition to the improvement in beam divergence, the 2-D structure also showed a higher efficiency and a lower threshold gain.

In this chapter we present experimental results for two-dimensional distributed feedback lasers based on MEH-PPV. We report laser instabilities associated with the pumping geometry for 2-D photonic crystal structures. These instabilities can result in the degradation of the spectral quality of the laser emission and in an increase in the threshold gain.

## *5.2 Laser action from a two-dimensional distributed feedback laser*

Whereas in 1-D structures a corrugation periodicity of 400 nm is used, two perpendicular corrugations of 400 nm form the 2-D photonic crystal structure. In this configuration laser action is achieved by phase locking the modes established in the two perpendicular resonators [57]. However this laser configuration has a drawback

of being dependent on the optical pumping geometry as will be shown next. To achieve a 2-D structure, two successive exposures are performed after rotating the sample by 90 degrees. See figure 4.10 . Thus the exposure time of each step has to be half the exposure time required for the 1-D structure. Figure 5.1 shows the atomic force microscope (AFM) image of the 2-D photonic crystal structure on a photoresist layer. After the 2-D structure is obtained, the same process as described in chapter 4 is used to complete the laser structure by spin coating the MEH-PPV and the PMGI.

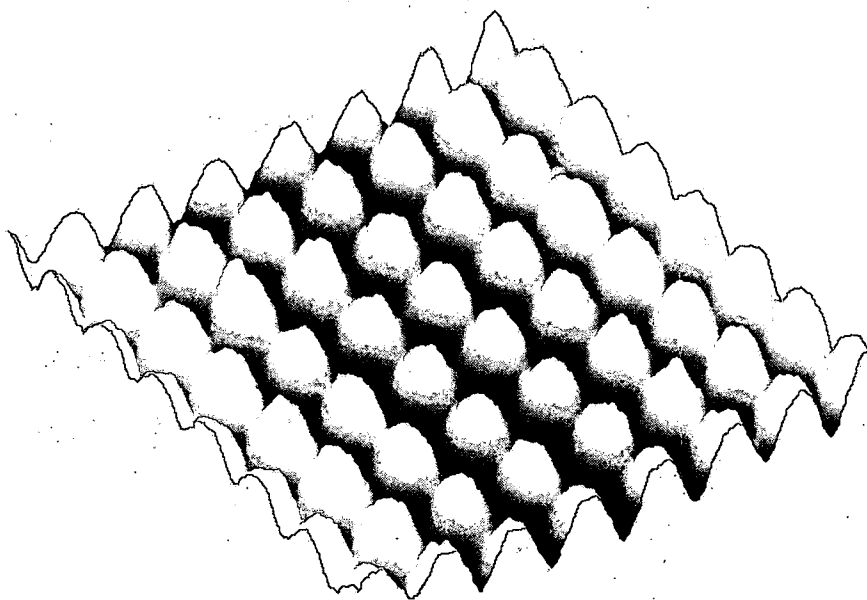


Figure 5.1 - Atomic force microscope (AFM) image of the 2-D photonic crystal structure. The period of the corrugation was about 400 nm in both directions with an average depth of 80 nm.

The observed laser emission was normal to the surface of the device. Figure 5.2 illustrates the difference in the spectral characteristics obtained by pumping the laser with a circular and elliptical spot. Figure 5.2 (a) shows the laser spectrum recorded by the spectrometer when the device is pumped with a collimated circular spot. However, when the structure is pumped with a non-circular beam, instabilities can take place as shown in figure 5.2(b). To understand the difference between the two

spectra in figure 5.2, an illustration of the diffraction process taking place in the grating is presented in figure 5.3. The circular excitation geometry allows both perpendicular resonators to have nearly equal threshold gains, and thus the locking process between the two resonators is more readily achieved. In contrast, when the device is pumped with a non-circular spot, one of the resonator sees a longer pumping length and thus its threshold gain is lowered. Hence the longer stripe is more likely to lase compared to the other resonator with the shorter pump stripe. This geometry makes the locking process between the two perpendicular resonators more difficult. The result is that the device behaves as a 1-D DFB laser along the longer stripe, and as a simple diffraction grating along the shorter stripe. This can be inferred from the diffraction slope around the lasing wavelength in Figure 5.2. The overall effect is an increase in loss due to the diffraction produced by the shorter resonator, that ultimately increases the threshold pumping power and deteriorates the spectral quality of the laser emission.

Figure 5.3 shows the diffraction process for these geometries. Another disadvantage of this configuration is that as discussed before Bragg reflection does not take place for TE modes in identical grating period, so only TM polarization can be obtained. A more proactive solution could be a fourth-order process in which both grating work in synergy to couple the backward and forward traveling waves. Figure 5.3(b) shows this diffraction process in k-space. This configuration is inherently more stable since both gratings are needed to complete the coupling process. It is also less susceptible to an arbitrary excitation geometry, and cross gratings can be designed with different periods for TE modes.

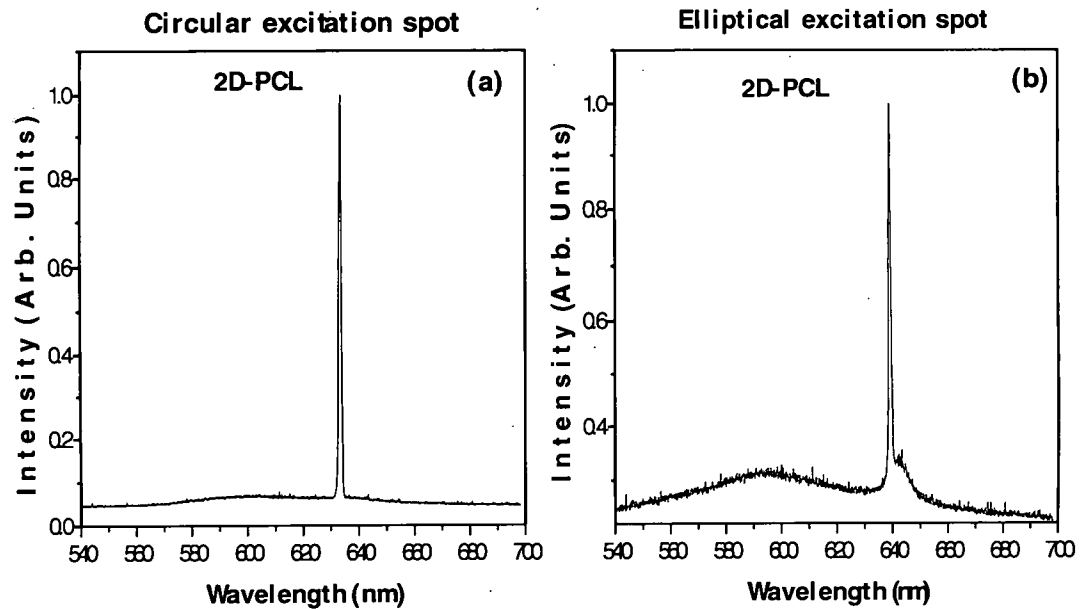


Figure 5.2 - a) Laser action from a 2-D PCL as pumped with circular spot. This pumping configuration presents better spectral characteristics compare with the elliptical geometry. Figure 5.2(b). Laser spectrum from a 2-D PCL as pumped with an elliptical spot. Notice the diffraction slope around the lasing wavelength.

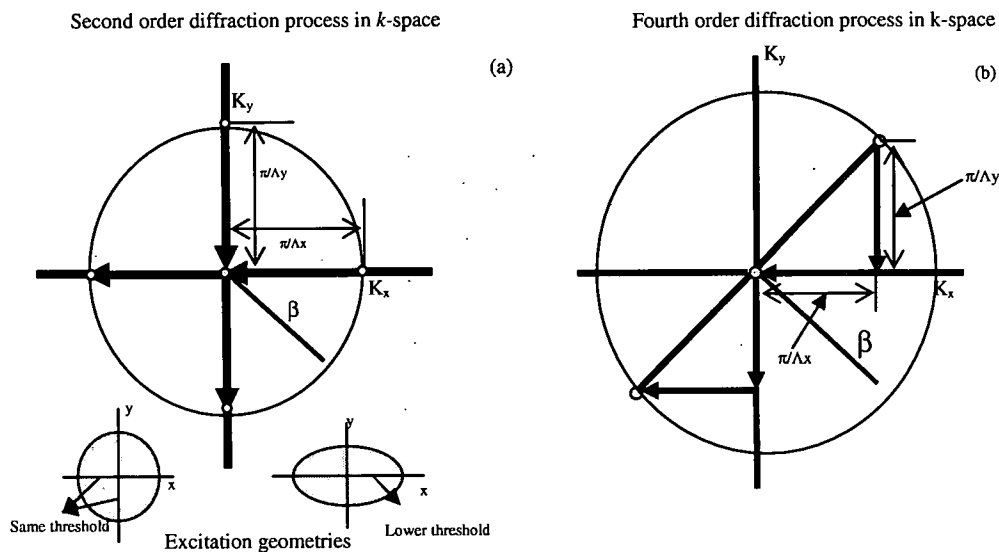


Figure 5.3 - Second order diffraction mechanism in 2-D PCL. In this configuration the grating vector couples the forward and backward waves in two steps. Surface emission is achieved through crossing the origin of the k-space coordinates after the first diffraction step. The device behaves as a two independent resonators and thus performance is dependent on pumping geometry. Figure 5.3(b). Fourth order process in 2-D PCL. This configuration is more stable since both gratings must work simultaneously to couple the forward and backward waves, thus only one resonator is defined.

## **Chapter VI**

### **CONCLUSIONS**

In this dissertation a comprehensive study of one and two dimensional distributed feedback lasers (1D-DFB and 2D-DFB) has been presented. Numerical and experimental results were presented for the case of 1D-DFB. For the experimental studies the polymer 2-methoxy-5-(2'-ethylhexyloxy)-1, 4-phenylenevinylene (MEH-PPV) was employed as gain media. This thesis also presented experimental results for optically pumped 2D-DFB lasers with different pumping geometries.

Chapter 2 provides a detailed analysis of 1D-DFB laser based on the coupled mode theory. The theory presented in this chapter uses Floquet's theorem to perform an accurate analysis of DFB lasers by considering the effect of the radiation modes in the threshold gain and detuning characteristics. The second order surface emission lasing and the effects of phase and discrete reflections at the facets were also included in the model.

To perform a detailed theoretical calculation of the model presented in chapter 2, the same laser structure that was used for the experimental investigations was studied to determine the threshold gain characteristic of the laser. Detailed

calculations using Floquet's formalism and including the influence of radiation modes in the laser performance was used to accurately describe surface emission DFB. Triangular shape was used to approximate the patterned grating structure, however the analysis can be applied to any grating shape.

Chapter 4 presented an experimental study of the lasing action from a 1D surface emission DFB using MEH-PPV as the gain medium. The study of the photophysics and spectroscopic characteristic of MEH-PPV were presented and the properties as suitable gain material for lasing applications were examined. This chapter also showed that the emission characteristics of the polymer in solutions are quite different from the samples in films. The ASE in solutions and films were shifted around 35 nm, therefore this phenomenon was taken into account for the resonant wavelength design in the DFB structure. Interferometric lithography was used to pattern the gratings structure on SiO<sub>2</sub> substrates and the lasing characteristics of 1-D DFB lasers were studied.

In chapter 5 we reported for the first time the instabilities associated with the lasing characteristics of 2-D DFB lasers with circular and elliptical pumping geometries. This phenomenon was the result of the laser design using equal periods that satisfied Bragg's conditions in both perpendicular directions. A more stable configuration was also proposed and it is the subject of our studies for future works.



## Recommendations

Future effort will be directed towards developing a complete theory of two-dimensional distributed feedback laser using the same formalism that was introduced in chapter 3. The theory will study the effect of radiation modes in the threshold characteristics of two-dimensional distributed feedback laser and will also study the effect of grating structure design on performance to try to correct and or prevent problems like the one presented in figure 5.2. The experimental demonstration of lasing action was done based on polymer based gain media, since it is a cheap and versatile way to study the DFB characteristics. As future work we will transfer our experience using the conjugated polymer to develop 2-D DFB laser based on semiconductor gain materials using quantum well and quantum cascade structure.

## Appendix A

### Matlab code

```
% One and Two Dimensional Surface Emission Distributed Feedback Lasers Based
on
% MEH-PPV. Dissertation Submitted to School of Engineering UNIVERSITY OF
% DAYTON In Partial Fulfillment of the Requirements for The Degree of Doctor of
%Philosophy in Electro-Optics By Aziz Mahfoud Familia.
% This program generate and calculate the decaying and radiating modes that are
describe by equations 25 and 26
% The program determines also the zetas coefficients describe in equations 29-32
% The structure analyze by this code is presented in figure 3.2.
% The first step is to calculate the fundamental mode of equation 16, which was
calculated using
% Dr. Andrew Sarangan photonics simulation program lights.
% The X and Field solution for equations 16 are contained in the file stre1
% This section calculate the E(m,0)
load variables
E0(1)=0;
E0(2000)=0
```

```

area=0

d=0

% grating period of 400 nm

period=0.4;

% Lasing wavelenght around 640 nm

lambda=0.64;

ko=2*pi/lambda;

dx=abs(XE0(2)-XE0(1));

% normalization of the fundamental field

for a=1:length(XE0)-1

    b=(E0(a).^2+E0(a+1).^2)/2;

    area=area+b*dx;

end

E0=E0/area.^0.5

% matrix definitions

Em=zeros(length(E0),length(E0));

radiation=zeros(2000,20);

for c=1:length(E0)

    Ef(c)=0;

end

% Radiation and decaying mode determination, the number of modes were limited to

20

for b=-10:10

```

```

d=d+1

q=b

% Propagation constant of the mode
Bm=(2*pi/period+2*pi*q/period);

Bo=2*pi/period

k=((ko^2*1.54^2-Bm^2)^0.5)

% aq coefficient determination at different positions of the grating structure
for a=2:length(XE0)-1;

if XE0(a)>= 0 & XE0(a) <= 0.93;

    no=1.46;

    aq=0;

end

if XE0(a)> 0.93 & XE0(a)<= 1;

    no = (-10.04 +13.28*XE0(a))^0.5;

    aq=(0.148/q)*i*(exp((-44.87*XE0(a)+38.6)*i*q)-exp((-
44.87+44.87*XE0(a))*i*q));

end

if XE0(a)> 1 & XE0(a)< 1.1;

    no=1.8;

    aq=0;

end

if XE0(a)>=1.1 ;

    aq= 0;

```

```

    no=1.54;

end

% Data point determination based on finite difference for the point a, a-1, a+1

Em(a,a)=-2/(dx^2)+ko^2.*no^2-Bm^2;

Em(a,a-1)=(dx*dx)^(-1);

Em(a,a+1)=(dx*dx)^(-1);

Ef(a)=-ko^2*aq*E0(a);

end

% Boundary condition points determination

Em(length(E0),length(E0))=-2/(dx^2)+ko^2.*no^2-Bm^2+exp(j*k*dx)/(dx^2);

Em(length(E0),length(E0)-1)=(dx*dx)^(-1);

Ef(length(E0))=ko^2*aq*E0(length(E0));

no=1.46

k=((ko^2*no^2-Bm^2)^0.5)

Em(1,1)=-2/(dx^2)+ko^2.*no^2-Bm^2+exp(j*k*dx)/(dx^2);

Em(1,2)=(dx*dx)^(-1);

Ef(1)=-ko^2*aq*E0(1);

% Solving matrix system

z=-Em\Ef);

for l=1:length(z)

    radiation(l,d)=z(l);

end

end

```

```

plot(XE0,abs(z))

save streemode radiation

% this section calculate the E (m,p) fields

% It is essentially the same program but with different aq values

% matrix definitions

Em=zeros(length(E0),length(E0));

radiation=zeros(2001,20)

for c=1:length(E0)

    Ef(c)=0;

end

for b=-10:10

    d=d+1

    q=b+2

    Bm=(2*pi/period+2*pi*b/period);

    Bo=2*pi/period

    k=((ko^2*3.4.^2-Bm^2)^0.5)

    for a=2:length(E0)-1;

        if XE0(a)<=0

            no=3.4;

            aq=0;

        end

        if XE0(a)> 0 & XE0(a)<=0.8;

            no=3.6;

```

```

    aq=0;

end

if XE0(a)> 0.8 & XE0(a)< 1

    aq = (-.7000000000*i*(exp(-8.421052632*i*pi*q*(1.187500000*XE0(a)-
.9500000000))-1)/(pi*q));

    no = (18.56-7*XE0(a)).^5;

end

if XE0(a)>=1

    aq= 0;

    no=3.4;

end

Em(a,a)=-2/(dx^2)+ko^2.*no^2-Bm^2;

Em(a,a-1)=(dx*dx)^(-1);

Em(a,a+1)=(dx*dx)^(-1);

Ef(a)=-ko^2*aq*E0(a);

end

Em(1,1)=-2/(dx^2)+ko^2.*no^2-Bm^2+exp(-j*k*dx)/(dx^2);

Em(1,2)=(dx*dx)^(-1);

Em(length(E0),length(E0))=-2/(dx^2)+ko^2.*no^2-Bm^2+exp(-j*k*dx)/(dx^2);

Em(length(E0),length(E0)-1)=(dx*dx)^(-1);

Ef(1)=-ko^2*aq*E0(1);

Ef(length(E0))=-ko^2*aq*E0(length(E0));

z=Em\'(Ef);

```

```

for l=1:length(z)

    radiationi(l,d)=z(l);

end

% determination of the zeta parameters

warning off

q=-2

t=aq.*E0.^2

kp=ko^2/(2*Bo)*trapz(XE0(1121:1201),t(1121:1201));

% zeta1 determination

zeta1=0

c=0;

for f=-10:-1

    c=c+1;

    if f~= -2

        q=-2-f ;

        aq= -.7000000000*i*(exp(-8.421052632*i*pi*q*(1.187500000*XE0-
.9500000000))-1)/(pi*q);

        t=aq.*E0.*conj(radiation(:,c));

        zeta1=zeta1+ko^2/(2*Bo)*trapz(XE0(1121:1201),t(1121:1201));

    end

end

c=11;

for f=1:10

```



```

c=c+1;

q=-2-f ;

aq= -.7000000000*i*(exp(-8.421052632*i*pi*q*(1.187500000*XE0-
.9500000000))-1)/(pi*q);

t=(aq.*E0.*conj(radiation(:,c)));

teta1=teta1+ko^2/(2*Bo)*trapz(XE0(1121:1201),t(1121:1201));

end

% zeta 2

zeta2=0

c=0;

for f=-10:-1

    c=c+1;

    if f~-2

        q=-f ;

        aq = -1.4000000000.*sin(pi.*q/2)/(pi*q);

        t=aq.*E0.*conj(radiationi(:,c)).*dx;

        zeta2=zeta2 + ko^2/(2*Bo)*sum(t(1121:1201));

    else

        end

    end

c=11;

for f=1:10

```

```

c=c+1;

q=-f ;

aq = -1.4000000000.*sin(pi.*q/2)/(pi*q);

t=aq.*E0.*conj(radiationi(:,c)).*dx;

zeta2=zeta2+ko^2/(2*Bo)*sum(t(1121:1201));

end

% zeta 3

zeta3=0

c=0;

for f=-10:-1

    if f~-2

        q=f

        aq = -1.4000000000.*sin(pi.*q/2)/(pi*q);

        t=aq.*E0.*conj(radiationi(:,(-f-2)+11));

        zeta3=zeta3+ko^2/(2*Bo)*trapz(XE0(1121:1201),t(1121:1201));

    end

end

for f=1:8

    q=f;

    aq = -1.4000000000.*sin(pi.*q/2)/(pi*q)

    t=aq.*E0.*conj(radiationi(:,(-f-2)+11));

    zeta3=zeta3+ko^2/(2*Bo)*trapz(XE0(1121:1201),t(1121:1201));

end

```

```

% zeta 4

zeta4=0

c=0;

for f=-10:-1

    if f~= -2

        q=f

        aq = -1.40000000000.*sin(pi.*q/2)/(pi*q);

        t=aq.*E0.*conj(radiation(:,(-f-2)+11));

        zeta4=zeta4+ko^2/(2*Bo)*trapz(XE0(1121:1201),t(1121:1201));

    end

end

for f=1:8

    q=f;

    aq = -1.40000000000.*sin(pi.*q/2)/(pi*q);

    t=aq.*E0.*conj(radiation(:,(-f-2)+11));

    zeta4=zeta4+ko^2/(2*Bo)*trapz(XE0(1121:1201),t(1121:1201));

end

```

## Appendix B

### Maple code for the solution of the threshold gain transcendental equation

```
# One and Two Dimensional Surface Emission Distributed Feedback Lasers Based on  
# MEH-PPV. Dissertation Submitted to School of Engineering UNIVERSITY OF  
# DAYTON In Partial Fulfillment of the Requirements for The Degree of Doctor of  
# Philosophy in Electro-Optics By Aziz Mahfoud Familia.  
# This code solve the equation 80.
```

```
restart;kappa:=1.193e-002-3e-004*I;L:=300;r1:=0;r2:=0;zita4:=-1.1399e-  
004+6.9957e-
```

```
004*I;zita2:=-1.3091e-004+7.0685e-004*I;zita1:= -1.2776e-004 + 7.0851e-004*I;
```

```
kappa := .01193 - .0003 I
```

```
L := 300
```

```
r1 := 0
```

```
r2 := 0
```

```
zita4 := -.00011399 + .00069957 I
```

```
zita2 := -.00013091 + .00070685 I
```

```
zita1 := -.00012776 + .00070851 I
```

```
> assume(kappa, real);
```

```
> assume(x, real);
```

```
> assume(y, real);
```

```

> assume(r1,real);

> assume(r2,real);

> assume(l,real);

> z:=x+I*y;

> f:=z^2*((1+r1*r2)^2-
*r1*r2*(cosh(z))^2)+(kappa+zita4)*(conjugate(kappa)+zita2)*(1-r1^2)*(1-
r2^2)*(sinh(z*L))^2+2*I*kappa*1*(r1+r2)^2*(1-r1*r2)*z*sinh(z)*cosh(z);

      f := (x+I*y)^2+(.1390158584e-3+.1661151206e-
4*I)*sinh(300*x+300*I*y)^2

> a:=evalc(f);

a := x^2-y^2+.1390158584e-3*sinh(300*x)^2*cos(300*y)^2-.1390158584e-
3*cosh(300*x)^2*sin(300*y)^2-.3322302412e-
4*sinh(300*x)*cos(300*y)*cosh(300*x)*sin(300*y)+I*(2*x*y+.1661151206
e-
4*sinh(300*x)^2*cos(300*y)^2-.1661151206e-
4*cosh(300*x)^2*sin(300*y)^2+.2780317168e-
3*sinh(300*x)*cos(300*y)*cosh(300*x)*sin(300*y))

> u:=Re(a);

      u := Re(x^2-y^2+.1390158584e-3*sinh(300*x)^2*cos(300*y)^2-
.1390158584e-
3*cosh(300*x)^2*sin(300*y)^2-.3322302412e-
4*sinh(300*x)*cos(300*y)*cosh(300*x)*sin(300*y)+I*(2*x*y+.1661151206
e-
4*sinh(300*x)^2*cos(300*y)^2-.1661151206e-
4*cosh(300*x)^2*sin(300*y)^2+.2780317168e-
3*sinh(300*x)*cos(300*y)*cosh(300*x)*sin(300*y)))

```

```
> v:=Im(a);
```

```
v:=Im(x^2-y^2+.1390158584e-3*sinh(300*x)^2*cos(300*y)^2-  
.1390158584e-
```

```
3*cosh(300*x)^2*sin(300*y)^2-.3322302412e-
```

```
4*sinh(300*x)*cos(300*y)*cosh(300*x)*sin(300*y)+I*(2*x*y+.1661151206  
e-
```

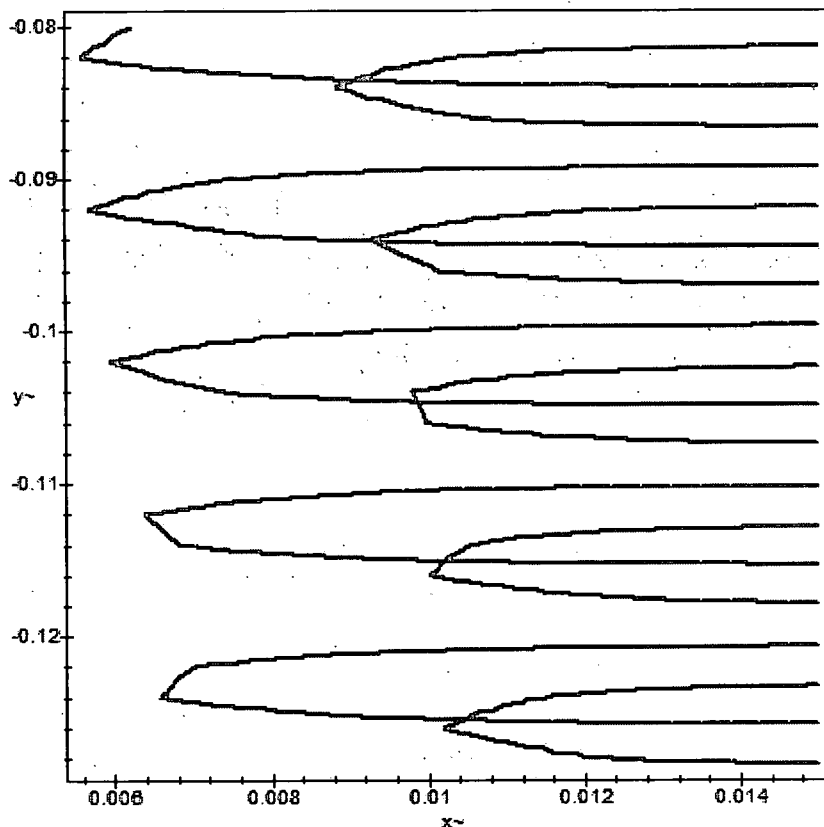
```
4*sinh(300*x)^2*cos(300*y)^2-.1661151206e-
```

```
4*cosh(300*x)^2*sin(300*y)^2+.2780317168e-
```

```
3*sinh(300*x)*cos(300*y)*cosh(300*x)*sin(300*y)))
```

```
> with (plots,implicitplot);
```

```
> implicitplot({u,v}, x=0.00..0.015,y=-0.13..-0.05);
```



# This graph is used to determined the corresponding to the values of x and y.

```
# each intersection represents a solution for x and y that later translate into solutions
for
```

```
# the gain and detuning coefficient.
```

```
>a:=[fsolve({u=0,v=0}, {x,y},{x=0..0.02,y=-0.13...-0.12})];
```

```
>assign(a);
```

```
    a := [{x = .1020277234e-1, y = -.1255920395}]
```

```
>a:=((alpha+I*delta)^2-(conjugate(kappa)+zita2)*(kappa+zita4))^.5-zita1;
```

```
za := ((alpha+I*delta)^2-.1390158584e-3-.1661151206e-4*I)^.5+.12776e-3-.70851e-
3*I
```

```
>ab:=evalc(za);
```

```
>b:=fsolve({Re(ab)=x,Im(ab)=y},{delta,alpha});
```

```
b := {alpha = .1005355123e-1, delta = -.1243239643}
```

```
>assign(b);
```

```
>alpha:=alpha*L;delta:=delta*L;
```

```
alpha := 3.016065369
```

```
delta := -37.29718929
```

## Bibliography

- [1] E. Yablonovitch, "Inhibited spontaneous emission in solid state physics and electronics", Phys. Rev. Lett. **58**, 20 2059-2062, (1987).
- [2] W. Streifer, D.C. Scifres, R. D. Burnham, "Coupling coefficient for distributed feedback single and double heterostructure diode laser", IEEE J. Quantum electronics, vol. **QE-11**, No. 11 867-873, (1975).
- [3] W. Streifer, D.C. Scifres, R. D. Burnham, "Analysis of grating-coupled radiation in GaAs:GaAlAs lasers and waveguide", IEEE J. Quantum electronics, vol. **QE-12**, No. 7 422-428, 1976.
- [4] W. Streifer, D.C. Scifres, R. D. Burnham, "Analysis of grating-coupled radiation in GaAs:GaAlAs lasers and waveguide II: blazing effects", IEEE J. Quantum electronics, vol. **QE-12**, No. 8, 494-498, 1976.
- [5] W. Streifer, D.C. Scifres, R. D. Burnham, "Coupled wave analysis of DFB and DBR lasers", IEEE J. Quantum electronics, vol. **QE-13**, No. 4, 134-141, 1977.
- [6] H. Kogelnik, C.V. Shank, "Coupled-wave theory of distributed feedback lasers" J. Appl. Phys., **43**, No. 5, 2237-2335, (1972).
- [7] K. Handa, s.t. Peng and T. Tamir. "Improved perturbation Analysis of dielectric grating", Appl. Phys. **5**, 323-328, (1975).
- [8] M. Nakamura, J. Umeda, A. Yariv, A. Kazir and H. Yem, "GaAs-GaAlAs distributed feedback diode laser with separated optical and carrier confinement", Appl. Phys. Lett., **27**, 145-146, (1975).
- [9] S. Wang and S. Sheen, "Two dimensional distributed feedback lasers and their applications", Appl. Phys. Lett., **22**, 460-463, (1973).
- [10] L. Vurgaftman and J. Meyer, "Photonic crystal distributed feedback lasers", Appl. Phys. Lett., **78**, No. 12, 1-4, (2001).
- [11] H. Han and J. Coleman, "Two dimensional rectangular lattice distributed feedback lasers: a coupled mode analysis of TE Guided modes", IEEE Journal of Quantum Electronics, **31**, no.11, 1947-1954, (1992).



- [12] M. Toda, "Proposed cross grating single-mode DFB laser", *IEEE Journal of Quantum Electronics*, **28**, no.7, 1653-1662, (1992).
- [13] K. Inoue, M. Sasada, J. Kawamata, K. Sakoda and J. Haus, "A two-dimensional photonic crystal laser", *J. Appl. Phys.* **74** 157-159, (1999).
- [14] A. Yariv, *Quantum electronics*, 3<sup>rd</sup> edition, New York, Wiley, (1989).
- [15] Ghafouri Shiraz, *Distributed feedback laser diodes*, Wiley, (1996).
- [16] W. Streifer, D.C. Sciprfes, "Radiation losses in distributed feedback lasers and longitudinal mode selection", *IEEE J. Quantum electronics*, vol. **QE-12**, 737-739, (1976).
- [17] W. Streifer, D.C. Scifres, R. D. Burnham, "Effects of external reflectors in the longitudinal modes of distributed feedback lasers", *IEEE J. Quantum electronics*, vol. **QE-11**, No. 4 154-161, (1975).
- [18] G. Sun, C. W. Trueman, "Approximate Crank-Nicholson schemes for the 2-D finite-difference time domain method for TE<sub>z</sub> waves", *IEEE Transactions on antennas and propagation*, **52**, No. 11, (2004).
- [19] G. R. Hadley, "Transparent boundary condition for beam propagation", *Optics Letters*, **16**, No. 9, (1991).
- [20] R. H. Friend, "Conjugated polymers. New materials for optoelectronics devices", *Pure Appl. Chem.*, **73**, No. 3, (2001).
- [21] T. Ito, H. Shirakawa, S. Ikeda, "Simultaneous polymerization and formation of polyacetylene film on the surface of concentrated soluble zeigler-type catalyst solution" *J. Polym. Sci. Chem. Ed.*, **12**, 11, (1974).
- [22] T. C. Chung, J. H. Kaufman, A. J. Heeger, "Fundamental Electrochemistry Studies of Polyacethylene", *J. Electrochem. Soc.* **131**, 2847, (1984).
- [23] J. H. Burroughes, D. D. C. Bradley, A. R. Brown, R. N. Marks, K. Mackay, R. H. Friend, P. L. Burn, A. B. Holmes, "Light-emitting diodes based on conjugated polymers" *Nature* **347**, 539-541 (1990).
- [24] B. Schweitzer, G. Wegmann, H. giesseb, d. Hertel, H. Bassler, R. F. Mahrt, U. Sherf, k. Mullen, "The optical gain mechanism in solid conjugated polymers", *Appl. Phys. Lett.*, **72** 2933, (1998).
- [25] R. Kersting, U. Lemmer, R. F. Mahrt, K. Leo, H. Kurz, H. Bassler, E. O. Gobel, "Fetosecond energy relaxation in pi-conjugated polymers", *Phys. Rev. Lett.*, **70**, 3820-3823, (1993).

- [26] R. Jakubiak, L. J. Rothberg, W. Wan, B. R. Hsieh, "Reduction of photoluminescence quantum yield by interchain interactions in conjugated polymers", *Synth. Met.*, **101**, 230-233, (1999).
- [27] S. Frolov, W. Gellerman, M. Ozaki, K. Yoshino, Z. V. Vardeny, "Cooperative Emission in  $\pi$ -Conjugated Polymer Thin Films" *Phys. Rev. Lett.*, **78**, 729, (1997).
- [28] Y. Shi, J. Liu and Y. Yang, "Device performance and polymer morphology in polymer light emitting diodes : morphology dependent emission spectra," *Macromol. Symp.* **154**, 187-197 (2000).
- [29] J. Gao, G. Yu, and A. J. Heeger, "Polymer p-i-n Junction Photovoltaic Cells," *Adv. Mater* **10**, 692-695 (1998).
- [30] J. Gao F. Hide, and H. Wang, "Efficient photodetectors and photovoltaic cells from composites of fullerenes and conjugated polymers: Photoinduced electron transfer," *Synth. Met.* **84**, 979-980 (1997).
- [31] T. Sakanoue, E. Fujiwara, R. Yamada, and H. Tada, "Visible light emission from polymer-based field-effect transistors," *Appl. Phys. Lett.* **84**, 3037-3039 (2004).
- [32] M. D. McGehee, A.J. Heeger, "Semiconducting (Conjugated) Polymers as Materials for Solid-State Lasers," *Adv. Mater*, **22**, 1655-1668 (2000).
- [33] N.M. Lawandy, R.M. Balachandran, A.S.L. Gomes and E. Sauvain, "Laser action in strongly scattering Media," *Nature*, **368** 436-438 (1994).
- [34] G. Turnbull, P. Andrews, W. Barnes, I. Samuel, "Relationship between photonic band structure and emission characteristics of a polymer distributed feedback laser," *Physical Review B*, **64** 125122-11 - 125122-6 (2001).
- [35] M. Yan, L. J. Rothberg, E. W. Kwock and T. M. Miller, "Interchain excitations in conjugated polymers", *Phys. Rev. Lett.* **75**, 1992-1995, (1995).
- [36] J. A. Osaheni, and S. A. Jenekhe, "Efficient blue luminescence of a conjugated polymer exciplex", *Macromol.* **27**, 739-742 (1994).
- [37] T. Pauck, R. Henning, M. Perner, U. Lemmer, U. Sieger, R. F. Mahrt, U. Scheref, K. Mullen, and H. Bassler, "Femtosecond dynamics of stimulated emission and photoinduced absorption in a PPP-type ladder polymer", *Chem. Phys. Lett.* **244**, 171-176 (1995).
- [38] T. Q. Nguyen, V. Doan, and B. J. Schwartz, "Conjugated polymer aggregates in solution: control of interchain interactions", *J. Chem. Phys.* **110** 4068-4078 (1999).

- [39] T. Nguyen, I. B. Martini, J. Liu, B. J. Schwartz, "Controlling interchain interactions in conjugated polymers: The effects of chain morphology on exciton-exciton annihilation and aggregation in MEH-PPV Films", *J. Phys. Chem. B*, **104**, 237-255 (2000).
- [40] B. C. Hess, G. S. Kanner, and Z. Vardeny, "Photoexcitation in polythiophene at high pressure" *Phys. Rev. B*, **47** 1407-1411 (1994).
- [41] M. D. McGehee, R. Gupta, S. Veenstra, E. K. Miller, M. A. Diaz-Garcia and A. J. Heeger, "Amplified spontaneous emission from photopumped films of a conjugated polymer", *Phys. Rev. B* **58** 7035-7039, (1998).
- [42] F. Hide, M. Diaz-Garcia, B. J. Schwartz, M. R. Anderson, Q. Pei, A. Heeger, "Semiconducting polymers: a new class of solid-state laser materials", *Science*, **273** 1833-1836 (1996).
- [43] A. K. Sheridan, G. A. Turnbull, A. N. Safonov and D. W. Samuel, "Tuneability of amplified spontaneous emission through control of the waveguide mode structure in conjugated polymer film" *Phy. Rev. B*, **62**, R11929-R11932, (2000).
- [44] S. Frolov, M. Osaki, W. Gellerman, K. Yoshino and Z. V. Vardeny, *Phys. Rev. Lett.* **78** 729, (1997).
- [45] G. Kranzelbinder, M. Nisoli, S. S tagira, S. De Silvestri, G. Lanzani, K. Mullen, U. Scherf, W. Grauper and G. Leising, "Cooperative effects in blue light emission of poly(para-phenylene)-type ladderpolymer, *Appl. Phys. Lett.* **71**, 2725-2727, (1997).
- [46] G. Gelinck, J. Warman, M. Remmers and D. Neher, "Narrow-band emissions from conjugated-polymer films" *Chem. Phys. Lett.* **265** 320-326, (1997).
- [47] A. K. Sheridan, J. M. Lupton, I. D. Samuel, D. D. C. Bradley, "Temperature dependence of the spectral line narrowing and photoluminescence of MEH-PPV", *Synth. Met* **111-112** 531-534, (2000).
- [48] A. Mahfoud, A. Sarangan, T.J. Nelson, and Elmo A. Blubaugh, "Role of aggregation in the amplified spontaneous emission of ([2-methoxy-5-(2'-ethylhexyloxy)-1,4-phenylenevinylene] ) ", *J. of Lumin.*, **118** 2, 123-130, (2005).
- [49] M. D. McGehee, A.J. Heeger, "Semiconducting (Conjugated) Polymers as Materials for Solid-State Lasers," *Adv. Mater*, **22**, 1655-1668 (2000).
- [50] D. R. Scifres, C. Lindstrom, R. D. Burnham, W. Streifer, and T. L. Paoli, "Phase-Locked (GaAs)Al laser diode emitting 2.6 w CW from a single mirror," *Electron Lett.* **19**, 169-171, (1983).

- [51] N. W. Carlson, J. K. Butler and V. J. Masin, "Coupled mode analysis of wavefront properties of phase locked array diode lasers," *Electron. Lett.* **22**, 1327-1328,(1986).
- [52] L. J. Mawst, D. Bitez, T. J. Roth and J. J. Yang, "Diffraction limited beam operation from quantum -well laser phase-locked array grown by metalorganic chemical vapor deposition," *Electron. Lett.*, **24**, 570-571, (1988).
- [53] W. Streifer, D. F. Welch, P. S. Cross, and D. R. Scifres, " Y-junction semiconductoir laser array ," *IEEE J. Quantum Electron.* **23**, 752-756, (1987).
- [54] S. Wang and S Sheem, "Two-dimensional distributed feedback lasers and their applications", *Appl. Phys. Lett.* Vol. **22**, pp. 460-462, (1973).
- [55] L. I. Luk'yanova, V. Shelkov and S. Yakunovich, "Thin film laser with a two dimensional diffraction grating ", *Sov. J. Quantum Electron.*, **9** 4, (1979).
- [56] V. A. Sychugov, A. V. Tischenko, and A. A. Khajimov, ,, Two-dimensional periodic structures in thin-film lasers," , *Sov. J. Quantum Electron.* **12**, 27, (1982).
- [57] S. Riechel, C. Kallinger, U. Lemmer, J. Feldman, "A nearly diffraction limited surface conjugated polimer laser utilizing a two-dimensional photonic band structure", *Appl. Phys. Lett.*, **77**, 2310-2312, (2000).

R702033200

